TARGETED PHOTOSENSITIZERS AND CONTROLLED SINGLET OXYGEN GENERATION FOR THERAPEUTIC APPLICATIONS

A THESIS SUBMITTED TO
THE GRADUATE SCHOOL OF ENGINEERING AND SCIENCE
OF BILKENT UNIVERSITY
IN PARTIAL FULLFILMENT OF THE REQUIREMENTS FOR
THE DEGREE OF
MASTER OF SCIENCE
IN
CHEMISTRY

By
Esma Uçar
December 2018

TARGETED PHOTOSENSITIZERS AND CONTROLLED SINGLET OXYGEN GENERATION FOR THERAPEUTIC APPLICATIONS

By Esma Uçar

December 2018

We certify that we have read this thesis and that in our opinion it is fully adequate, in scope and in quality, as a thesis for the degree of Master of Science.

Engin Umut Akkaya (Advisor)

Ferdi Karadaş

Dönüş Tuncel

Özdemir Doğan

Canan Ünaleroğlu

Approved for the Graduate School of Engineering and Science:

Ezhan Karaşan

Director of the Graduate School

ABSTRACT

TARGETED PHOTOSENSITIZERS AND CONTROLLED SINGLET OXYGEN GENERATION FOR THERAPEUTIC APPLICATIONS

Esma Uçar

M.Sc. in Chemistry

Advisor: Engin Umut Akkaya

December 2018

Photodynamic therapy of cancer plays a pivotal role due to its many superior features and potential. Considering the pathways for improving the practice of PDT of cancer is gradually increasing, enhancing the selectivity of photodynamic action is an obvious choice. Being the source of reactive oxygen species in the body, mitochondrion is one of the most proper organelles to target. There is plethora of findings suggesting that triphenlyphosphonium cation is a very favorable mitochondria targeting agent. Another aspect of PDT requires creation of smart molecules which respond to either the increased temperature or ion concentrations in order to release $^1O_2$. Cyclic endoperoxides of naphthalene and anthracene could help in achieving the desired objective of storing $^1O_2$ and regenerating it again when appropriate conditions meet. The half-life cycloreversion of 1,4-Dimethylnaphthalene could be changed at least 100-fold when 2-position of the naphthalene is sterically hindered. Taking advantage of the fact that fluoride ions' silicophile nature, a novel perspective for drug design can be proposed. In the final project, a certain level magnetic hyperthermia, large enough to cause endoperoxide cycloreversion, but not large enough to cause necrotic death, is being sought after. Controlled generation singlet oxygen by the application of tissue penetrating alternating magnetic fields is the ultimate goal for that project.

Keywords: PDT, mitochondria, magnetic fluid hyperthermia, endoperoxide

ÖZET

TERAPÖTİK UYGULAMALAR İÇİN HEDEFLENMİŞ FOTODUYARLAŞTIRICILAR VE KONTROLLÜ SINGLET OKSİJEN ÜRETİMİ

Esma Uçar

Kimya, Yüksek Lisans

Tez Danışmanı: Engin Umut Akkaya

Aralık 2018

Kanserin fotodinamik terapisi birçok üstün özelliği ve potansiyeli barındırmasından ötürü, çok önemli bir role sahiptir. Kanserin fotodinamik terapi uygulamalarının geliştirilmesinin gitgide artması göz önüne alındığında, fotodinamik çalışmanın seçiciliğinin yükseltilmesi aşikar bir seçenektir. Mitokondri, vücutta reaktif oksijen türlerinin kaynağı olarak, hedeflemek için en uygun organellerden biridir. Trifenil fosfonyum katyonunun çok uygun bir mitokondri hedef ajanı olduğunu savunan çok fazla sayıda bulgular mevcuttur. Fotodinamik terapinin diğer bir yönü, $^1O_2$ salınımı yapabilmek için yükselen sıcaklık veya iyon konsantrasyonunu algılayabilen zeki moleküller oluşturmayı gerektirir. Naftalin ve antrasen gibi halkalı endoperoksitler, $^1O_2$ depolayarak ve uygun koşullar sağlandığında yeniden üreterek, bu istenilen amaca ulaşmamıza olanak sağlar. 1,4-Dimetilnaftalin'in 2 pozisyonu sterik olarak engellenmiş olduğunda, sikloreversiyonun yarı ömrü en az 100 kat artırılabilir. Florür iyonlarının silikofil doğasından yararlanarak, özgün ilaç tasarım perspektifi önerilebilir. Sonuncu projede, endoperoksit sikloreversiyonuna neden olacak fakat nekrotik hücre ölümü gerçekleştiremeyecek kademede manyetik hipertermi hedeflenmiştir. Kontrollü singlet oksijen üretimi için dokuya nüfus eden alternatif manyetik akım uygulaması, bu proje için nihai amaçtır.

Anahtar Sözcükler: PDT, mitokondri, manyetik akışkan hipertermisi, endoperoksit

Dedicated to my mother…

Acknowledgment

At first, I would like to offer my humble and eternal appreciation to Prof. Dr. Engin Umut Akkaya. There are too many things to say about his never-ending support, close attention, guidance, and limitless patience. He changed my life perspective as a scientist and a human by showing how can I become a much more developed individual. It is not possible to me not to remember his one of a kind effort along my life.

I also owe a special thank to Dr. Özlem Seven who thought me lots of things in the laboratory. Beside she is a good mentor who has unflagging support and patience, her friendship is also priceless to me.

I would like to acknowledge my special friend Dr. Nisa Yeşilgül due to her support and encouragement in and out of the laboratory, as well as her valuable friendship.

I would like to thank our past and present group members Dr. Safacan Kölemen, Darika Okeev, Yahya Ismael, Cansu Kaya, Seylan Ayan, Simay Aydonat, Dr. İlke Şimşek Turan, and the rest of the group members for creating a kind work-place atmosphere and establishing worthwhile friendships.

I owe exclusive thanks to our collaborators Assist. Prof. Dr. Ferdi Karadaş and Assist. Prof. Dr. Safacan Kölemen for their guidance and endless support.

I would like to thank all members of UNAM; especially to Selim Bozdoğan and İbrahim Tanrıöver for their infinite support and lively companion.

Last but not least I want to serve my gratitude to my family, especially my mother. I owe her to everything including every breath I take.

List of Abbreviations

PDT: Photodynamic Theraphy

PS: Photosensitizer

BODIPY: Boradiazadacene

LED: Light Emitting Diode

ROS: Reactive Oxygen Species

PEG: Poly (ethylene glycol)

TEG: Triethylene Glycol

t-BOC: Di-tert-butyl-dicarbonate

SPION: Superparamagnetic Iron Oxide Nanoparticles

MNP: Magnetic Nanoparticles

DPBF: 1,3-Diphenylisobenzofuran

TEM: Transmission Electron Microscopy

HRMS-TOF: High Resolution Mass Spectroscopy- Time of Flight

TBAF: Tetra-n-butylammonium Fluoride

ISC: Intersystem Crossing

Contents

List of Figures

Chapter 1

Introduction

1.1. Supramolecular Chemistry and Basic Interactions

Coming from the definiton of "chemistry beyond the molecule", the area of supramolecular chemistry have been developing day by day from the late 1960's.[1,2] It represents non-covalent interactions between two or more covalently bounded species. Those non-covalent interactions involve electostatic interactions, hydrogen bonding, van der Waals interactions, π-π interactions and some hydrophobic effects.[3] Supramolecular chemistry has an interdisciplinary fashion from inorganic chemistry to organic chemistry, physical chemistry to computational chemistry. Besides, lots of biological systems have non-covalent interactions, establishing relevance to supramolecular chemistry. Supramolecular chemistry has been improved many various areas such as molecular machines, molecular sensors, nanoreactors, chemical catalysis, drug delivery and so on.[4]

The first part of supramolecular chemistry comprises host-guest chemistry. The host molecule should include appropriote binding sites and geometries for small guest molecule. In order to achieve selectivity, some criteria such as complementarity of binding sites of host&guest molecules, preorganisation of the host structure and co-operativity of binding sites should have met.[5, 6] Host-guest chemistry utilizes the biological activity by extension of recognition-directed interactions through the reversible binding ability.[7]

The second part is composed by the self assembly of molecules by coming together via non-covalent interactions and form stable and well-defined structure aggregates. Assembly is the result of spontaneous association of compunds when the equilibrium conditions are supplied.[8, 9] Several kinds of shaped and sized supramolecular assemblies could be synthesized via using template reactions or hydrogen bonding.[10] The size scale could be in the range of micro to macro molecular in consideration of supramolecular assemblies formed from molecular assemblies.

Among the interactions which held those molecules togerther, electrostatic interactions have very strong characteristics and play a decisive role in the faith of supramolecular molecules and biological systems.[11,12] Just as in the tetrabutylammonium fluoride, the non-covalent interaction involves Coulombic interactions between oppositely charged particles.[5]

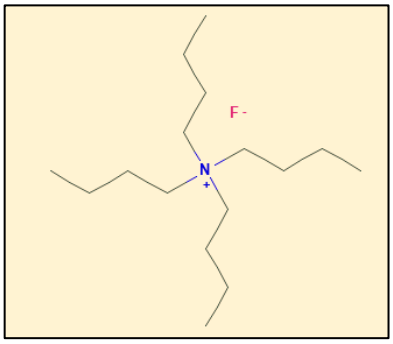

Figure 1. Coulombic interactions in tetrabutylammonium fluoride.

Because of its strength and directionality, hydrogen bonding conceivably has been used mostly in the supramolecular systems.[13] The hydrogen bonding is

frequently defined as non-covalent interaction between a suitable donor of acidic hydrogen atom and acceptor carrying available non-bonding electron pairs.[14] Whether it is essential, the double helix structure of DNA is a real-life example of hydrogen bonding.

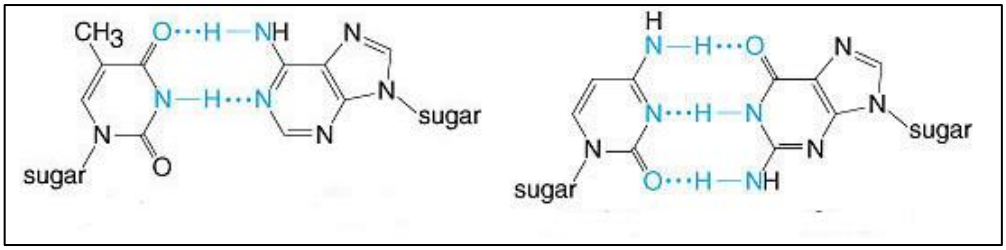

Figure 2. Hydrogen bonding in DNA.

The attraction forces coming from fluctuation between electron clouds of molecules in close proximity has been called as van der Waals interactions or London intreactions.[15, 16] As frequent as those interactions could be realized for another molecules by virtue of being the most basic interaction, supramolecular molecules are also experiences this type of interactions.

The π-π and cation-π interactions could be prevailed in both organic and organometallic chemistry.[17] The fact that cation-π interactions are based on electronic interactions, it is much far stronger than π-π stacking. Even, it has been argued that cation-π interaction strength are superior to hydrogen bonding.[18] Ferrocene is known for its cation-π interaction between iron and cyclopentadienyl group, while graphene has π-π interaction between its layers.

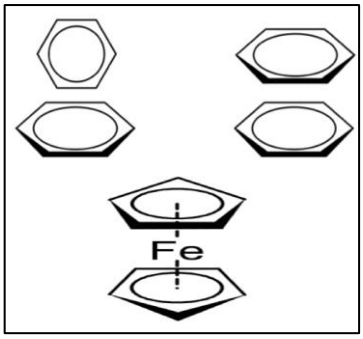

Figure 3. Edge to face π-π, cation-π, and face to face π-π interactions (from left to right).

Hydrophobic effect could be the reason of both enthalpic or entropic foundation.[19] The exclusion of non-polar groups in an aqueous solution could be given as a good instance. Thereby this exclusion paves the way for self-association of the non-polar sub-units to form aggregates. The effect arises from the some milestone knowledge of chemical interaction "Like dissolves like" outlining basically the polar species dissolves in polar solvents or vice versa. Hydrophobic effect is used for reserach in many areas including protein folding which is still a puzzle for biochemistry and biology.[20]

1.2. Luminescence and Photodynamic Action

The light which reserves the electomagnetic radiation of a wavelength is very significant when the words come to the living organisms, accordingly the science of chemistry and biology. In terms of electromagnetic spectrum, luminescence[21] is the concept that corresponds to the emission of ultraviolet, visible or infrared photons from electronically excited compounds. There are many types of luminescence containing electroluminescence, chemiluminescance, photoluminescence, thermoluminescence and so on.

If excitation occurs via light irradiation, it is called photoluminescence.[22] When a compound exposed to light, some of the light is absorbed by the compound which leads to the excitation of electron to higher energy level by experiencing different routes[23] (demonstrated in the Jablonski diagram) depending on the vibrational, translational or rotational properties of the chemical environment. The excited molecule subsequently relaxes back to the ground state by losing its excess energy. This relaxation may result as the emission of light; fluorescence which is a radiative transition and occurs between the states of same multiplicity and in the order of 10-50 nanoseconds.[24] If a singlet compound in the excited state goes to the triplet state which is called intersystem crossing and then relaxes back as a slower emission known as phosphorescence. The transition between states is given in the following Perrin-Jablonski Diagram involving the mechanism for photodynamic action.

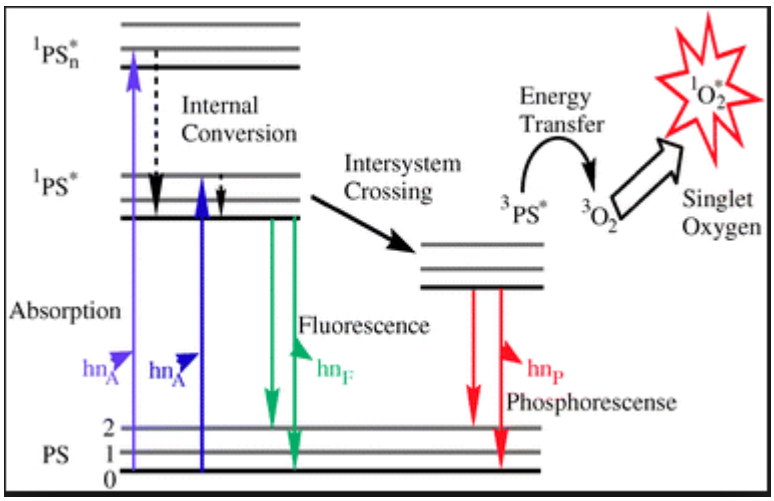

Figure 4. The Perrin-Jablonski Diagram displaying photodynamic action.[25]

Photodynamic action has its own mechanism which needs to actualize for photodynamic therapy. The mechanism involves PS and light so as to fulfill generation of reactive oxygen species, most importantly singlet oxygen. In Jablonski diagram, it is possible to assess that the ground state PS induced with photon will jump to the first excited state initially. After then, except radiationless relaxation, there are two possible routes to follow; either relaxation by emitting fluorescence or lapse to triplet excited state by intersystem crossing. When ISC is more favorable, singlet oxygen generation could occur since the triplet state energy can be assigned to ground state O_2. That kind of relaxation is also known as phosphorescence or delayed fluorescence.[26]

The fluorescence quantum yield is described as the ratio of number of emitted photons per the number of absorbed photons. In order to rephrase the previous

sentence, indication of ratio of excited molecules that relaxes back to the S_0 ground state from S_1 excited states yields the fluorescence quantum yield.[27]

1.3. Photodynamic Therapy

Photodynamic therapy is a non-invasive method which is used for diagnostic and treatment of number of diseases including certain cancer types such as malignant tumors of skin, brain, neck, gastrointestinal among others.[28] PDT is based on the activation of a photosensitizer with light at a specific wavelength to produce singlet oxygen (O_2^1) which destroys the nearby cells. In this therapy, a photosensitizer is introduced to a patient locally, orally or intravenously.[29] The hydrophobicity and the charge of PS designate its localization in the cell. PS has cationic charges are mainly accumulate in mitochondria while hydrophobic ones localizes the membrane of the cell. After 1-3 days of introduction, it is activated via light emitting diodes which has red or near infrared color (since fluorescent dyes which have longer wavelength excitation and emission are preferred for this therapy) in order to penetrate tissues better.[30,31] This activation of PS leads to the formation of reactive oxygen species including singlet oxygen (O_2^1) from molecular oxygen which will attack the close biological structure by giving oxidative damage.[32] Attacking by reactive oxygen species could result in initiation of apoptosis, activation of immune system or shut down vascular supply.[33]

History of the PDT dates back to ancient times, where phototherapy method was used in ancient Greece, Egypt and India.[34] However; it was disappeared for a long time until the modern practice has been reinstated in the Western civilizations. From pioneers Dane, Niels Finsen, Oscar Raab to Hermon von Tappeiner, the modern way of PDT has been established.[35] The phenomenon of PDT was first reported by Raab, nonetheless the first photosensitizer, Eosin, was first used for the treatment of skin cancer and reported by Tappeiner and Jesionek.[35] First clinical application trial of PDT was conducted by Dougherty in 1978 at Roswell Park Cancer Institute.[36] The following development is the approval of hematoporphyrin derivative as a PS from U.S. Food and Drug Administration in 1980.[36] Thenceforward, lots of novel PS derivatives have been developed and clinically tried. Several successes in treatment have been obtained for different kinds of diseases, especially for cancer.

1.4. Photosensitizers

Photosensitizers are the main and light-sensitive components of the PDT along with light and oxygen. They could be either naturally occurring such as plant extracts (Lumnitzera racemose) or synthetic such as BODIPY or phorphyrin derivatives.[37] In order to have enviable rate of photodynamic action, PS should have some fundamental physical and chemical properties which is taken into consideration in the process of structure design.

Especially since the spin transition from the triplet ground state to excited singlet state of oxygen is forbidden by spin selection rules, it could be advanced by spin-

orbit coupling. When angular momentums of spin and orbit mix with the singlet and triplet states of oxygen, it enables to forbidden transition between states by giving triplet state a singlet character. The equation for coupling is proportional to the fourth power of the atomic number; this in turn makes the heavier atoms much more suitable to achieve spin-orbit penetration.[38, 39 ,40] Generally, halogen atoms like bromine or iodine is used for this purpose in the literature.[41] In addition, possession of transition metal complexes such as Ru or Pt and intramolecular spin converters such as fullerene in the medium or in attachment of PS can enhance ISC.[41, 42] The most expected feature of a PS should be its $^1O_2$ generation efficiency which is directly related to the ability of transitions between introduced forbidden states.

Secondly, PS should be chemically stable as well as the photostability. PS should be chemically pure and stable at room temperature in account of incapacitate degradation.[43] It also has photostability which means that it should not be open to photobleaching,[39] alteration in characteristic of PS which further makes fluorescence impossible.

Biological compatibility is another requirement accompanied by physical and chemical properties. Due to the fact that they will be used for living cell treatment eventually, it should have sufficient water-soluble characteristic in advance. Dark toxicity[43] could be defined as damaging the cell media without the light interplay. PS should not have dark-toxicity and should only get excited by the light to generate singlet oxygen and attack nearby cells.[44] Otherwise, the drug is not efficient and deviates from the obvious goal of PDT. Additionally, PS

should not have side effects which can cause immunological response before PDT application.

Tumor tissue selectivity is another essential property of a feasible PDT agent. The formation of tortuous and leaky tumor blood vessels has been described in the name of "enhanced permeability and retention (EPR) effect" in cancer research.[45] Some of the most effective PS accumulation on the region of tumor experiencing EPR effect has been reported by Pütz et al., in 2016.[46]

Necessity for deep-tissue penetration of light is significantly important and probably the most important drawback of PDT together with hypoxia. Literature examples indicate that red light penetration (around 4-5 mm) is better than blue light penetration (around 1 mm).[47] Therapeutic window of the body (around 600-800 nm wavelength)[48] comprises the near-IR wavelength of the light, from 600 to 1350, and PS should provide the property of absorbing the range of light accordingly. However, certain amino acids could absorb some light near UV or visible lights.[49] Furthermore, beyond 1200 nm, the penetration decreases in a considerable amount owing to the water absorbance.[50] When those interferences are kept in mind, the most useful gap spans 600-800 nm.

1.5. Mitochondria Targeting for PDT

Photodynamic therapy of cancer is at the focus of renewed attention.[51] While the methodology is highly promising, there are issues[52] which limit broader applicability. Enhancing selectivity of photodynamic action is an important goal

in improving the practice of PDT.[53] To that end, chemical[54] and biochemical differences[55] of tumor microenvironment are being scrutinized. Overexpression of certain receptor proteins on cancer cell membranes[56], reducing intracellular medium of the tumor cells, including higher concentration of glutathione[57] and relatively acidic status of extracellular medium of tumor tissues[58] are very widely targeted differences. In recent years, organelle targeting of various drugs[59], including photodynamic photosensitizers received considerable attention. Mitochondria have been identified as particularly attracting targets for improving photodynamic efficiency, due to the fact that apoptosis following photodynamic action starts with structural and chemical changes in mitochondria.[60] One important difference between a normal cell and a cancer cell which is not exploited for enhancing selectivity of photodynamic action is the large difference between the membrane potentials ($\Delta\psi_m$) of normal cell mitochondria, and cancer cell mitochondria.[61] There is ample previous literature which report that carcinoma derived cells (breast cancer, prostate cancer, melanomas, etc.) have higher $\Delta\psi_m$ than normal epithelial cells by at least 60 mV.[62] Typically value for normal cells is -160 mV, whereas, in cancer cells, it is near -210 mV. In fact, mitochondria membrane potential is a reflection of the functional status of mitochondria, and believed to be strongly correlated with tumorigenicity and malignancy of the cells, as evidenced by survival in low oxygen conditions and increased ability for anchorage-independent growth.[63]

Fluorescent dyes[64] are very effective in many systems as well as the tracking of mitochondria. Mitochondrion is a double membrane organelle and plays a significant role in cell death and survival signaling. Oxidative phosphorylation

process requires a continuous flow of electrons and respectively mitochondria is the major source of reactive oxygen species.[65] When ROS is overproduced, it is harmful for some macromolecules. However, if ROS is produced in a controlled manner, it plays a pivotal role in signaling during the processes which consist of redox reactions.[65]

1.6. BODIPY Dyes

The lucky discovery of zwitterionic fluorophore BODIPY came true in 1968 by Treibs and Kreuzer[66] accidentally and it has become popular and popular day by day until its fluorescent properties revealed in 1991 by Haughland and Kang.[67] BODIPY (also known as Boron-dipyyromethe or Boradiazaindacene) has some appealing features leading to become one of the most important PS in the PDT. Initially the dye has sharp absorption and emission characteristics compared to other fluorescent dyes in the therapeutic window as mentioned earlier. Thermostability of BODIPY dyes is accompanied by chemical stability by having low sensitivity for both solvent polarity and pH and photostability[68] by minimizing the effects of photobleaching. Versatility of applications of BODIPY dyes[66] leads up to dramatically increasing research area due to functionalization and modification of newly BODIPY derivatives. Possibility of multiple chemical modifications on BODIPY allows the attachment of selective tumor targeting and water soluble chemical groups to increase the efficiency of photodynamic action. To synthesize fluorescent dyes which will have longer wavelength

absorbing or emitting characteristics, modified BODIPY dyes can be used efficiently.[69] Long-wavelength (650-900 nm) has some advantages such as minimum photo damage, deep tissue penetration and minimum interference from the fluorescent species in living system.[70] BODIPY based fluorescent dyes have many applications from molecular switches[71], photodynamic therapy[72], solar cell sensitizers[73], light harvesters[74] and to many more systems.

Halogenated BODIPYs[75] are widely used due to its efficiency for synthesizing various BODIPY derivatives. Furthermore, BODIPY derivatives have heavy halogen atoms are preferred for PDT since heavy halogens increases the rate of intersystem crossing which sparks of an increase in triplet state favoring ROS generation.

Due to negative electrochemical potential across the membrane of mitochondria, delocalized lipophilic cations[76] are preferable. For the purpose of surpass the membrane; triphenylphosphonium moiety could be used in the modification of the BODIPY dye.

Knoevenagel reaction is a high yielding method to the substitution of the BODIPY core. While the piperidine is used as organocatalyst, the Knoevenagel condensation of aldehydes with active methylene compounds is a widely used method for carbon-carbon bond formation[77] in the organic chemistry and has some applications such as the synthesis of heterocyclic compounds for biological importance.[78] While 3- and 5- positions of the BODIPY dye is functionalized through the Knoevenagel reaction, it is possible to obtain

BODIPY derivatives which have longer wavelength absorbing and emitting characteristics.[79]

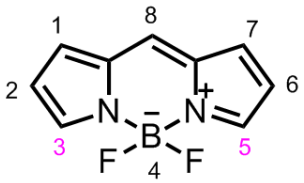

Figure 5. BODIPY core and its reactive sites.

1.7. Singlet Oxygen Properties

Aforementioned cytotoxic singlet oxygen has the capability of providing a sophisticated research opportunity. Due to being highly reactive, $^1O_2$ supplies predominant source of treatment for PDT.[80] Mainly, as it is produced, the attack for the biological structures in the vicinity takes place resulting oxidative stress[81] within the cells. It has been reported that the half-life of $^1O_2$ in aqueous solutions is around 3.45 μs and the distance traveled by $^1O_2$ in aqueous solutions is roughly 125 nm in literature.[82, 83] Due to being a short-lived species, the diffusion distance of $^1O_2$ is limited to a certain area, which enables us to target the tumor region without giving harm to healthy cells. While the importance of controlled $^1O_2$ generation is considered, utilization of the properties of $^1O_2$ is indispensable. Singlet oxygen generation could be achieved two distinct ways which both contributes to photodynamic action indeed. Type-I reaction[84] involves excited PS, hydroxyl radicals, superoxide anion or hydrogen peroxides. Those radical species could further react with biological molecules or molecular oxygen itself

to generate $^1O_2$. When produced $^1O_2$ is the primary reactant, the reaction is defined as Type-II[84]. After $^1O_2$ is generated and gets in contact with biological molecules, the expected outcome is apoptosis or necrosis as a biological response. Necrotic cell death is defined as a quick and violent degradation of cells by releasing all the cellular content as a result of destruction of plasma membrane.[85] Although necrotic cell death is unplanned; apoptotic cell death could be identified as "controlled cell death" by cleaving the cell units with "executioner caspases" such as caspase -3, -6, and -7.[86]

1.8. Cyclic Endoperoxides and Singlet Oxygen Storage

Ironically one of the most challenging conditions of singlet oxygen therapy is that cancer cells are already suffering from hypoxic[87] conditions. Therefore, whether the tumor cells are lack of oxygen; the molecular oxygen to generate singlet oxygen cannot be procured. Apart from fluorescent dyes which are capable of production of singlet oxygen, it was obvious that research world could come up with a solution which consist novel drugs as storage for singlet oxygen.[88] The most promising cyclic aromatic compounds (anthracene, naphthalene or pyridone) have been studied to trap and to regenerate singlet oxygen under exposition to heat.[89] The first study of endoperoxide was composed of the dissociation of rubrene[90] molecule in 1926, followed by some other endoperoxide investigation involving 9,10-Diphenylanthracene[91].

Singlet oxygen, due to its high reactivity, leads to the formation of endoperoxides[91], dioxetanes[92] and allylic hydroperoxides[93]. The synthesis of molecules could be described as photosensitized oxygenation which is the [4+2] addition[94] of oxygen molecule to desired cyclic aromatic compound. Due to electrophilic nature of $^1O_2$[95], it has much more tendency to react with compounds bearing more electron donating groups. The previous works also showed that singlet oxygen generation rate could rise up to at least 100-fold in polar solvents compared to non-polar solvents.[95] Steric factors are another dependency for inclination towards reaction for both $^1O_2$ and aromatic compound; while the steric stress relieved, it is much more convenient to synthesize the target molecule.[96] The scientists had been worked different series of fused ring aromatic compounds between 1-9, and reported that when the number of fused ring increases, the ease of chemistry come to light.[97] Formed endoperoxides are generally stable at room temperature; especially for some anthracene derived endoperoxides could reside without cycloreversion or any other degradation for months.

Initial reversible reaction between aromatic compound and $^1O_2$ forms a singlet state intermediate which further could lead the formation of endoperoxide[98, 99] or could go triplet state by ISC. Furthermore, triplet state intermediate can experience dissociation by yielding the starting material and $^3O_2$. The reaction mechanism consists of single step electron donation which is the major discrepancy from Diels-Alder cycloaddition. Suggested mechanism for [4+2] cycloaddition is demonstrated in the following Figure 6.

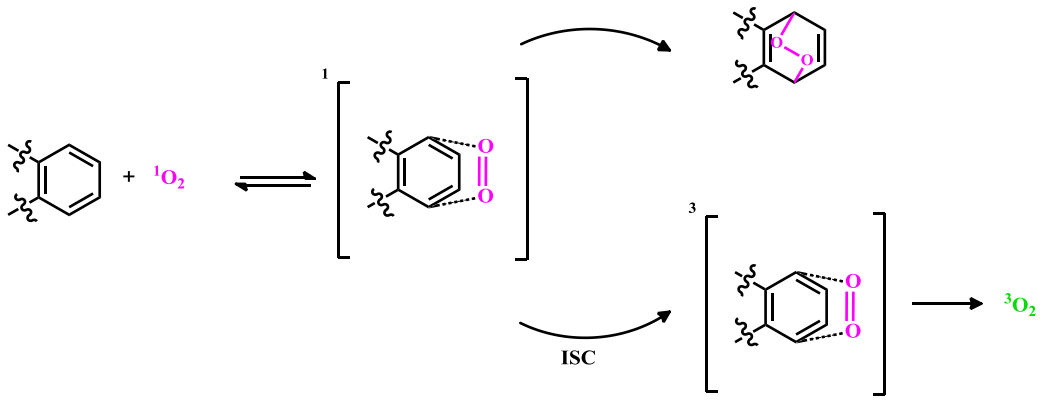

Figure 6. Suggested cycloaddition reaction mechanism for $^1O_2$ and aromatic hydrocarbons.

The dissociation mechanism of endoperoxide species can be explained by either thermolysis or photolysis[100]. Both of them have the similar outcome as homolytic cleavage of peroxide bridge by guiding quinones or hydroxyl-ketones, or as cycloreversion by guiding starting aromatic molecule, $^1O_2$, and $^3O_2$. The dissociation mechanism of cyclic-aromatic endoperoxides is shown in the Figure 7.

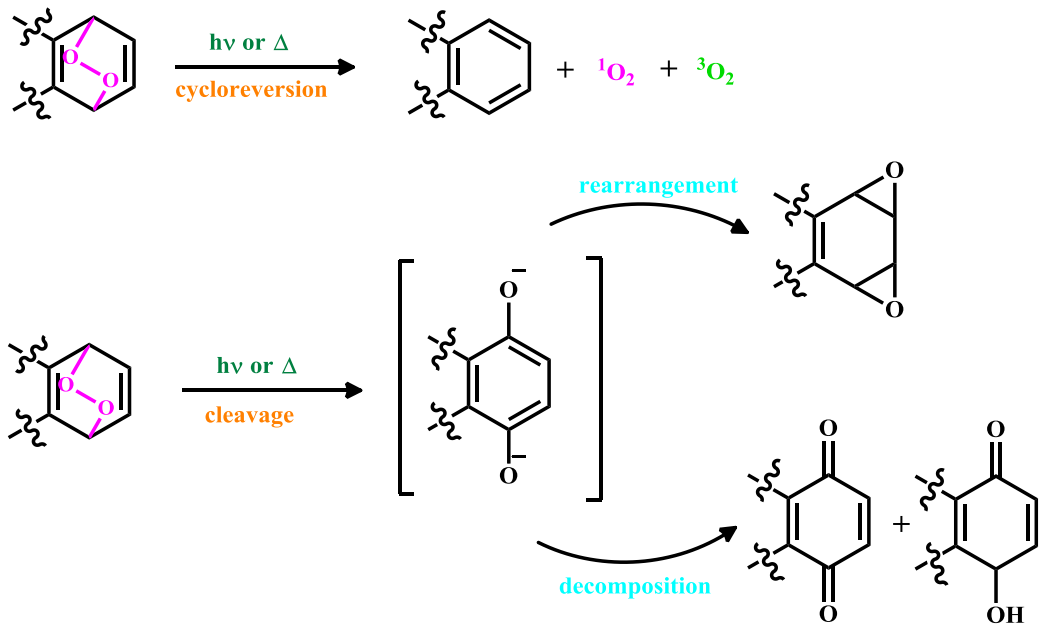

Figure 7. Dissociation pathways for thermolysis and photolysis of endoperoxides.

Cycloreversion could also follow two discrete pathways either resulting in homolytic cleavage or concerted cycloreversion. In concerted cycloreversion, only $^1O_2$ is produced along with the starting compound. Nonetheless, the homolytic cleavage could result in singlet and triplet oxygen emerging from ISC besides the starting material generation.

1.9. Sillyl Protection and Fluorine Mediated Deprotection

To prevent the reaction apart from the desired site of a multifunctional molecule, usage of protecting groups[101, 102] is ineluctable. Therefore, protection group utilization has been preserving its importance in organic synthesis for many years. With this importance, protecting group should have some expected properties as well. First of all, protective group should bear only one functional group which will further react and block the unwanted reactive site of the molecule on hand. Secondly, the deprotection should be easy and side-reaction free which could cause the formation of new reactive sites.

There are surfeit examples of protecting groups in the literature such as trimethylsilyl[103] (TMS) and di-tert-butyl-dicarbonate[104] (t-BOC) which are put to use in this very thesis, too. Deprotection of t-BOC group is usually carried out in the presence of acid such as TFA or HCl, nevertheless as I will introduce later in Chapter 3, it is achievable even with neat heating at 185 ^{0}C for 15-20 minutes.[102] Depending on the other substituents, however, t-BOC could be more expensive protecting group than TMS. Additionaly, most of organic molecules tend to degrade upon contact with acidic medium or high temperatures. Because of some serious drawbacks of various other protecting groups, TMS catches a valuable attention due to having a very easy deprotection routine. The high affinity of fluoride anions towards silicone has been notified various times since fluoride has very high nucleophilicity while silicon is overly electropositive.

Fluoride anion mediated deprotection of silly groups is accomplished via usage of tetrabutylammonium fluoride (TBAF) molecule or another fluorinated

compounds such as KF, as it is stated in Kishi and Kaburagi's work amongst others.[105, 106]

1.10. Half-life of Cycloreversion of Endoperoxide Derivatives

As it was indicated earlier, there is variance in fused ring endoperoxides including the modifications on the reactives sites. In the circumstances, the half-life of investigations of different endoperoxides is more than necessary to control the singlet oxygen generation as desired. Kinetic studies of endoperoxides have been performed various research groups up to now.[107, 108] However, the research area is relatively new and there are too many aspects to explore. Cycloreversion can be monitored thorough NMR, UV-Visible, or Fluorescence spectroscopy but there are some limitations like spectral overlap, ground state interactions between substrate and sensitizer, excited state interactions between substrate and photosensitizer and the probability of Type I reactions occurance.[109] In order to ensure the production of $^1O_2$, some singlet oxygen trap molecules such as 1,3-Dipenylisobenzofuran[110] or Aarhus Sensor Green[111] could be exploited.

1,4-Dimethylnaphthalene has been studied and recorded as a metastable endoperoxide at present.[112, 113] According to the study of Knör et al., the singlet oxygen generation could be delayed by tailoring the structural properties of 1,4-Dimethylnaphthalene in order to raise the energy barrier of thermal release of singlet oxygen.[114] The control operation under singlet oxygen release is really

important for biological structures in order to prepare the sickly region for cellular uptake of the drug.

1.11. Magnetic Fluid Hyperthermia

Hyperthermia therapy is the atrificial process of heating cancer cells in the temperatures between 41-45 ^{0}C which results in destruction of the tumor regions by inducing apoptosis or necrosis.[115] Hyperthermia treatment might be implemented for the whole body for metastatic cancer or some localized region for localized cancer such as certain organs or body cavities. Introduction of hyperthermia to body can be achieved by many different heating systems such as radiofrequency, microwave, ultrasound, or laser.[116] Radiation therapy and chemotherapy could be collaborate with hyperthermia to treat many kinds of cancer such as liver, sarcoma, brain, lung, breast, bladder, and esophagus.[117]

Magnetic fluid hyperthermia covers the irradiation with alternating magnetic field (AMF) so as to generate thermal energy around tumor tissue by Neel and/or Brownian relexation.[124] Alternating magneting field employment in order to induce magnetic fluid hyperthermia allows much more homogenous heating than other methods (like microwave heating) and is the pioneer work of Jordan et al. in 1993.[118] Hyperthermia therapy by using MNPs in oncology is highly promising due to being tumor-focused, less toxic and uniformly distributed.[119] The application is mainly based on the usage of magnetite, Fe_3O_4 nanoparticles, since they are highly biocompatible compared other magnetic nanoparticles which have toxic effects on biological structures. However, as a disadvantage of

iron oxide nanoparticles, one can conclude that having a high Curie point (phase transition point-1043 K) paves the way for overheating of healthy tissues along with tumor tissues.[120] Regulation of temperature range has tried to be achieved using manganese perovskites and lanthanum-strontium manganites.[121, 122]

1.12. Super Paramagnetic Iron Oxide Nanoparticles

Nanoparticle design in biological theranostic has been utilized for many different applications such as drug delivery, magnetic separation, hyperthermia and MRI constrast agents.[123] Applied magnetic field triggers a localized heating by occuring nanoparticle surface which is restricted to an area from a few angstroms to less than a nanometer.[124] Nanoparticles could be defined as nanosized aggregates which could be synthesized either aqueous or the organic media, of course stable at aqueous media nanoparticles are preferred for biological applications. Ability to flow over blood vessels and to enter tumor region efficiently make them appropriate tools to enhance therapeutic applications of various types of diseases. Nanoparticle size alteration could significantly change the ability of heat production, which is demonstrated in Puri et al. work, the most suitable diameter range lies in between 15-20 nm for magnetite particles.[125, 126, 127, 136] When the dispersity index of the particles gets lower, by other means when the particle size is in a narrow space, the interaction between biological molecules and nanoparticles rises up in a unique way.[128] Being aware of the magnetic properties, conducting properties or fluorescent properties of nanoparticles, researchers have been invented new methods to modify their

surface with some features such as water-solubility, drug attachment, and biocompatibility.[129, 130]

Among the other properties, the size of the nanoparticles remains the most important, since it has capability of determination of surface-to-volume ratio which could further affect magnetophoretic forces.[131] Thereby, the size influence over magnetic behavior investigations have a wider research area which is mostly conducted with dynamic light scattering (DLS) measurements of hydrodynamic sizes of the particles in solution.

Bare nanoparticles are unstable and could easily be oxidized from air. Additionaly, the particles intend to agglomerate due to their large surface areas to volume ratio and hence minimize the energy of surface.[132] Introduction of polymeric coating agents become very important when the idea comes to the biocombatility, there are vast numbers of literature examples showing that poly (acrylic acid) (PAA) has the capability of stabilization in neutral and slightly acidic media more than other coating materials.[132 ,133 ,134]

Chemical precipitation method[135] is accepted as the easiest method for iron oxide nanoparticle synthesis and thereby it is adapted for our work. When the pH is kept in between 8 to 14, the ratio of Fe^{2+} to Fe^{3+} (2:1) enables the synthesis of MNPs in aqueous solution by coprecipitation of ferrous salts. The materialized reaction is demonstrated in the following equation:

$$2Fe^{2+} + Fe^{3+} + 8OH^{-} \rightarrow Fe_3O_4 + 4H_2O$$

Chapter 2

Selectivity in Photodynamic Action: Higher Activity of Mitochondria Targeting Photosensitizers in Cancer Cells

2.1. Objectives and Design

Starting of the Meldrum et al. work for mitochondria targeting sensor[137], we designed three different photosensitizers each having different aims. The attachment of triphenylphosphonium[87, 137] moiety is realized as a mitcondria targeting agent, mitochondriotropic[138], and we make us of this particular attachment for this project. Bromination procedure is used to enhance intersystem crossing which also enhances the generation of reactive oxygen species. Eventually, BODIPY core is functionalized with triethylene glycol (TEG) and methoxy units by taking advantage of Knoevenagel condensation; therefore BODIPY based photosensitizers at longer wavelength are synthesized. In order to elucidate the differential cytotoxicity of mitochondria targeting and non-selective photosensitizers, we synthesized the target molecules shown in the following figure.

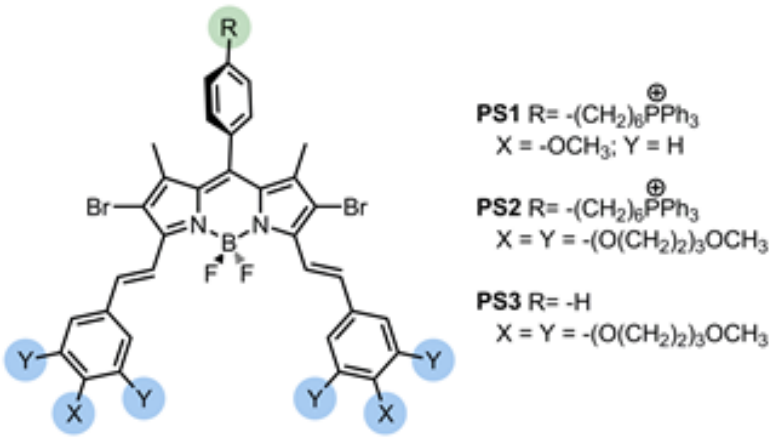

Figure 8. Structures of the photosensitizers (PS1-3) synthesized for elucidating the relevance of membrane potential in mitochondria targeting agents.

The photosensitizers PS1-3, are based on 3,5-distyryl-BODIPY derivatives. Heavy atoms (Br) were incorporated to enhance intersystem crossing efficiency and singlet oxygen quantum yield. PS1 carries a TPP group, but it is without additional solubility enhancers. PS2 was derivatized for an amphiphilic character and TPP group was appended by a meso-phenyl substituent. PS3 is a negative control photosensitizer for mitochondrial targeting. All compounds seemed to be very effective in singlet oxygen generation when excited at 653 nm (LED source) light in the presence of selective singlet oxygen probe 1,3-Diphenylisobenzofuran. The synthesis routes for molecules are indicated in Figure 9-12.

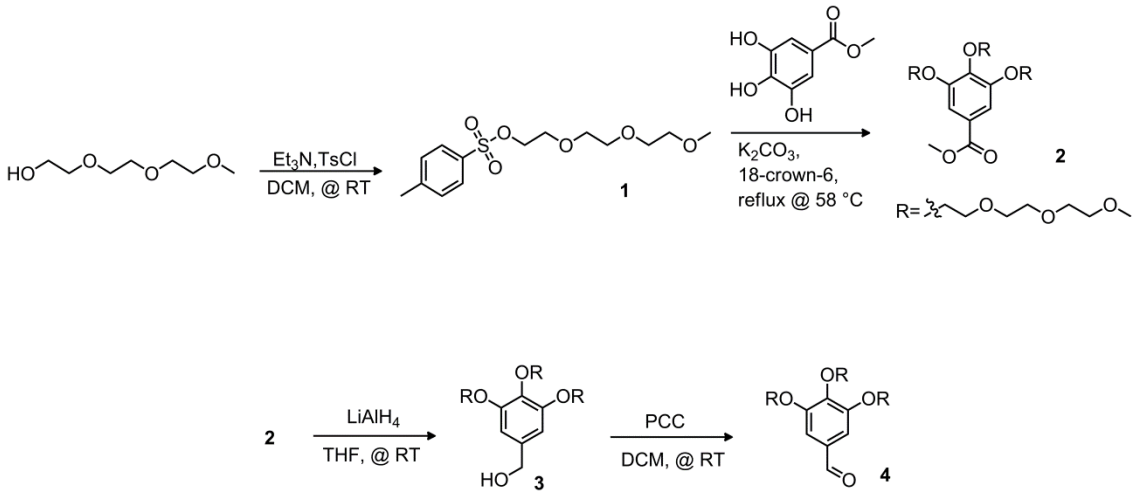

Figure 9. Synthetic pathway for TEG-benzaldehyde.

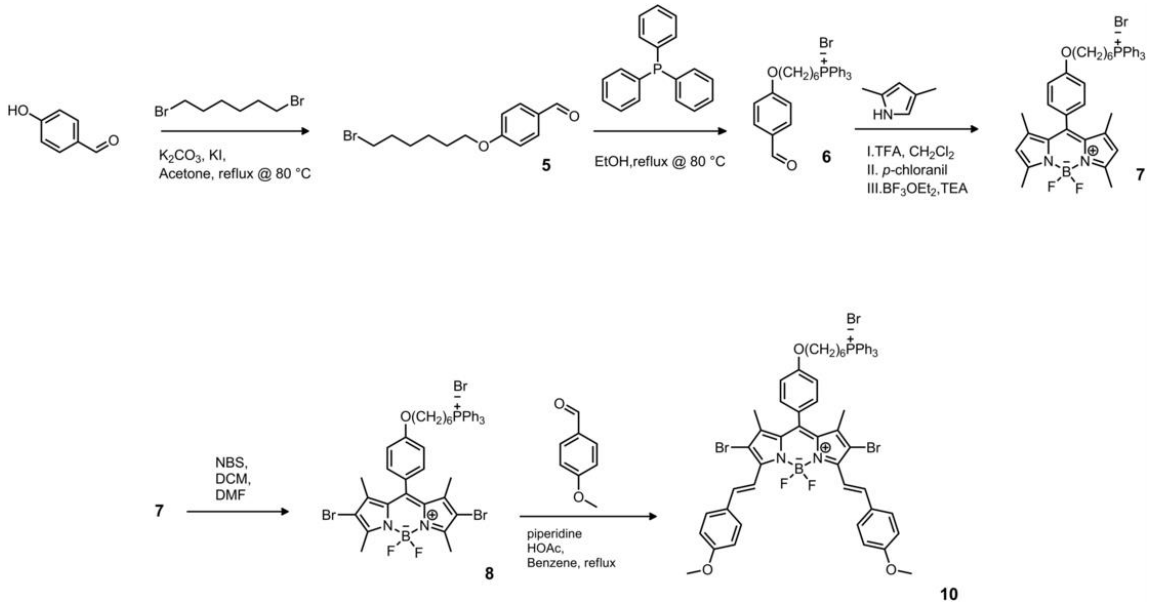

Figure 10. Synthetic pathway for PS1.

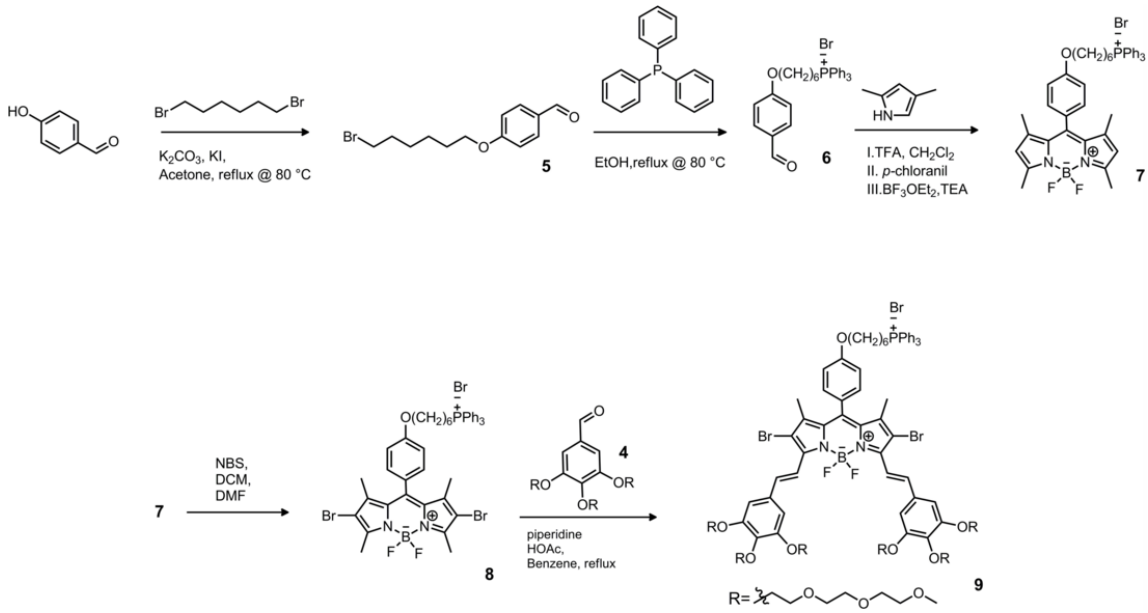

Figure 11. Synthetic pathway for PS2.

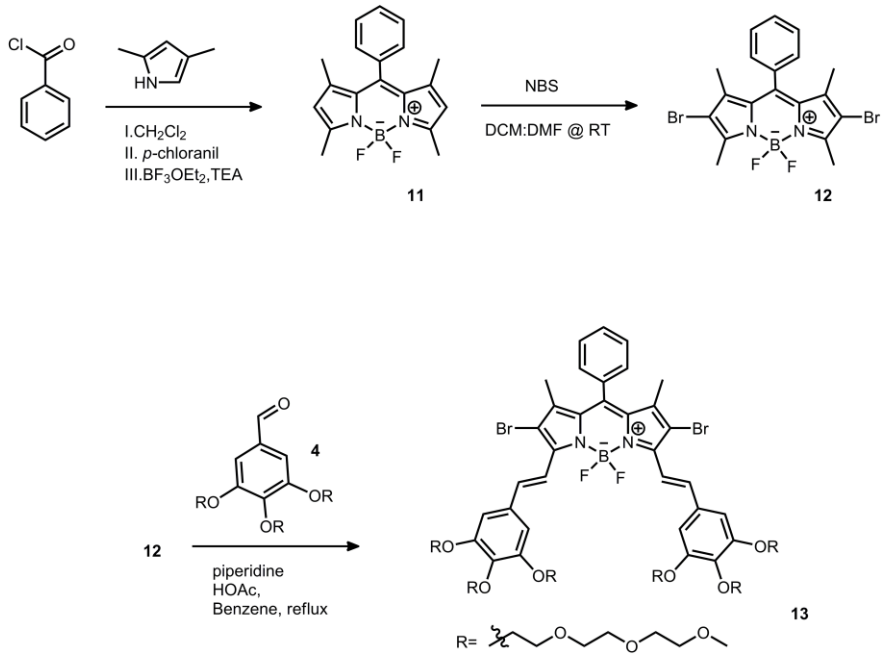

Figure 12. Synthetic pathway for PS3.

2.2. Results and Discussion

In order to assess photophysical characteristics of photosensitizers, absorbance and emission spectra of the compounds were recorded. While the absoption maxima of PS1 was at 666 nm, the absoption maxima of PS2 and PS3 were obtained at 656 nm in DCM at 25 ^{0}C. In excitation wavelength of 620 nm, the emission maxima for PS2 and PS3 were recorded as 679 nm, where the emission maxima for PS1 was recorded as 684 nm in the excitation wavelength of 640 nm, again in DCM at 25^{0}C.

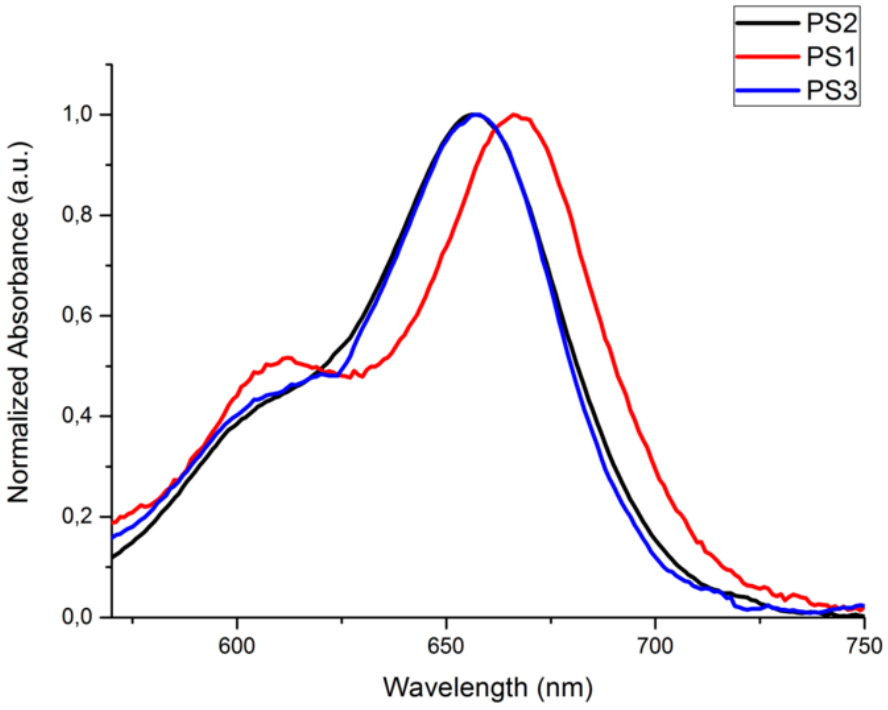

Figure 13. Normalized absorbance spectra of PS1, PS2, and PS3 in DCM at 25 ^{0}C.

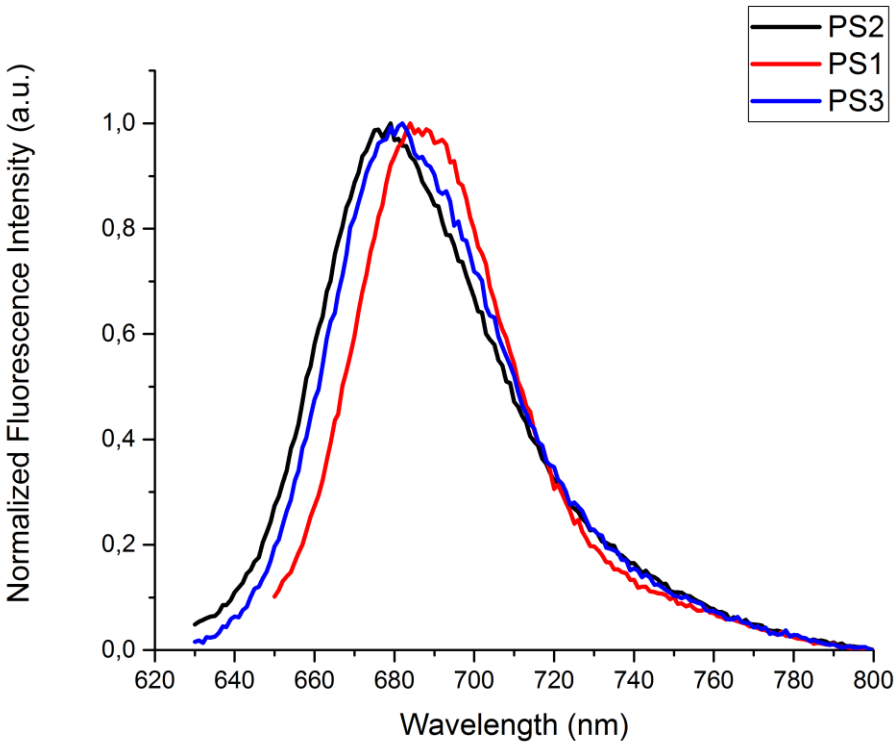

Figure 14. Normalized fluorescence emission spectra of of PS1, PS2, and PS3 in DCM at 25 ^{0}C. Compounds were excited at: λ_{abs} (PS2) = 620 nm, λ_{abs} (PS1)= 640 nm, and λ_{abs} (PS3) = 620 nm.

Singlet oxygen generation and quantum yield calculations has shown that the effectiveness of PS2 compound (which is the main target molecule) is immensely sufficient for PDT. In singlet oxygen generation experiments, 1,3-Diphenylisobenzofuran (DPBF) was used as chemical singlet oxygen trap molecule in oxygen gas bubbled DCM. This procedure includes approximately 1.0 µM photosensitizer (PS1, PS2, or PS3) mixed with trap molecule (approximately 0.4 µM) in

O_2 bubbled DCM. Initially 25 minutes dark measurements were taken for each compund at 5 minutes intervals. This procedure followed by the irridiation of the light of the mixture. Absorbance decrease of trap molecules was monitored revealing singlet oxygen generation in the presence of light and mixture with photosensitizer. Measurements were performed using 653 nm LED and samples were irradiated with the light source from 10 cm distance. The reaction between 1,3-Diphenylisobenzofuran and singlet oxygen is given in following Figure 15.

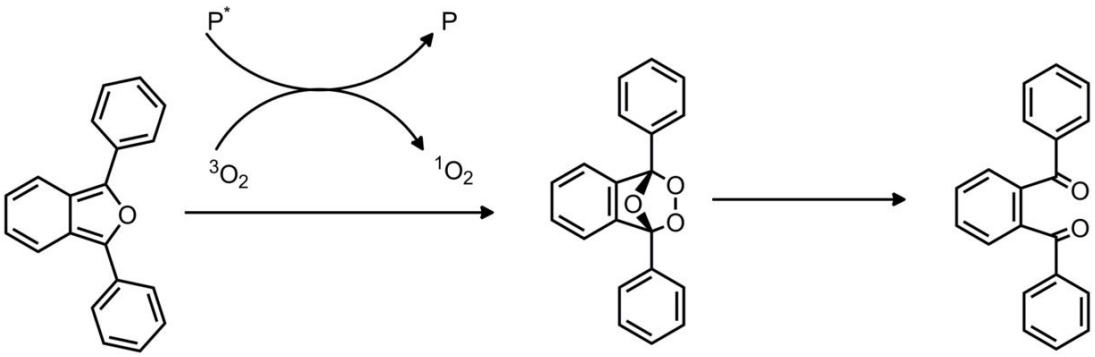

Figure 15. Reaction of singlet oxygen with 1.3-Diphenylisobenzofuran.

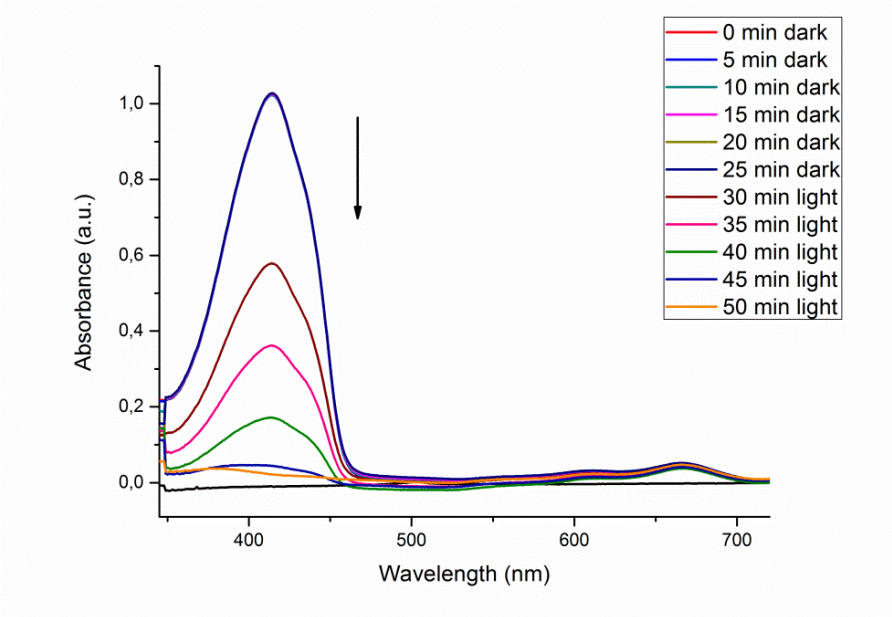

Figure 16. Decrease in absorbance of DPBF (0.4 μM) in DCM in the presence of 1.4 μM PS1 at 653 nm.

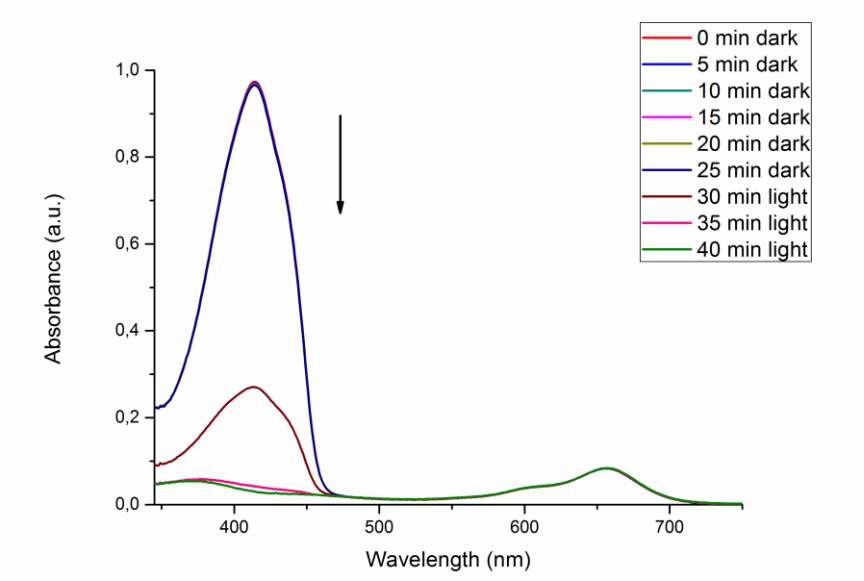

Figure 17. Decrease in absorbance of DPBF (0.4 μM) in DCM in the presence of 0.83 μM PS2 at 653 nm.

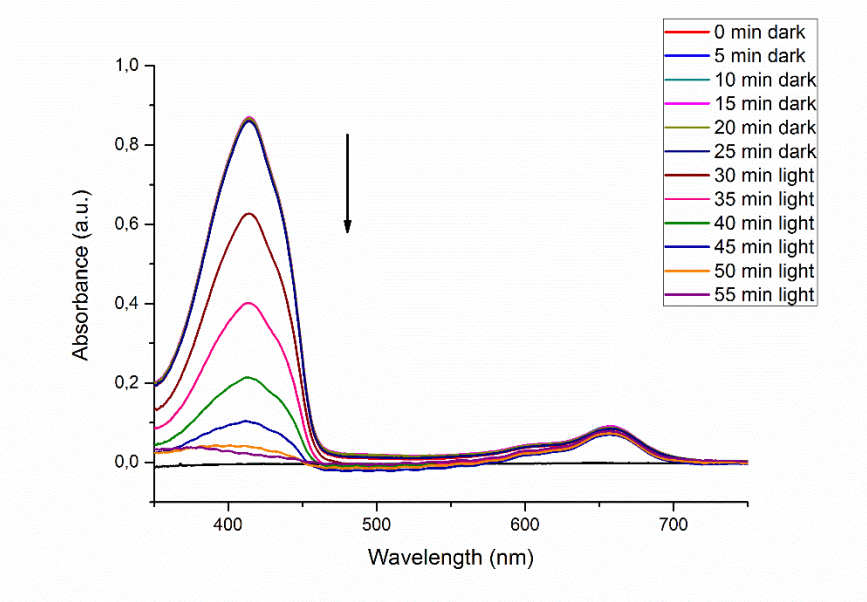

Figure 18. Decrease in absorbance of DPBF (0.4 μM) in DCM in the presence of 1.0 μM PS3 at 653 nm.

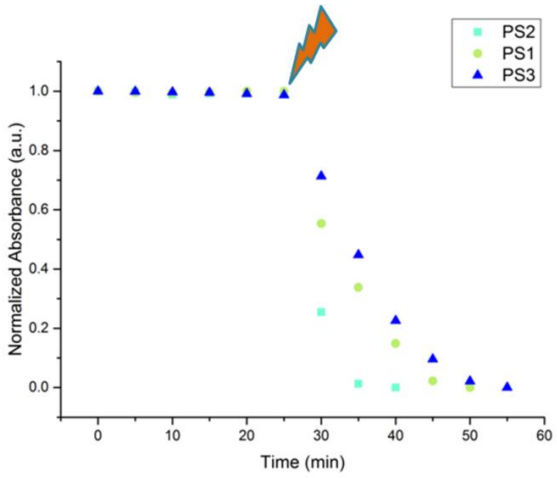

Figure 19. Decreasing absorbance peak for the singlet oxygen trap DPBF at 414 nm with time in oxygen gas bubbled DCM solvent either dark and light reaction conditions in the presence of photosensitizers PS1, PS2, and PS3.

Singlet oxygen quantum yields were calculated according to the literature. 30 minutes oxygen gas bubbled dicholoromethane was used for all the measurements. Relative singlet oxygen quantum yields were calculated compared to Methylene Blue (MB) which has 0.57 singlet oxygen quantum yield in DCM. The absorbance of photosensitizer was adjusted below than 0.2 while the absorbance of DPBF was adjusted around 1.0 in oxygen bubbled DCM. After stabilization of absorbance readings in dark, the absorbance readings were recorded in every 5 minutes by exposing light (653 nm) for 15 minutes. The recorded graph is given below:

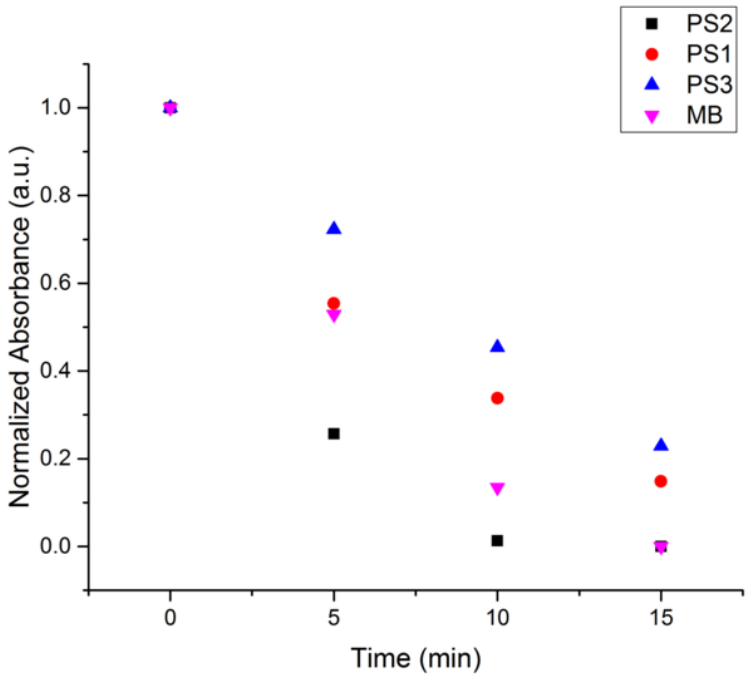

Figure 20. Decreasing absorbance peak for the singlet oxygen trap DPBF at 414 nm with time in oxygen gas bubbled DCM solvent in the light reaction conditions and in the presence of photosensitizers PS1, PS2, and PS3 (Methylene Blue as reference).

The quantum yield of singlet oxygen generation was calculated according to the equation:

$$\Phi_{\Delta}(PS) = \Phi_{\Delta}(MB) \times \frac{m(PS)}{m(MB)} \times \frac{F(MB)}{F(PS)} \times \frac{PF(MB)}{PF(PS)}$$

where PS and MB stands for photosensitizer and Methylene Blue. m is the slope of the difference in change in absorbance of DPBF at absorbance maxima with respect to irradiation time. F is the absorption correction factor, which is given as $F=1-10^{-OD}$ and PF is the absorbed photonic flux. The calculated singlet oxygen quantum yields are given below:

Compounds	Singlet Oxygen Quantum Yields
PS1	0.54
PS2	0.96
PS3	0.34

Figure 21. Relative singlet oxygen quantum yields of photosensitizers PS1, PS2, and PS3 where Methylene Blue is reference.

The effectiveness of organellar targeting was studied using HeLa cells with confocal microscopy. Cell nuclei were stained with Hoechst 33342, and Rhodamine 123 was used for imaging mitochondria, as it is a known fluorescent label for mitochondria. PS1 has low emission intensity, which is most likely due to lower solubility leading to

aggregation with reduced fluorescence quantum yield. However, on excitation of PS1 in cell cultures under irradiation with the light source, there are structural changes in the cell nuclei and mitochondria loses Rhodamine 123 label, suggesting a highly compromised mitochondrial membrane structure. PS2 on the other hand, shows even more revealing results. Since this compound has a higher emission quantum yield, we can clearly see mitochondria being selectively labeled with this photosensitizing agent. On laser irradiation, cell nuclei and mitochondria are damaged and also, there are signs of nuclear condensation. Intracellular localization of the dyes PS2 and PS3 were compared with the known mitochondria label Rhodamine 123. Pearson correlation plots show that PS2 has a 95 % overlap with Rhodamine 123. The photosensitizer PS3, which lacks mitochondria targeting triphenylphosphonium moiety has a lower overlap as expected (81 %).

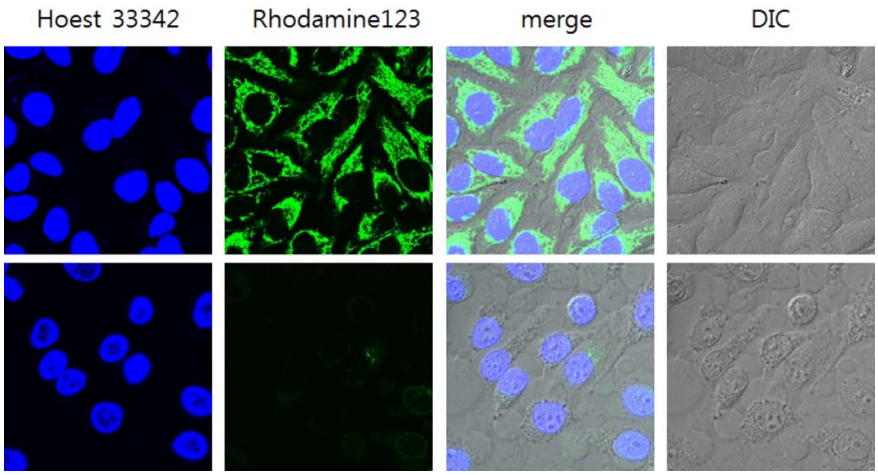

Figure 22. HeLa cells were incubated with 1 μM PS1 for 2 hr and stained with 1ug/mL Hoest33342 and 500 nM Rhodamine 123 for 20 min, then irradiated 655 nm laser (0.6A, 3 min). Fluorescent images were acquired by confocal

microscopy. H33342 (ex. 405 nm/em. 430-455 nm), R123 (ex. 473 nm/em. 490-590 nm).

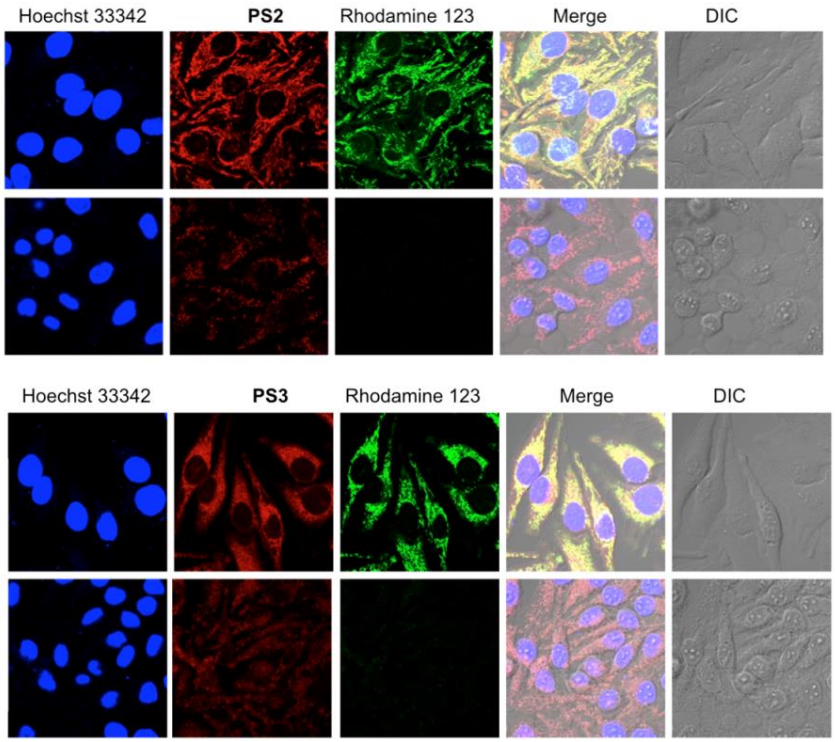

Figure 23. HeLa cells were incubated with 1.0 μM PS2 (top two rows) or PS3 (bottom two rows) for 2 hr and stained with 1.0 μg/mL Hoechst-33342 and 500 nM Rhodamine 123 for 20 min, then irradiated with 655 nm laser (0.433 W/cm^2, 3 min). Fluorescence images were acquired by confocal microscopy. H33342 (ex. 405 nm/em. 430-455 nm), R123 (ex. 473 nm/em. 490-590 nm), PS2/PS3 (ex. 635 nm/em. 655-755nm).

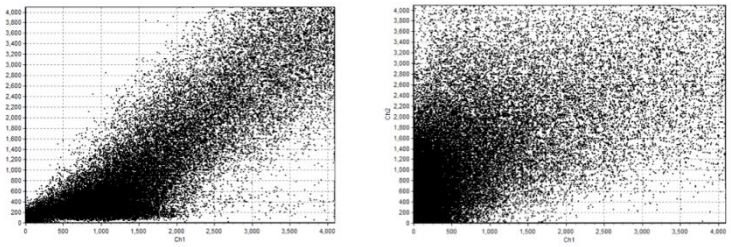

Figure 24. The fluorescence intensity correlation plot of PS2 (left) and PS3 (right) (at 3 μM concentration) with Rhodamine 123 (500 nM) with HeLa cells costained.

We then compared MTT cytotoxicity assay data for the mitochondria targeting agents PS2 and PS3 in HeLa (human cervical cancer) cells and normal cell cultures (NIH3T3: mouse embryo fibroblast cell line and WI38: fibroblast-like fetal lung cell line). The results were particularly striking when the data for 5 nM photosensitizer concentrations with WI38 and HeLa cells were compared (Figure 25). Compound PS2 decrease the survival rate of HeLa cells down to 68 % whereas at the same concentration 97 % of the WI38 cells remained alive (same as the control, considering the margin of error). In fact at all concentrations of the study, HeLa cells were at the lower concentrations of the photosensitizers PS1 and PS2.

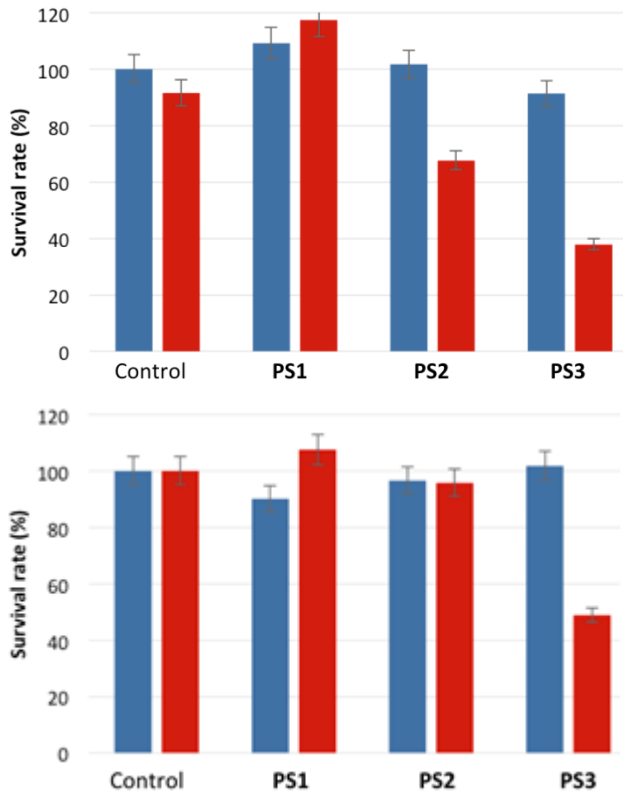

Figure 25. WI38 (top) and HeLa (bottom) cells were incubated with compounds PS1-3 at 5.0 nM concentrations for 2 h, then the cells were irradiated with 655 nm laser (0.433 W/cm^2, 5 min), followed by 24 h incubation. Cell survival rates were determined by standard MTT assays. Controls are cells subjected to same conditions except for any added photosensitizer. Experiments were run in triplicate.

2.3. Conclusion

In conclusion, we have successfully demonstrated that mitochondria targeted photosensitizers have a larger propensity for localizing in the cancer cell mitochondria as opposed to normal cells. Thus, explicit targeting of mitochondria is very likely to generate a therapeutic advantage due to the differences in membrane characteristics of the mitochondria. Selectivity achieved in this way is very valuable, as there is an established strong correlation between tumor cell malignancy and the negative deviation of the mitochondrial potential. As a consequence, it is reasonable to expect PDT agents making use of this unique character to be more effective and to minimize unintended damage to normal cells. This in turn, may reduce or even eliminate some of the potential side effects and complications. Work to realize these goals are in progress in our laboratories.

2.4. Experimental Details

2.3.1. Materials

All reagents and solvents were purchased from commercial suppliers and used without further purification. Reactions were monitored by thin layer chromatography using Merck TLC Silica gel 60 F_{254}. Column chromatography was performed by using Merck Silica Gel 60 (particle size: 0.040-0.063 mm, 230-400 mesh ASTM).

2.3.2. Instrumentation

The ^{1}H and ^{13}C NMR spectra were recorded using Bruker DPX-400 (operating at 400 MHz for ^{1}H NMR and 100 MHz for ^{13}C NMR) at 298 K using deuterated solvents with tetramethylsilane (TMS) as internal standard. Chemical shifts were reported in parts per million (ppm) and coupling constants (*J* values) are given in Hz. Splitting patterns are indicated as follow s, singlet; d, doublet; t, triplet; m, multiplet. The UV-Vis absorption spectra were performed by using Varian Cary-100 Bio UV-Vis spectrophotometer. Fluorescence Emission Spectra were performed by using Varian Cary Eclipse fluorescence spectrophotometer. Mass spectra were recorded with Agilent Technologies 6224 TOF LC/MS.

2.3.3. Cell Imaging by Confocal Microscopy

HeLa cells were seeded in a 35-mm glass bottomed dishes at a density of 3 × 105 cells per dish in culture media. To test organelle localization, HeLa cells were incubated with 3 μM samples and stained with 500 nM Rhodamine 123 for 20 min. After washed with DPBS, the cells were imaged by confocal microscopy (Fluoview 1200, Olympus, Japan) with R123 (ex. 473 nm/em. 490-590 nm) and samples (ex.635nm/em. 655-755nm). Except for overnight culture, cell experiments were tested in HBSS (Hanks' balanced salt solution) media. To test apoptosis, HeLa cells were incubated with 1 μM samples for 2 hr and stained with 1μg/mL Hoest33342 and 500 nM Rhodamine 123 for 20 min, then irradiated 655 nm laser (0.433 W/cm^2) for 3 min. Fluorescence images were acquired by confocal microscopy with Hoest33342 (ex. 405 nm/em. 430-455 nm), R123 (ex. 473 nm/em. 490-590 nm) and samples (ex.635nm/em. 655-755nm).

2.3.4. Cytotoxicity Test

Cells were seeded in a 96-well plate with culture media. After overnight culture, cells were incubated with samples for 2 h and washed with DPBS. After irradiation with 655 nm NIR laser (0.433 W/cm^2) for 3 min, cells were incubated another 24 h. To identify cell viability, 0.5 mg/mL of MTT (Sigma) media was added to the cells for 4 h, and the produced formazan was dissolved in 0.1 mL of dimethylsulfoxide (DMSO) and read at OD 650 nm with a Spectramax Microwell plate reader.

2.3.5. Synthesis

Compound 1:

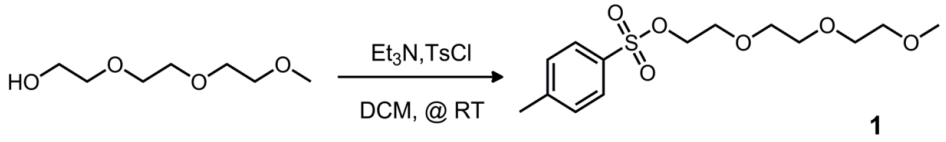

Figure 26. Synthesis of Compound 1.

Triethylene glycol monomethyl ether (10.0 g, 61.0 mmol) was dissolved in 100.0 mL dicholoromethane and 13.0 mL triethylamine. *p*-Toluenesulfonyl chloride (12.0 g, 63.0 mmol) in 20.0 mL dicholoromethane was added dropwise to the previous mixture in an ice bath. The reaction mixture allowed to stir for 12 hours at room temperature. After that, the reaction mixture was extracted with DCM and water. The organic layer was combined and dried over anhydrous Na_2SO_4. After removal of the solvent by rotary evaporator, the crude product was purified by silica gel column chromatography with DCM: Methanol (98:2, v/v) as the eluent. The product was obtained in light yellow liquid form in 90% yield (17.5 g, 55.0 mmol). ^{1}H NMR (400 MHz, $CDCl_3$): δ 7.81 (d, *J*=8.0 Hz, 2H), 7.35 (d, *J*=8.0 Hz, 2H), 4.17 (t, *J*=4.8 Hz, 2H), 3.70 (t, *J*= 4.8 Hz, 2H), 3.63-3.59 (m, 6H), 3.57-3.52 (m, 2H), 3.38 (s, 3H), 2.46 (s, 3H). ^{13}C NMR (100 MHz, $CDCl_3$): δ 144.7, 132.9, 129.7, 129.2, 126.3, 127.6, 71.6, 70.3, 70.2, 70.1, 69.3, 68.3, 58.5, 21.2. MS (TOF-ESI) m/z calcd for $C_{14}H_{22}O_6S$: 319.1210 $[M+H]^+$, found: 319.1172 $[M+H]^+$, Δ=11.67 ppm.

Compound 2:

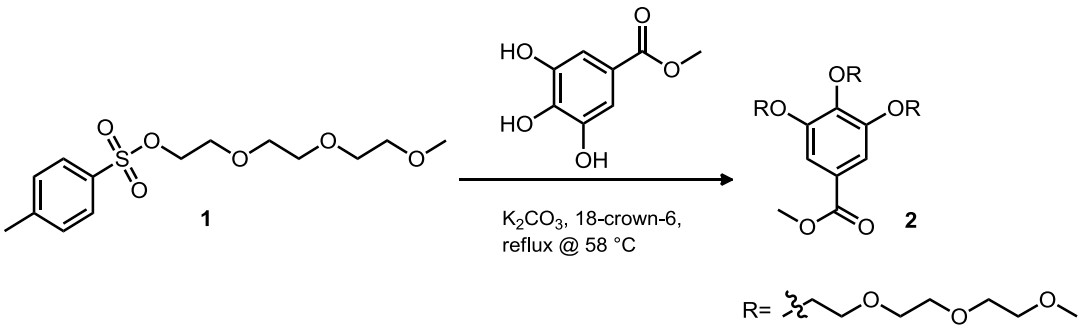

Figure 27. Synthesis of Compound 2.

Compound **1** (15.0 g, 47.0 mmol) and methyl-3,4,5-trihydroxybenzoate (2.75 g, 15.0 mmol) were dissolved in 60.0 mL acetone. Then K_2CO_3 (8.3 g, 60.0 mmol) and catalytic amount of 18-crown-6 were added to the reaction mixture. The reaction mixture was refluxed for 18 hours at 58 ^oC. Reaction is monitored by TLC. Then, the reaction mixture was extracted with ethyl acetate and brine solution. Organic layer was combined and dried over anhydrous Na_2SO_4. After removal of the solvent by rotary evaporator, the crude product was purified by silica gel column chromatography with EtOAc:MeOH (95:5, v/v) as the eluent. The product was obtained in light yellow liquid form in 15 % yield (4.5 g, 7.0 mmol). ^1H NMR (400 MHz, $CDCl_3$): δ 7.31 (s, 2H), 4.25-4.19 (m, 6H), 3.90 (s, 3H), 3.88 (t, *J*= 5.2 Hz, 4H), 3.81(t, *J*= 5.2 Hz, 2H), 3.76.371 (m, 6H), 3.69-3.61 (m, 12H), 3.57-3.54 (m, 6H), 3.39 (s, 9H). ^{13}C NMR (100 MHz, $CDCl_3$): δ 166.6, 152.3, 142.7, 124.9, 109.1, 72.4, 71.9, 70.84, 70.70, 70.69, 70.58, 70.57, 70.55, 70.53, 69.6, 68.9, 59.0, 52.1. MS (TOF-ESI) m/z calcd for $C_{29}H_{50}O_{14}$: 617.3144 $[M+Na]^+$, found: 645.3034 $[M+Na]^+$, Δ=8.98 ppm.

Compound 3:

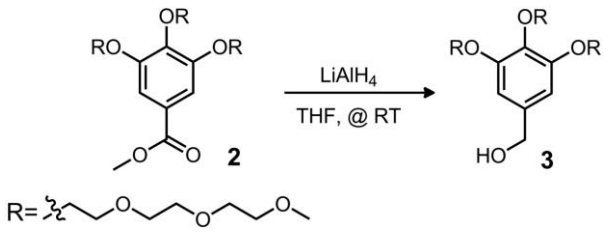

Figure 28. Synthesis of Compound 3.

Compound **2** (2.33 g, 3.7 mmol) was dissolved in freshly distilled 20.0 mL THF in a flask in an ice bath. Then, $LiAlH_4$ (0.28 g, 7.4 mmol) was added to the solution and allowed to stir at room temperature for 12 hours. After 12 hours, excess $LiAlH_4$ was quenched with cold water. The mixture was extracted with ethyl acetate and brine solution. Organic layer was dried over anhydrous Na_2SO_4. After removal of the solvent by rotary evaporator, the cude product was purified by silica gel column chromatography with EtOAc:MeOH (90:10, v/v) as the eluent. The product was obtained in light yellow liquid form in 81% yield (1.91 g, 3.0 mmol). ^{1}H NMR (400 MHz, $CDCl_3$): δ 6.64 (s, 2H), 4.58 (s, 2H), 4.18 (t, *J* = 5.2 Hz, 4H), 4.15 (t, *J* = 6.0 Hz, 2H), 3.85 (t, *J*= 5.2 Hz, 4H), 3.80 (t, *J* = 5.2 Hz, 2H), 3.75-3.72 (m, 6H), 3.68-3.64 (m, 12H), 3.57-3.54 (m, 6H), 3.39 (s, 9H). ^{13}C NMR (100 MHz, $CDCl_3$): δ 152.7, 137.9, 136.6, 106.8, 72.3, 71.97, 71.94, 70.79, 70.72, 70.70, 70.55, 70.51, 69.8, 68.9, 65.3, 58.9. MS (TOF-ESI) m/z calcd for $C_{28}H_{50}O_{13}$: 617.3144 $[M+Na]^+$, found 617.3204 $[M+Na]^+$, Δ=-9.89 ppm.

Compound 4:

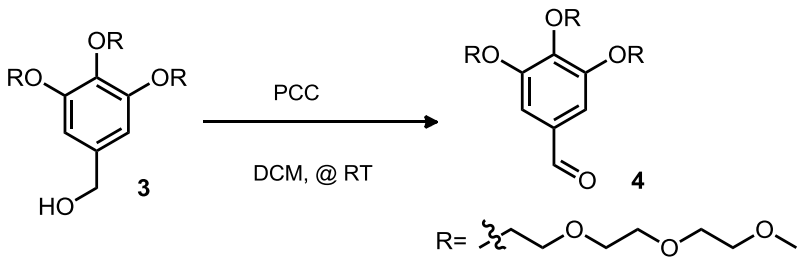

Figure 29. Synthesis of Compound 4.

Compound **3** (0.706 g, 1.2 mmol) was dissolved in 25.0 mL DCM in a round-bottom flask. Then, pyridinum cholorochromate (PCC) (0.65 g, 3.0 mmol) was added to the solution and allowed to stir at room temperature for approximately 45 minutes. After removal of the solvent by rotary evaporator, the crude product was purified by silica gel column chromatography with EtOAc:MeOH (95:5, v/v) as the eluent. The product was obtained in light yellow liquid form in 83% yield (0.59 g, 0.99 mmol). ^{1}H NMR (400 MHz, $CDCl_3$): δ 9.80 (s, 1H), 7.12 (s, 2H), 4.25 (t, *J* = 4.8 Hz, 2H), 4.20 (t, *J* = 4.4 Hz, 4H), 3.86 (t, *J* = 4.4 Hz, 4H), 3.79 (t, *J*= 4.4 Hz, 2H), 3.73-3.68 (m, 6H), 3.66-3.60 (m, 12H), 3.53-3.50 (m, 6H), 3.35 (s, 9H). ^{13}C NMR (100 MHz, $CDCl_3$): δ 190.9, 153.0, 144.4, 131.6, 109.0, 72.5, 71.9, 70.8, 70.9, 70.7, 70.59, 70.55, 70.52, 69.6, 69.0, 58.9. MS (TOF-ESI) m/z calcd for $C_{28}H_{48}O_{13}$: 615.2987 $[M+Na]^+$, found: 615.3030 $[M+Na]^+$, Δ=-7.11 ppm.

Compound 5:

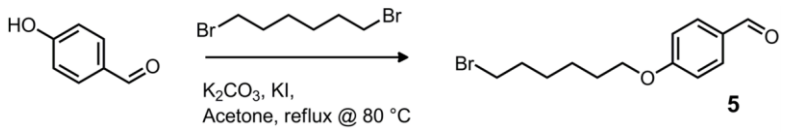

Figure 30. Synthesis of Compound 5. [137]

4-hydroxybenzaldehyde (5.0 g, 40.94 mmol) and 1,6-dibromohexane (15.0 mL, 97.51 mmol) were dissolved in acetone and then K_2CO_3 (22.0 g, 159.0 mmol) was added to the mixture. Then, catalytic amount of KI was added to the reaction mixture and it was refluxed at 61 ^{o}C for 24 hours. Reaction is monitored by TLC. After removal of the solvent by rotary evaporator, the crude product was purified by silica gel column chromatography with DCM:Hexane (2:1, v/v) as the eluent. The product was obtained in light yellow liquid form in 48% yield (5.6 g, 19.7 mmol). ^{1}H NMR (400 MHz, $CDCl_3$): δ 9.88 (s, 1H), 7.83 (d, *J*= 8.8 Hz, 2H), 6.99 (d, *J* = 8.8 Hz, 2H), 4.05 (t, *J*= 6.4 Hz, 2H), 3.43 (t, *J* = 6.8 Hz, 2H), 1.94-1.80 (m, 4H), 1.53-1.50 (m, 4H). ^{13}C NMR (100 MHz, $CDCl_3$): δ 190.8, 164.1, 131.9, 129.8, 114.7, 68.1, 33.8, 32.6, 28.9, 27.9, 25.2. MS (TOF-ESI) m/z calcd for $C_{13}H_{17}BrO_2$: 285.0485 $[M+H]^+$, found: 285.0522 $[M+H]^+$, Δ=-13.26 ppm.

Compound 6:

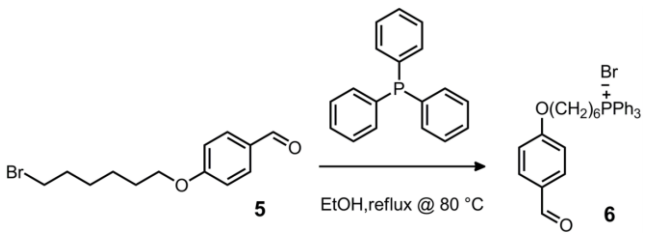

Figure 31. Synthesis of Compound 6. [137]

Compound **5 (**1.0 g, 3.51 mmol) and triphenylphosphine (0.92 g, 3.51 mmol) were dissolved in 30.0 mL ethanol. The mixture was refluxed for 72 hours at 80 ^{o}C. Reaction was monitored by TLC. After removal of the solvent by rotary evaporator, the crude product was purified by silica gel column chromatography with DCM:MeOH (95:5, v/v) as the eluent. The product was obtained in yellow liquid form in 46 % yield (0.9 g, 1.6 mmol). ^{1}H NMR (400 MHz, $CDCl_3$): δ 9.79 (s, 1H), 7.81-7.65 (m, 17H), 6.91 (d, *J* = 8.4 Hz, 2H), 3.97 (t, *J* = 6.4 Hz, 2H), 3.80-3.68 (m, 2H), 1.73-1.70 (m, 4H), 1.64-1.61 (m, 2H), 1.47-1.42 (m, 2H). ^{13}C NMR (100 MHz, $CDCl_3$): δ 190.9, 164.2, 135.1, 135.0, 133.7, 133.6, 131.9, 130.6, 130.5, 129.7, 128.7, 117.8, 114.8, 68.2, 30.1, 29.9, 28.6, 25.5, 22.9. MS (TOF-ESI) m/z calcd for $C_{31}H_{32}O_2P$: 467.2134 [M^x+], found: 467.2151 [M^x+], Δ=3.7 ppm.

Compound 7:

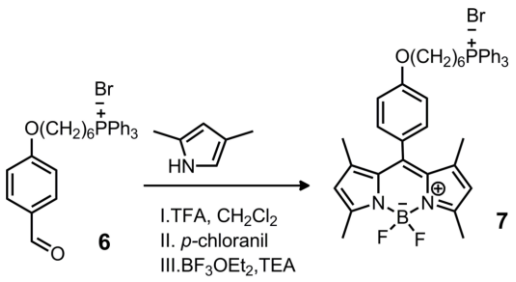

Figure 32. Synthesis of Compound 7. [137]

Dicholoromethane (300.0 mL) was bubbled with argon for 30 minutes. Then, Compound **6** (1.1 g, 2.0 mmol) and 2,4-dimethylpyrrole (0.52 mL, 3.96 mmol) were added sequentially at 10 min intervals under argon. After that, 2 drops of trifluoroacetic acid (TFA) were added to the reaction mixture. The reaction mixture was stirred at room temperature for 12 hours. Then, *p*-chloranil (0.487 g, 2.0 mmol) was added to the reaction mixture and allowed to stir for another 2 hours. Finally, triethylamine (5.0 mL, 36.0 mmol) and BF_3OEt_2 (5.0 mL, 39.5 mmol) were added sequentially at 30 minutes interval. After 30 minutes, the reaction mixture was washed with water (2 x 100.0 mL); 0.1 M HCl (2 x 100.0 mL); water (2 x 100.0 mL); %10 Na_2CO_3 (2 x 100.0 mL) and then water (2 x 100.0 mL). Organic layer was combined and dried over anhydrous Na_2SO_4. After removal of the solvent by rotary evaporator, the crude product was purified by silica gel column chromatography with DCM:MeOH (98:2, v/v) as the eluent. The product was obtained in orange-red solid form in 21% yield (0.31 g, 0.41 mmol). ^{1}H NMR (400 MHz, $CDCl_3$): δ 7.85-7.71 (m, 15H), 7.14 (d, *J*=8.4 Hz, 2H), 6.98

(d, *J*=8.8 Hz, 2H), 5.98 (s, 2H), 4.01-3.97 (m, 2H), 3.42-3.31 (m, 2H), 2.56 (s, 6H), 1.85-1.76 (m, 2H), 1.76-1.70 (m, 4H), 1.59-1.50 (m, 2H), 1.44 (s, 6H,). ^{13}C NMR (100 MHz, $CDCl_3$): δ 159.7, 155.2, 143.2, 142.0, 135.1, 135.1, 133.5, 133.4, 131.9, 130.6, 130.5, 129.1, 126.8, 124.7, 118.7, 117.8, 115.1, 67.9, 30.3, 29.7, 28.9, 25.8, 22.59, 22.55, 22.1, 21.6, 14.6, 14.5. MS (TOF-ESI) m/z calcd for $C_{43}H_{45}BF_2N_2OP$: 684.3372 [M^x+], found: 684.3442 [M^x+], Δ=-10.31 ppm.

Compound 8:

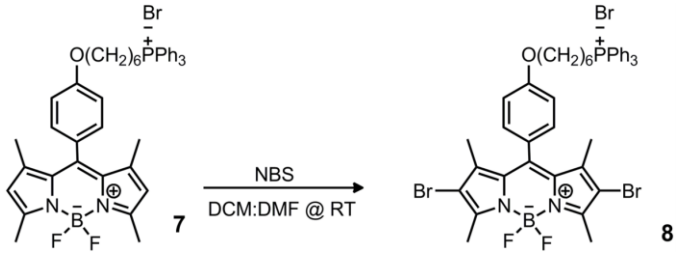

Figure 33. Synthesis of Compound 8.

Compound **7** (0.298 g, 0.4 mmol) was dissolved in DMF:DCM (5.0 mL:15.0 mL) solution in a round-bottom flask. At the same time, N-Bromosuccinimide (NBS) (0.17 g, 0.1 mmol) was dissolved in sufficient amount of DCM. Then, NBS solution was added dropwise to the previous solution and allowed to stir at room temperature for approximately 1 hour. The reaction mixture was extracted with DCM and water. Organic layer was combined and dried over anhydrous Na_2SO_4. After removal of the solvent by rotary evaporator, the crude product was purified by silica gel column chromatography with DCM:MeOH (95:5, v/v) as the eluent. The product was obtained

in pinkish solid form in 80% yield (0.26 g, 0.32 mmol).). ^{1}H NMR (400 MHz, $CDCl_3$): δ 7.85-7.70 (m, 15H), 7.12 (d, *J* = 8.4 Hz, 2H), 7.02 (d, *J* = 8.8 Hz, 2H), 4.03 (t, *J* = 6.4 Hz, 2H), 3.43-3.34 (m, 2H), 2.61 (s, 6H), 1.84-1.79 (m, 2H), 1.75-1.61 (m, 4H), 1.58-1.51 (m, 2H), 1.43 (s, 6H). ^{13}C NMR (100 MHz, $CDCl_3$): δ 160.1, 153.6, 140.7, 135.1, 135.1, 133.5, 133.4, 130.6, 130.5, 129.0, 126.1, 118.7, 117,8, 115.4, 67.9, 30.1, 29.9, 28.9, 25.4, 22.6, 22.1, 21.6, 13.9, 13.3. MS (TOF-ESI) m/z calcd for $C_{43}H_{43}BBr_2F_2N_2OP$: 840.1717 M^{n}+, found: 840.1620 M^{n}+, Δ= -5.83 ppm.

Compound 9 (PS2):

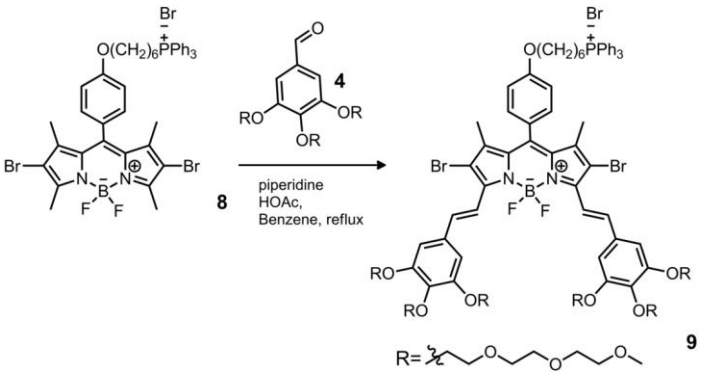

Figure 34. Synthesis of Compound 9.

Compound **8** (0.111 g, 0.120 mmol) and Compound **4** (0.136 g, 0.231 mmol) were dissolved in 20.0 mL benzene in a round-bottom flask. After that, 0.25 mL piperidine and 0.25 mL glacial acetic acid added to the previous solution and allowed to reflux by using Dean-Stark apparatus at 98 ^{o}C. The reaction was followed by TLC until all BODIPY was consumed. After the reaction was completed, it was extracted with DCM

and water. Organic layer was dried over anhydrous Na_2SO_4. After removal of the solvent by rotary evaporator, the crude product was purified by silica gel column chromatography with DCM:MeOH (92.5:7.5, v/v) as the eluent. The product was obtained in green solid form in 48% yield (0.095 g, 0.046 mmol). ^{1}H NMR (400 MHz, $CDCl_3$): δ 7.95 (d, *J* = 16.4 Hz, 2H), 7.85-7.71 (m, 15H), 7.50 (d, *J* = 16.4 Hz, 2H), 7.16 (d, *J* = 8.4 Hz, 2H), 7.04 (d, *J* = 8.8 Hz, 2H), 6.87 (s, 4H), 4.25-4.20 (m, 12H), 4.05 (t, *J*=6.4 Hz, 2H), 3.88 (t, *J* = 5.2 Hz, 8H), 3.83 (t, *J* = 5.2 Hz, 4H), 3.76-3.73 (m, 12H), 3.70-3.63 (m, 26H), 3.58-3.52 (m, 12H), 3.40 (s, 6H), 3.37 (s, 12H), 1.87-1.82 (m, 2H), 1.78-1.69 (m, 4H), 1.58-1.55 (m, 2H), 1.49 (s, 6H).^{13}C NMR (100 MHz, $CDCl_3$): δ 159.1, 152.9, 148,2, 140.2, 139.3, 135.1, 133.5, 133.4, 132.6, 130.6, 130.5, 129.3, 118.5, 117.6, 117.3, 115.8, 107.7, 72.4, 71.94, 71.91, 70.79, 70.65, 70.50, 69.7, 69.1, 59.0, 31.9, 30.3, 29.7, 28.9, 25.5, 21.6, 14.1. MS (TOF-ESI) m/z calcd for $C_{99}H_{135}BBr_2F_2N_2O_{25}P$: 1989.7628 $[M+H]^+$, found: 1989.7550 $[M+H]^+$, Δ= 3.92 ppm.

Compound 10 (PS1):

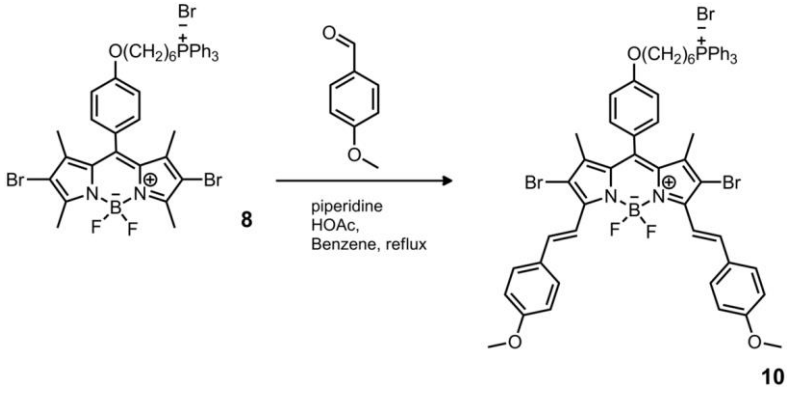

Figure 35. Synthesis of Compound 10.

Compound **8** (0.146 g, 0.158 mmol) was dissolved in 20.0 mL benzene in a round-bottom flask. Then, 4-methoxybenzaldehyde (48.0 μL, 0.395 mmol) was added to the reaction mixture. After that, 0.25 mL piperidine and 0.25 mL glacial acetic acid added to the previous solution and allowed to reflux by using Dean-Stark apparatus at 97 ^{o}C. The reaction was followed by TLC until all BODIPY was consumed (approximately 2 hours). After the reaction was completed, it was extracted with DCM and water. Organic layer was dried over anhydrous Na_2SO_4. After removal of the solvent by rotary evaporator, the crude product was purified by silica gel column chromatography with DCM:MeOH (90:10, v/v) as the eluent. The product was obtained in green solid form in 88% yield (0.016 g, 0.014 mmol). ^{1}H NMR (d_6-DMSO): δ 8.05 (d, *J* = 16.4 Hz, 2H), 7.93-7.76 (m, 15H), 7.60 (d, *J* = 8.8 Hz, 4H), 7.47 (d, *J* = 16.8 Hz, 2H), 7.31 (d, *J* = 8.8 Hz, 2H), 7.09 (d, *J* = 8.8 Hz, 2H), 7.05 (d, *J* = 8.8 Hz, 4H), 4.00 (t, *J* = 6.0 Hz, 2H), 3.81 (s, 6H), 3.63-3.56 (m, 2H), 1.74-1.67 (m, 2H), 1.62-1.53 (m, 4H), 1.50-1.44 (m, 2H), 1.37 (s, 6H). ^{13}C NMR (100 MHz, d_6-DMSO): δ 161.2, 160.1, 147.8, 141.3, 140.4, 138.8, 135.4, 134.11, 134.01, 132.5, 130.8, 130.7, 130.1, 129.5, 129.2, 126.1, 119.5, 118.6, 115.7, 115.6, 115.2, 109.9, 68,1, 55.6, 30.2, 30.0, 28.8, 25.3, 22.3, 20.9, 20.5, 14.0. MS (TOF-ESI) m/z calcd for $C_{59}H_{56}BBr_2F_2N_2O_3P$: 1076.2414 M, found: 1076.2488 M, Δ= -6.85 ppm.

Compound 11:

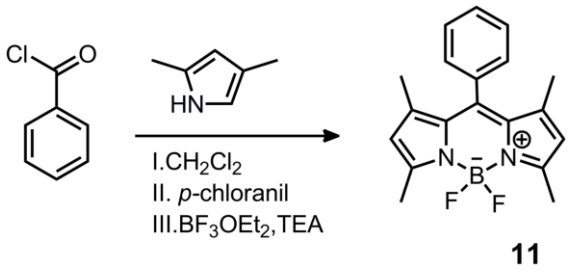

Figure 36. Synthesis of Compound 11.[141]

Dichloromethane (300.0 mL) was degased with argon for 30 minutes. Benzoyl chloride (10.0 mL, 10.0 mmol) and 2,4-dimethylpyrrole (0.52 mL, 3.96 mmol) were added sequentially at 10 min intervals under argon. The reaction mixture was stirred at room temperature for 24 hours. Then, triethylamine (10.0 mL, 72.0 mmol) and BF_3OEt_2 (10.0 mL, 79.0 mmol) were added sequentially at 30 min interval. The reaction mixture was allowed to stir another 24 hours. Then, it was washed with saturated Na_2CO_3 solution (3 x 200.0 mL) and then water (3 x 200.0 mL). Organic layer was combined and dried over anhydrous Na_2SO_4. After removal of the solvent by rotary evaporator, the crude product was purified by silica gel column chromatography with hexane as the eluent. The product was obtained in orange-gold solid form in 35% yield (0.41 g, 1.28 mmol). ^{1}H NMR (400 MHz, $CDCl_3$): δ 7.51-7.48 (m, 3H), 7.29-7.27 (m, 2H), 6.00 (s, 2H), 2.58 (s, 6H), 1.39 (s, 6H). ^{13}C NMR (100 MHz, $CDCl_3$): δ 155.4, 143.2, 141.8, 134.9, 129.1, 128.9, 127.9, 121.3, 14.6, 14.3. MS (TOF-ESI) m/z calcd for $C_{19}H_{19}BF_2N_2$: 324.1718 $[M+H]^+$, found: 324.1664 $[M+H]^+$, Δ=16.61 ppm.

Compound 12:

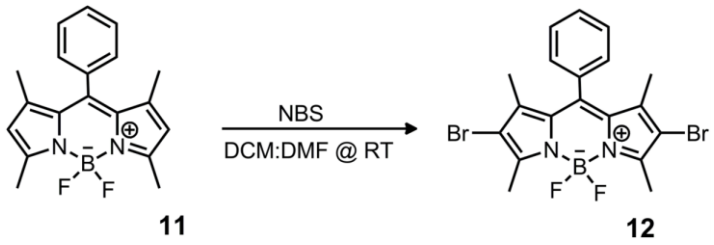

Figure 37. Synthesis of Compound 12.

Compound **11** (0.114 g, 0.352 mmol) was dissolved in DMF:DCM (5.0 mL:15.0 mL) solution in a round-bottom flask. At the same time, NBS (0.16 g, 0.899 mmol) was dissolved in sufficient amount of DCM. Then, NBS solution was added dropwise to the previous solution in an ice bath and the reaction mixture was allowed to stir at room temperature for approximately 2 hours. The reaction mixture was extracted with water and DCM. Organic layer was dried over anhydrous Na_2SO_4. After removal of the solvent by rotary evaporator, the crude product was purified by silica gel column chromatography with Hexane:EtOAc (90:10, v/v) as the eluent. The product was obtained in pinkish solid form in 61% yield (0.104 g, 0.21 mmol) ^{1}H NMR (400 MHz, $CDCl_3$): δ 7.56-7.54 (m, 3H), 7.29-7.27 (m, 2H), 2.63 (s, 6H), 1.39 (s, 6H). ^{13}C NMR (100 MHz, $CDCl_3$): δ 153.9, 142.1, 140.6, 134.4, 130.4, 129.6, 129.4, 127.8, 111.6, 14.1, 13.7. MS (TOF-ESI) m/z calcd for $C_{19}H_{17}BBr_2F_2N_2$: 517.9487 $[M+K]^+$, found: 517.9548 $[M+K]^+$, Δ= -11.77 ppm.

Compound 13 (PS3):

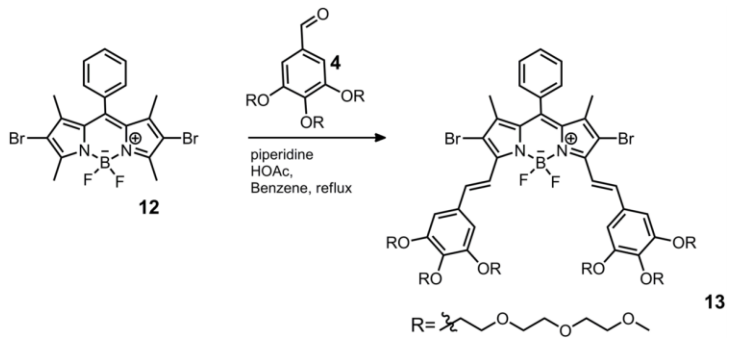

Figure 38. Synthesis of Compound 13.

Compound **12** (0.107 g, 0.221 mmol) and Compound **4** (0.326 g, 0.553 mmol) were dissolved in 20.0 mL benzene in a round-bottom flask. After that, 0.25 mL piperidine and 0.25 mL glacial acetic acid added to the previous solution and allowed to reflux by using Dean-Stark apparatus at 98 ^{o}C. The reaction was followed by TLC until all BODIPY was consumed (approximately 1.5 hours). After the reaction was completed, it was extracted with DCM and water. Organic layer was dried over anhydrous Na_2SO_4. After removal of the solvent by rotary evaporator, the crude product was purified by silica gel column chromatography with EtOAc:MeOH (85:15, v/v) as the eluent. The product was obtained in green solid form in 40% yield (0.144 g, 0.088 mmol). ^{1}H NMR (400 MHz, $CDCl_3$): δ 7,97 (d, *J* = 16.4 Hz, 2H), 7.59-7.54 (m, 2H), 7.52 (d, *J* = 16.8 Hz, 2H), 7.34-7.31 (m, 3H), 6.88 (s, 4H), 4.27-4.21 (m, 12H), 3.88 (t, *J* = 4.8 Hz, 8H), 3.83 (t, *J* = 5.6 Hz, 4H), 3.77-3.74 (m, 12H), 3.70-3.63 (m, 26H), 3.58-3.53 (m, 12H), 3.40 (s, 6H), 3.37 (s, 12H), 1.45 (s, 6H).^{13}C NMR (100 MHz, $CDCl_3$): δ 151.9, 148.5, 141.3, 140.3, 139.5, 134.8, 132.3, 129.6, 129.5, 128.3, 117.3, 110.7, 107.8, 72.5, 71.96, 71.92,

70.81, 70.69, 70.67, 70.58, 70.54, 70.52, 69.7, 69.1, 59.0, 58.9, 13.8. MS (TOF-ESI) m/z calcd for $C_{75}H_{109}BBr_2F_2N_2O_{24}$: 1650.5726 $[M+Na]^+$, found: 1650.5965 $[M+Na]^+$, Δ= -14.46 ppm.

Chapter 3

Preparation of Metastable Endoperoxides for Singlet Oxygen Release on Iron Oxide Nanoparticles

3.1. Objectives and Design

The main idea of this chapter is to introduce another project of us which has the goal of the singlet oxygen generation by magnetic heating of anthracene endoperoxide in the presence of iron oxide nanoparticle. The previous work of Akkaya laboratory (Kolemen et al.)[139] accomplished the similar purpose by making use of plasmonic heating of gold nanorods; by following the footsteps of this work, we designed a novel drug which unites both singlet oxygen and magnetic fluid hyperthermia therapy. In the design of molecule, the stability of iron oxide was regulated with PAA attachment. Then, the stabilized MNP's was PEGylated in order to fulfill the desired water-solubility for biological studies. On the basis of 9,10-dipenylanthracenes were proved to be very stable at room temperature, the endoperoxide unit was chosen from 9,10-diphenylanthraces. After the synthesis of parts finalized, both units were conjugated to each other. The final endoperoxide and its cycloreversed anthracene version are given in the Figure 39.

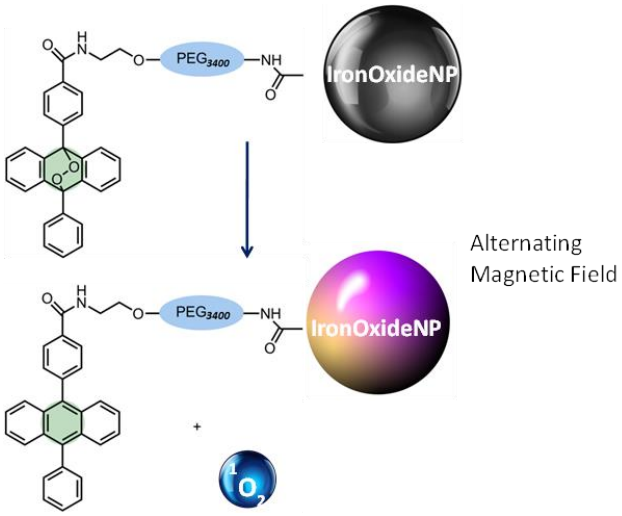

Figure 39. The target product and cycloreversed anthracene derivative (resulting from applied alternating magnetic field).

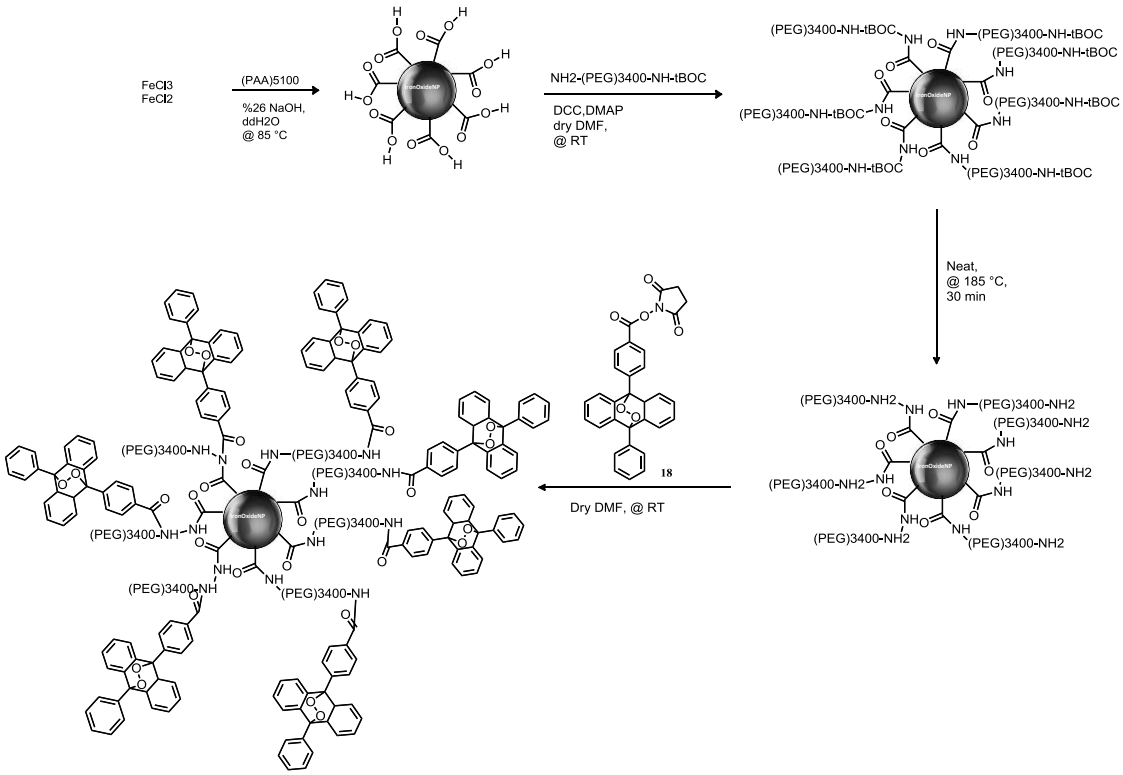

Figure 40. Synthetic pathway for target molecule.

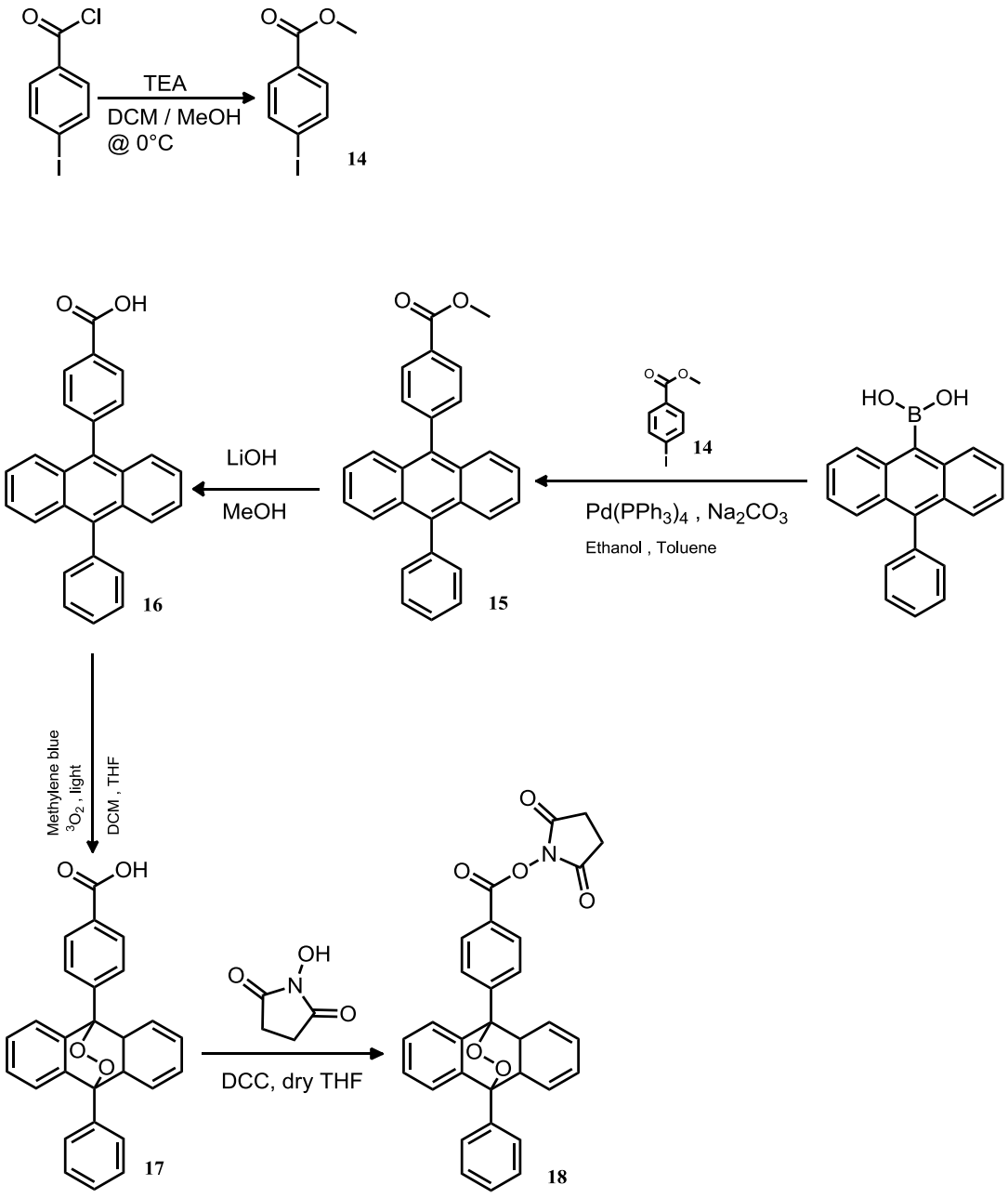

Figure 41. Synthetic pathway for anthracene-endoperoxide.

3.2. Results and Discussion

To assess the particle core sizes, hydrodynamic sizes, and zeta potentials of synthesized compounds in water, TEM and Zeta measurements were recorded. It was observed that both hydrodynamic volume and size of the particles were in the desired range. However, aggregation problem was also faced due to the highly polymeric design of coatings. According to TEM images, the size of Fe_3O_4 nanoparticles were observed between 6-11 nm. The average size of the nanoparticles was determined as 8 nm.

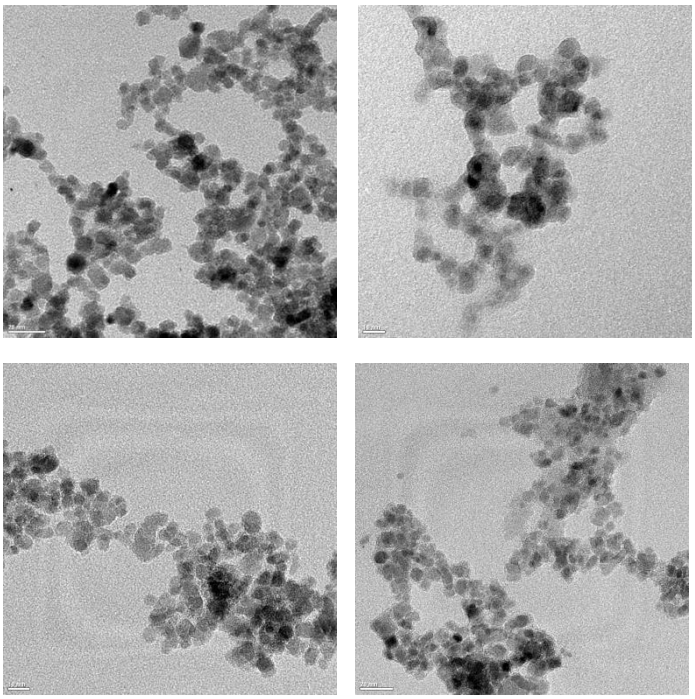

Figure 42. TEM images of Fe_3O_4 cores- 1) Top- Left: decorated with PAA; 2) Top- Right: decorated with PAA-NH-$(PEG)_{3400}$-NH-tBoc**,** 3) Bottom- Left: decorated with PAA-NH-$(PEG)_{3400}$-NH_2; 4) Bottom- Right: PAA-NH_2-$(PEG)_{3400}$-NH-anthracene endoperoxide.

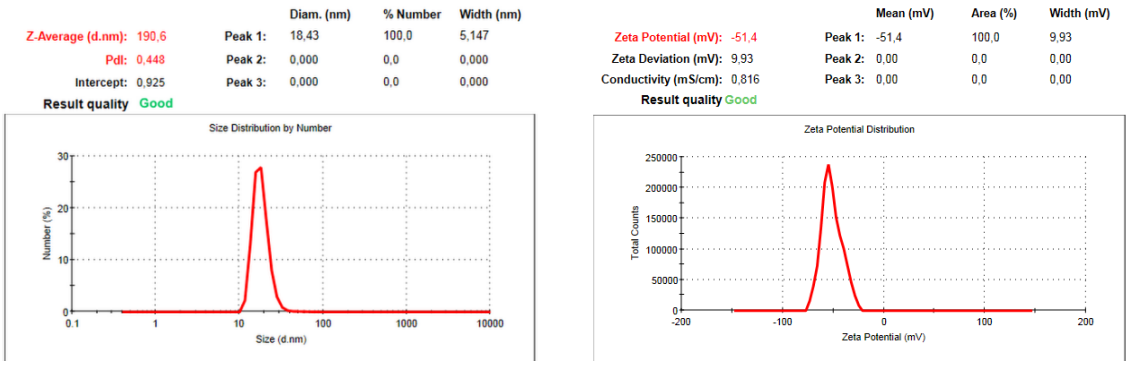

Figure 43. Left: Hydrodynamic size; Right: Zeta potential value of the Fe_3O_4 nanopartciles decorated with PAA (pH=5.5).

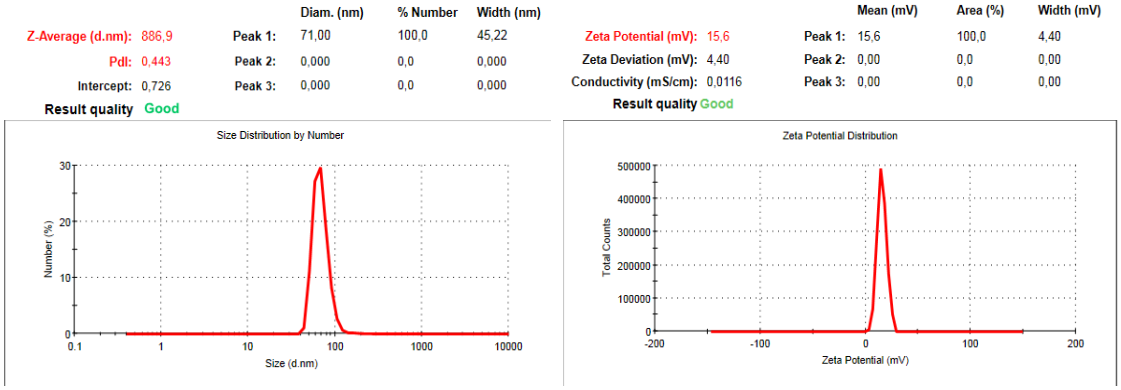

Figure 44. Left: Hydrodynamic size; Right: Zeta potential value of the Fe_3O_4 nanopartciles decorated with PAA-NH-$(PEG)_{3400}$-NH-tBoc (pH=12).

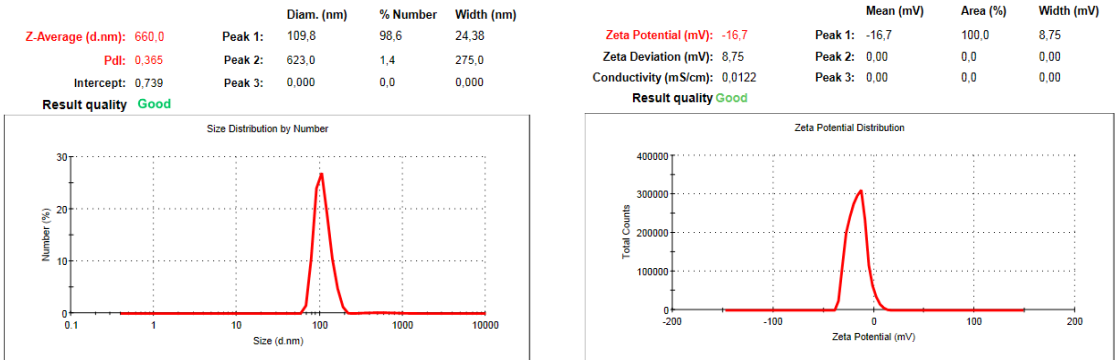

Figure 45. Left: Hydrodynamic size; Right: Zeta potential value of the Fe_3O_4 nanopartciles decorated with PAA-NH-$(PEG)_{3400}$-NH_2 (pH=10).

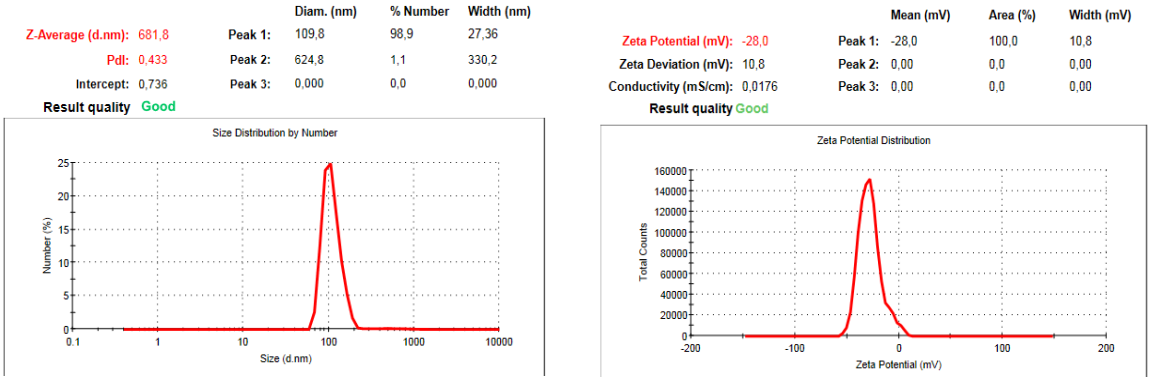

Figure 46. Left: Hydrodynamic size; Right: Zeta potential value of the Fe_3O_4 nanopartciles PAA-NH_2-$(PEG)_{3400}$-NH-anthracene endoperoxide (pH=6).

Endoperoxide formation absorbance graph constructed during the reaction taking place. Samples from reaction mixture were taken and analyzed for 0, 20, 40, 60, 120, 180, 240, 300 and 360 minutes. The disappearance of characteristic triplet absorption of anthracene depictured of endoperoxide formation by distrupting aromaticity. In singlet oxygen generation experiments, thermal cycloreversion of anthracene-endoperoxide is followed by temperature change. The sample was heated in DMSO in an oil bath and absorbance data of taken samples were recorded for 20, 50, 80 and 110 ^{0}C. The reappearance of triplet absorption pattern just above 80 ^{0}C shows the cycloreversion reaction by yielding the parent anthracene compound. After the target molecule was synthesized, the same thermal cycloreversion procedure in DMSO applied at 110 ^{0}C and the cycloreversion was detected in the first 5 minutes. The data collection was unfavourable for the final compound, due to light scattering of iron oxide nanoparticles. However, we were managed to observe triplet absorbance pattern again (shown in Figure 48).

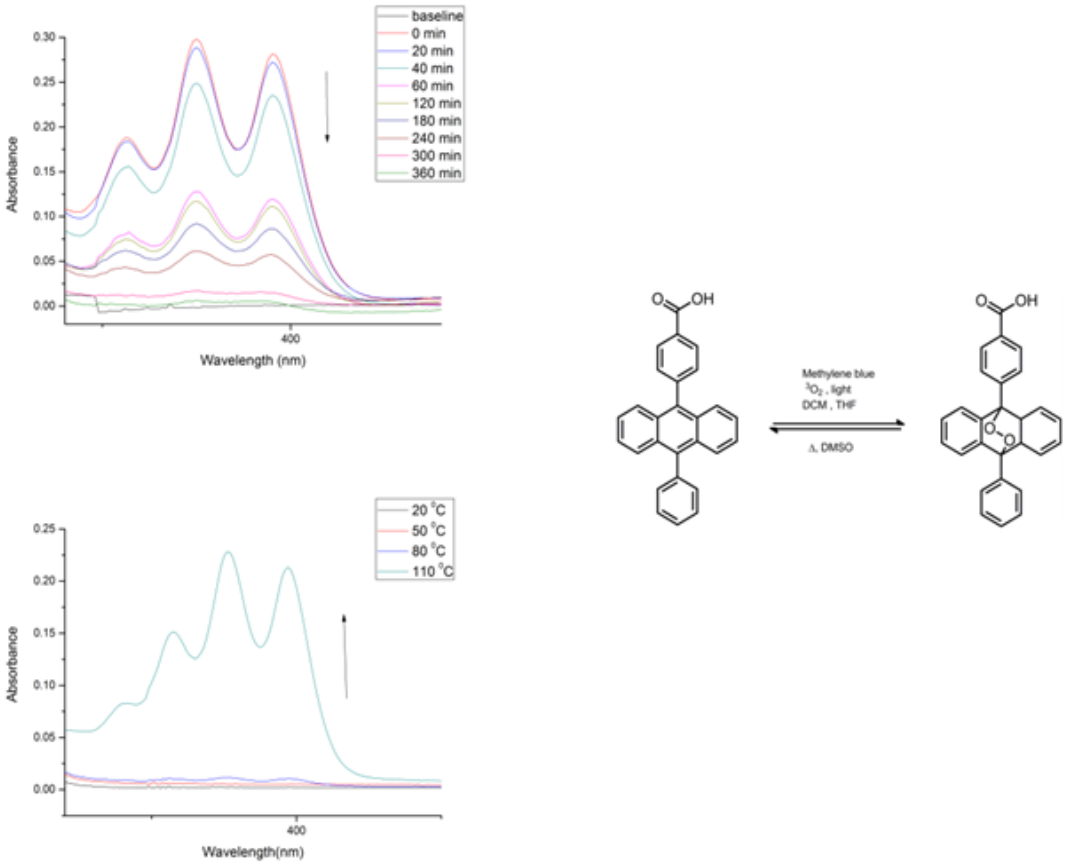

Figure 47. Top: Absorption spectra that is taken during the endoperoxide formation reaction of Compound 17.

Bottom: Thermolysis of endoperoxide - Compound 17 to parent Compound 16.

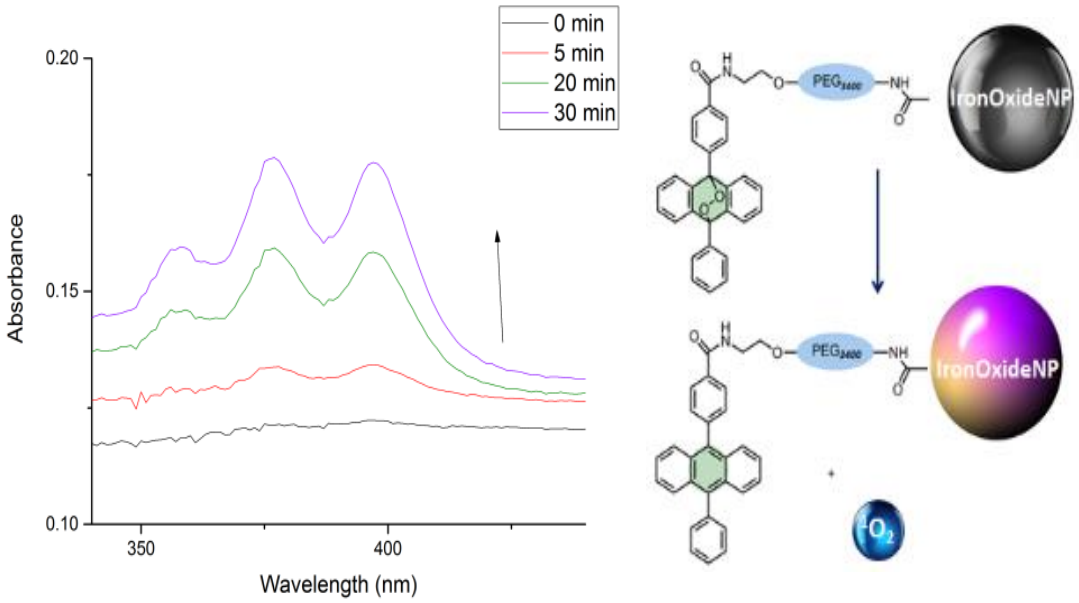

Figure 48. Thermolysis of target endoperoxide - Compound 22 at 110 °C with time.

3.3. Conclusion

In conclusion, we have successfully demonstrated that target compound has been synthesized and characterized. Singlet oxygen generation was achieved with both the endoperoxide compound itself and with the MNP-attached endoperoxide. In vitro experimentation was concluded by thermolysis with regular heating. Magnetic heating will be applied by our collaborators in Sabancı University. After the in vivo cell experimentation, dependent on the outcomes, further experimentation on lab rats is planning. Alternative methods to PDT are in progress with cycloreversion of endoperoxides are in progress in our laboratories.

3.4. Experimental Details

3.3.1. Materials

All reagents and solvents were purchased from commercial suppliers and used without further purification. Reactions were monitored by thin layer chromatography using Merck TLC Silica gel 60 F_{254}. Column chromatography was performed by using Merck Silica Gel 60 (particle size: 0.040-0.063 mm, 230-400 mesh ASTM). NH_2-$(PEG)_{3400}$-NH-tBoc was purchased from Laysan Bio, Inc. Poly (acrylic acid sodium salt/mw=5100) was purchased from Sigma-Aldrich. (10-phenylanthracen-9-yl)boronic acid was purchased from Fluorochem, Inc.

3.3.2. Instrumentation

The ^{1}H and ^{13}C NMR spectra were recorded using Bruker DPX-400 (operating at 400 MHz for ^{1}H NMR and 100 MHz for ^{13}C NMR) at 298 K using deuterated solvents with tetramethylsilane (TMS) as internal standard. Chemical shifts were reported in parts per million (ppm) and coupling constants (*J* values) are given in Hz. Splitting patterns are indicated as follow s, singlet; d, doublet; t, triplet; m, multiplet. The UV-Vis absorption spectra were performed by using Varian Cary-100 Bio UV-Vis spectrophotometer. Mass spectra were recorded with Agilent Technologies 6224 TOF LC/MS. The size and zeta potentials of SPIONs were both assessed by using Malvern Zetasizer Nano ZS. All zeta measurements were taken by using 0.005 wt% of nanoparticles in distilled water. ATR-FTIR spectra were performed on Bruker Platinum ATR/Alpha model. The size of SPIONs was measured through transmission electron microscope- TEM (FEI Tecnai G2 F30, S-TWIN) at 200 kV.

3.3.3 Synthesis

Compound 14:

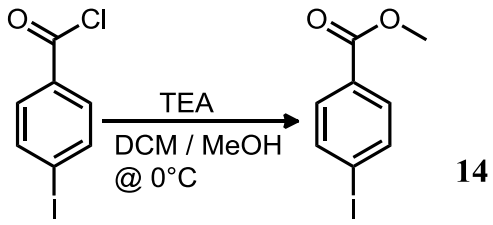

14

Figure 49. Synthesis of Compound 14.[142]

4-iodobenzoylchloride (1.43 g, 5.37 mmol) was dissolved in 3.0 mL dicholoromethane. Triethylamine (2.3 mL, 16.59 mmol) and methanol (1.1 mL, 27.16 mmol) were added in an ice bath. The reaction mixture allowed to stir for 30 minutes at 0 °C. After that, the reaction mixture was poured into ice-water mixture and extracted with DCM. Organic layer was washed with 1 M hydrochloric acid and water. The organic layer was combined and dried over anhydrous $MgSO_4$. After removal of the solvent by rotary evaporator, the crude product was purified by silica gel column chromatography with Hexane:DCM (3:1, v/v) as the eluent. The product was obtained in white solid form with 93% yield (1.31 g, 5.0 mmol). ^{1}H NMR (400 MHz, $CDCl_3$): δ 7.82 (d, J = 8.0 Hz, 2H) 7.76 (d, J = 8.0 Hz, 2H), 3.93 (s, 3H). ^{13}C NMR (100 MHz, $CDCl_3$): δ 166.6, 137.7, 131.0, 129.6, 100.7, 52.3. MS (TOF-ESI) m/z calcd for $C_8H_7IO_2$: 300.9133 $[M+K]^-$, found: 300.9144 $[M+K]^-$, Δ=-3.66 ppm.

Compound 15:

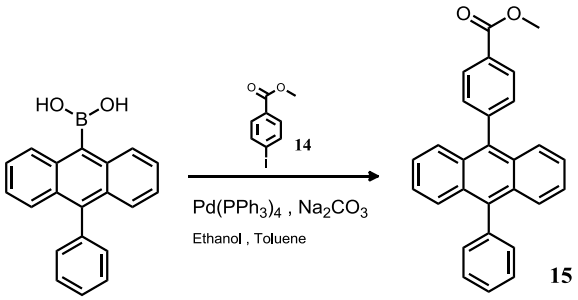

Figure 50. Synthesis of Compound 15.[139]

(10-phenylanthracen-9-yl)boronic acid (0.3 g, 1.0 mmol), methyl 4-iodobenzoate (Compound **14)** (0.26 g, 1.0 mmol) and K_3PO_4 (0.25 g, 1.2 mmol) were dissolved in 2.5 mL degassed toluene. The reaction mixture allowed to stir up to 80 °C, followed by the addition of $Pd(PPh_3)_4$ (0.115 g, 10^{-4} mmol) as toluene solution with syringe. Reaction is monitored by TLC up to reactants were consumed totally. Then, the reaction mixture was allowed to cool at room temperature, quenched with water and extracted with ethyl acetate (x3). Organic layer was combined and dried over anhydrous Na_2SO_4. After removal of the solvent by rotary evaporator, the crude product was purified by silica gel column chromatography with Hexane:DCM (2:1, v/v) as the eluent. The product was obtained in white solid form with 30% yield (0.103 g, 0.3 mmol). ^{1}H NMR (400 MHz, $CDCl_3$): δ 8.35 (d, *J* = 12.0 Hz, 2H), 7.78-7.75 (m, 2H), 7.69-7.60 (m, 7H), 7.54-7.51 (m, 2H), 7.40-7.36 (m, 4H), 4.07 (s, 3H). ^{13}C NMR (100 MHz, $CDCl_3$): δ 167.1, 144.4, 138.9, 137.8, 135.8, 131.58, 131.29, 129.87, 129.77, 129.57, 129.49, 128.5, 127.61, 127.15, 126.5, 125.41, 125.15, 52.3. MS (TOF-ESI) m/z calcd for $C_{28}H_{20}O_2$: 389.1536 $[M+H]^+$, found: 389.1431 $[M+H]^+$, Δ=26.97 ppm.

Compound 16:

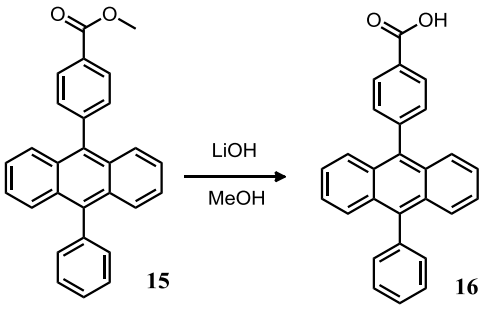

Figure 51. Synthesis of Compound 16.[139]

Compound **15** (0.103g, 0.3 mmol) was dissolved in 7.5 mL methanol. Then, 2 M LiOH solution in 1.5 mL water was added to the solution. The reaction mixture was allowed to stir at 60 °C for 3 hours. Solution was acidified to pH 2.0 followed by precipitation in water. Filtrate was collected and dried. The crude product was purified by silica gel column chromatography with EtOAc:MeOH (85:15, v/v) as the eluent. The product was obtained in white solid form with 77% yield (0.085 g, 0.23 mmol). ^{1}H NMR (400 MHz, DMSO): δ 8.23 (d, *J* = 8.0 Hz, 2H), 7.70-7.66 (m, 2H), 7.64-7.58 (m, 5H), 7.56-7.53 (m, 2H), 7.49-7.42 (m, 6H). ^{13}C NMR (100 MHz, DMSO): δ 167.7, 143.5, 138.5, 137.6, 135.9, 131.79, 131.34, 130.76, 130.09, 129.63, 129.39, 129.16, 128.3, 126.95, 126.58, 126.28, 126.06. MS (TOF-ESI) m/z calcd for $C_{27}H_{18}O_2$: 374.1302 M, found: 374.1270 M, Δ=9.6 ppm.

Compound 17:

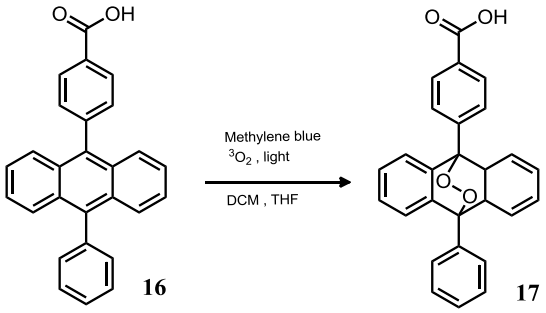

Figure 52. Synthesis of Compound 17.[139]

Compound **16** (0.74 g, 0.2 mmol) was dissolved in 7.5 mL DCM:THF (5:2.5 mL). The reaction mixture was cooled to – 78 °C. Methylene blue (0.006 g, 0.02 mmol) was added into the solution and mixture was stirred for 6 hours under oxygen atmosphere. During the reaction water-cooled 400 W Hg arc lamp (white light irradiation) was used. After removal of the solvent by rotary evaporator, the crude product was purified by silica gel column chromatography with DCM:MeOH (95:5, v/v) as the eluent. The product was obtained in white solid form with 82% yield (0.65 mg, 0.16 mmol). ^{1}H NMR (400 MHz, DMSO): δ 8.27 (d, *J* = 8.0 Hz, 2H), 7.78 (d, *J* = 8.0 Hz, 2H), 7.74-7.70 (m, 2H), 7.66-7.61 (m, 3H), 7.35-7.31 (m, 4H), 7.11-7.06 (m, 4H). ^{13}C NMR (100 MHz, DMSO): δ 167.4, 140.1, 139.7, 137.3, 132.6, 131.5, 130.0, 129.12, 129.07, 128.49, 128.44, 127.92, 127.53, 123.61, 123.44, 99.7, 83.7. MS (TOF-ESI) m/z calcd for $C_{27}H_{20}O_4$: 407.1289 $[M-H]^-$, found: 407.1224 $[M-H]^-$, Δ=15.92 ppm.

Compound 18:

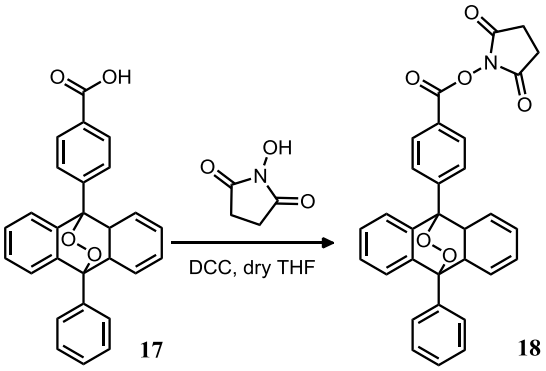

Figure 53. Synthesis of Compound 18.[143]

Compound **17** (0.33 g, 0.8 mmol) was dissolved in freshly distilled 10.0 mL THF. N-hydroxysuccinimide (0.120 g, 1.04 mmol) and dicyclohexylcarbodiimide (0.214 g, 1.04 mmol) were added to the reaction mixture. Reaction is monitored by TLC. Then, the mixture was filtered and the solution was collected. After removal of the solvent by rotary evaporator, the crude product was purified by silica gel column chromatography with DCM:MeOH (97:3, v/v) as the eluent. The product was obtained in white solid form with 72% yield (0.292 g, 0.58 mmol). ^{1}H NMR (400 MHz, DMSO): δ 8.43 (d, *J* = 8.0 Hz, 2H), 7.95 (d, *J* = 8.0 Hz, 2H), 7.75-7.71 (m, 2H), 7.67-7.62 (m, 3H), 7.38-7.31 (m, 4H), 7.13-7.09 (m, 4H), 2.96 (s, 4H). ^{13}C NMR (100 MHz, $CDCl_3$): δ 169.1, 161.6, 140.33, 140.11, 139.3, 132.7, 130.6, 128.41, 128.22, 127.99, 127.84, 127.46, 125.2, 123.77, 123.09, 84.30, 83.98, 25.7. MS (TOF-ESI) m/z calcd for $C_{31}H_{23}NO_6$: 505.1531 [M^x-], found: 505.1553 [M^x-], Δ=-4.3 ppm.

Compound 19:

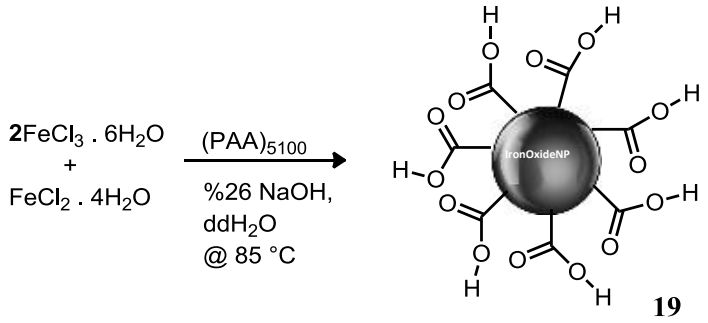

Figure 54. Synthesis of Compound 19.[140]

Iron Oxide nanoparticles were synthesized according to Massart's[140] procedure with some modifications: distilled water (30.0 mL) was degassed with argon for 30 minutes. Then, poly (acrylic acid sodium salt/mw=5100) (1.2 g, 2.35 mmol) was added and dissolved in water for 30 minutes under argon. Subsequently, iron(III) chloride hexahydrate (1.5 g, 5.55 mmol) and iron(II) chloride tetrahydrate (0.55 g, 2.77 mmol) was added to the reaction mixture for 15 minutes under argon. After adjusting the temperature to 85 °C, the reaction mixture was stirred for 2 hours. Then, %26 NaOH solution (4.6 mL) was added to the solution under vigorous stirring and allowed to stir for 1 more hour. The resulting suspension of PAA-IONPs was then allowed to wait overnight with magnet, washed with water for several times, and lyophilized to have PAA coated magnetite nanoparticles.

Compound 20:

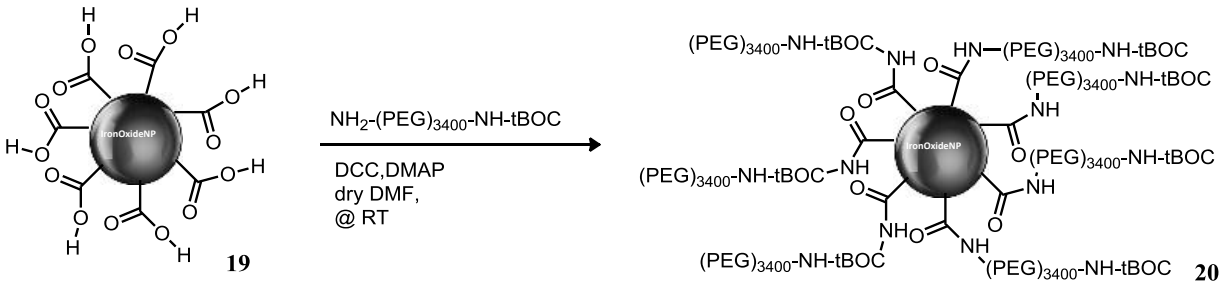

Figure 55. Synthesis of Compound 20.

Compound **19** (0.010 g) and NH_2-$(PEG)_{3400}$-NH-tBoc (0.294 g) were dissolved in 3.0 mL dry DMF. Then, dicyclohexylcarbodiimide (0.035 g, 172 mmol) and 4-dimethylaminopyridine (0.011 g, 86 mmol) were added to the reaction mixture under argon atmosphere. The reaction mixture was allowed to stir for 2 days at room temperature. The resulting suspension was then allowed to wait overnight with magnet, washed with distilled water for several times, and lyophilized to have Compound **20**.

Compound 21:

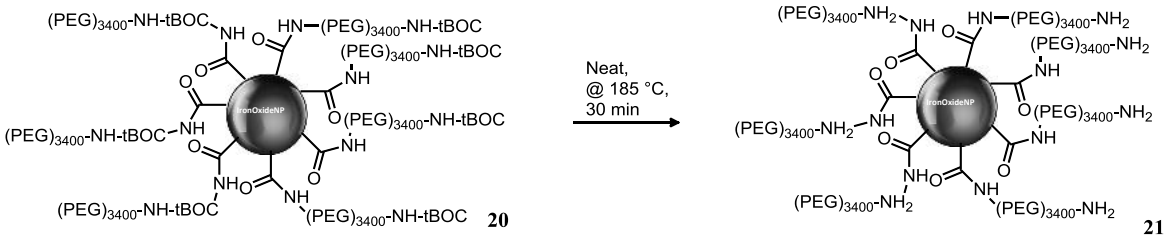

Figure 56. Synthesis of Compound 21.[102]

Compound **20** was heated neatly at the 185 °C for approximately 30 minutes to achieve the t-Boc deprotection and to have Compound **21**.

Compound 22:

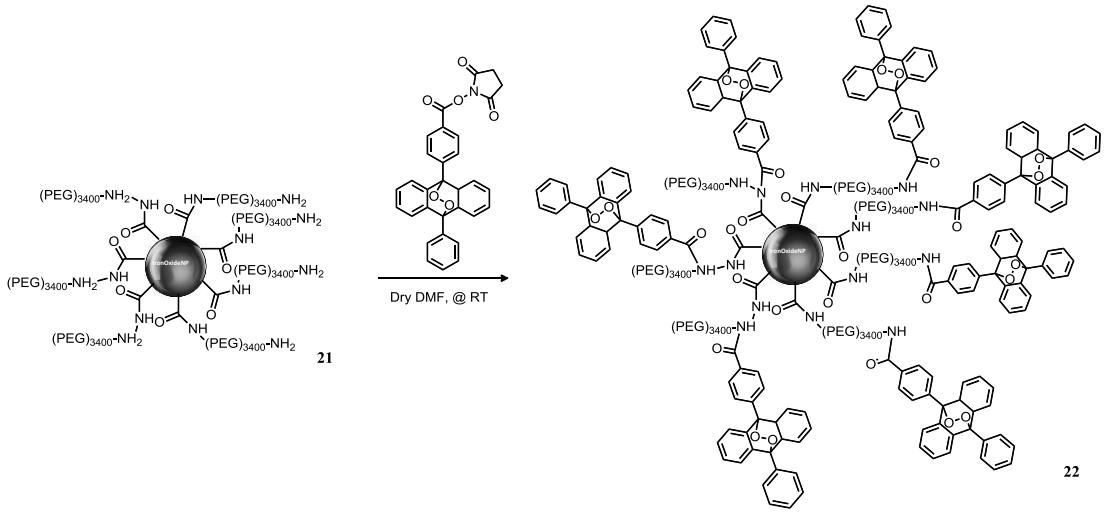

Figure 57. Synthesis of Compound 22.

Compound **21** (0.050 g) and Compound **18** (0.017 g, 0.006 mmol) were dissolved in 3.0 mL dry DMF under argon atmosphere. The reaction mixture was allowed to stir for 2 days at room temperature. The resulting suspension was then allowed to wait overnight with magnet, washed with distilled water for several times, and lyophilized to have Compound **22**.

Chapter 4

Naphthalene Endoperoxides for Chemically Triggered Singlet Oxygen Release

4.1. Objectives and Design

In this chapter, the kinetic study of 1,4-Dimethylnaphthalene endoperoxide derivative will be discussed. The objective of this work is to control the singlet oxygen generation rate by modifiying the metastable 1,4-Dimethylnaphthalene endoperoxide. Since the steric hindrance around the endoperoxide adduct could delay both formation and cycloreversion of the endoperoxide, we wanted to design a sterically hindered endoperoxide derivative. Due to its easy removal with the addition of fluoride, we decided to use trimethylsilyl group as steric hindrance source. Simple attachment and deprotection of TMS group could be attained in this structure design to proceed further toward practical goals. The synthesis scheme of the desired endoperoxide is given in the following Figure 58.

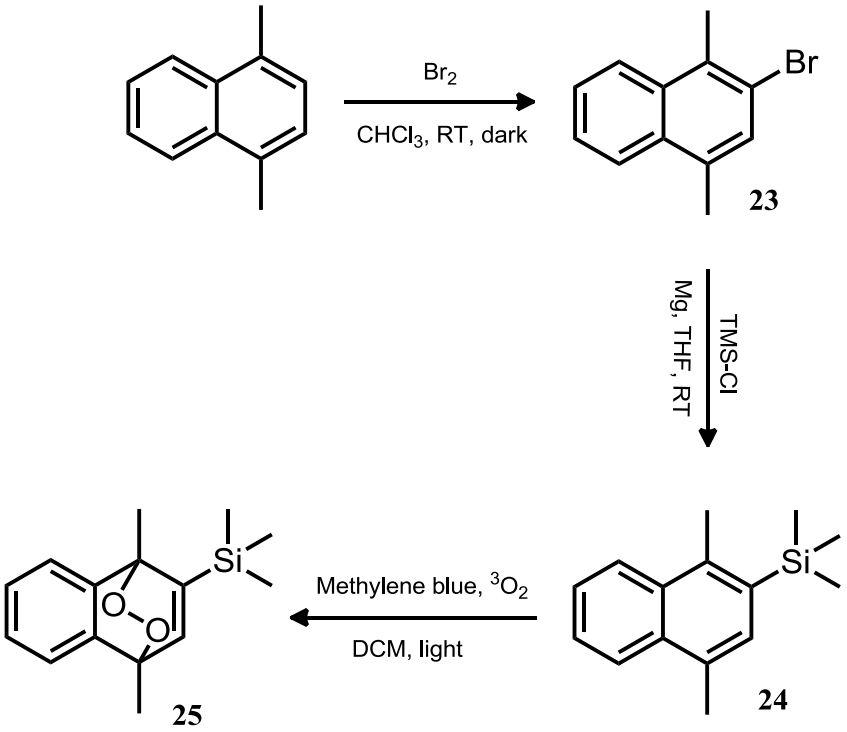

Figure 58. Synthetic pathway for 1,4-Dimethyl-2-TMS-naphthalene-endoperoxide.

4.2. Results and Discussion

With the intention of getting more qualitative results, the NMR investigations of two systems were performed as a function of time, the solvent being DMSO-d_6. It was observed that the TBAF introduced endoperoxide had a half-life of 4.7 hours, while the endoperoxide itself had a half-life of 790 hours according to appearance/disapearance of their normalized integral values of the selected peaks. The rate constant and half-life

calculations were done in accordance to the first-order reaction rate equations. The equations are given below:

$$\ln[A] = -kt + \ln[A]_0 \quad , \quad t_{1/2} = 0.693/k$$

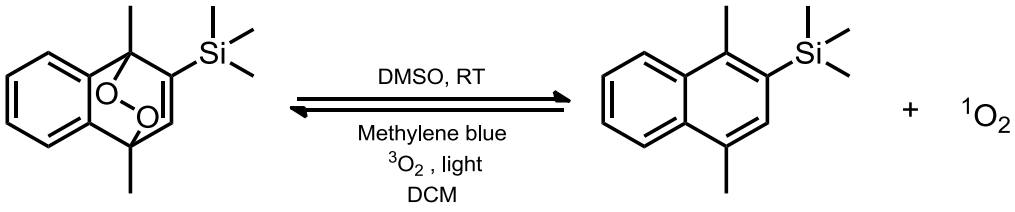

Figure 59. Reversible reaction of parent-naphthalene-endoperoxide.

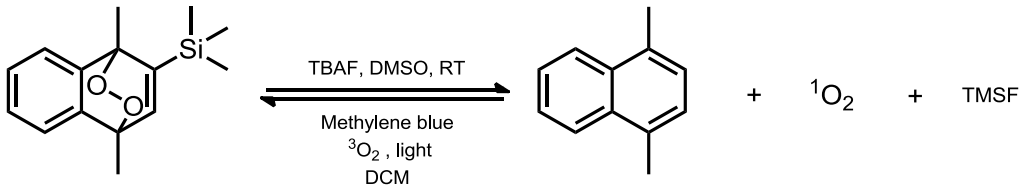

Figure 60. Reversible reaction of TBAF introduced-naphthalene-endoperoxide.

In the following NMR spectra, it is possible to observe the evolution of peaks (8.11-8.08, 8.01-7.98, 7.57, and 7.35 ppm) which belongs to Compound 24 due to endoperoxide cycloreversion. While the peaks of parent compound increases, the peaks of endoperoxide (7.38-7.34, 7.27-7.25, and 6.94 ppm) decreases.

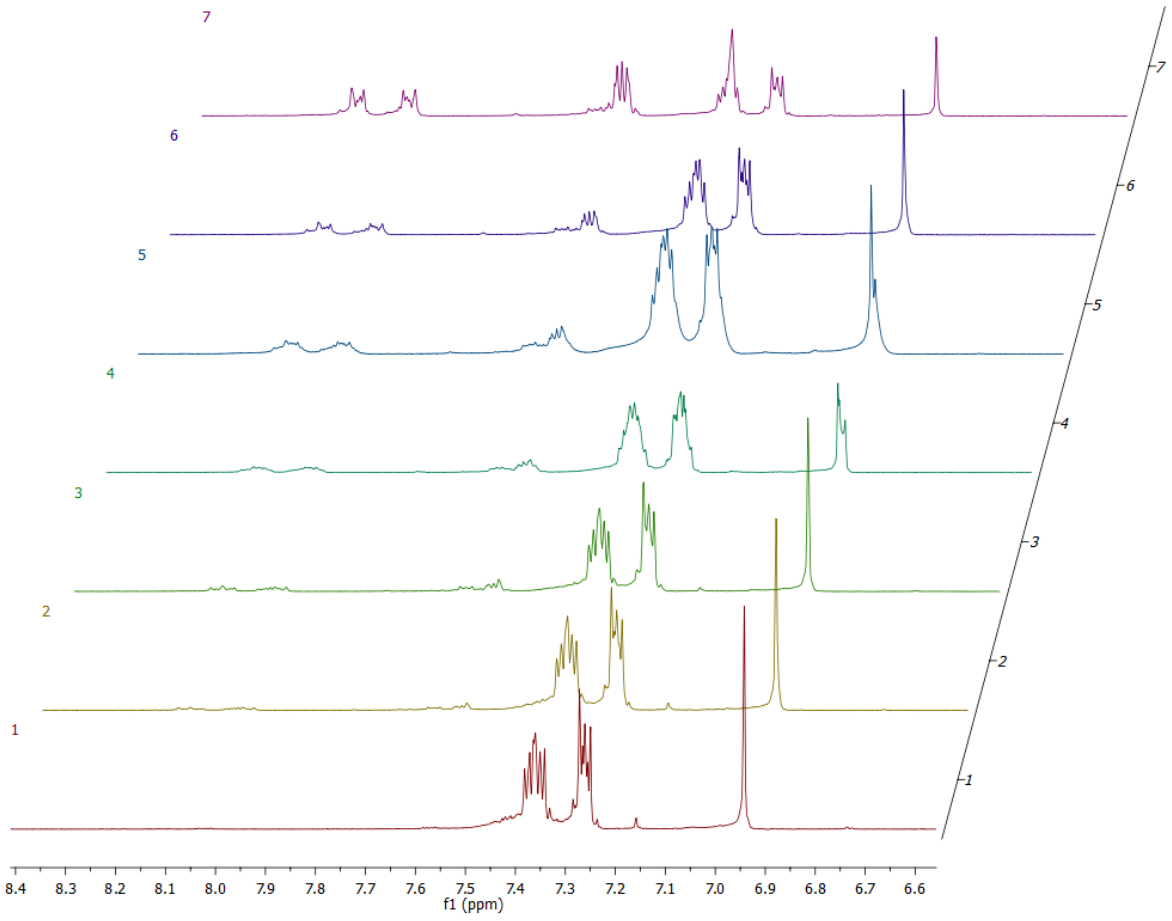

Figure 61. Evolution of the NMR spectra of parent-naphthalene- endoperoxide with time at room temperature in DMSO-d_6 as the solvent.

(Spectra 1- 0 hours, Spectra 2- 27.5 hours, Spectra 3- 67.5 hours, Spectra 4- 115.5 hours, Spectra 5- 153.5 hours, Spectra 6- 251 hours, Spectra 7- 990 hours).

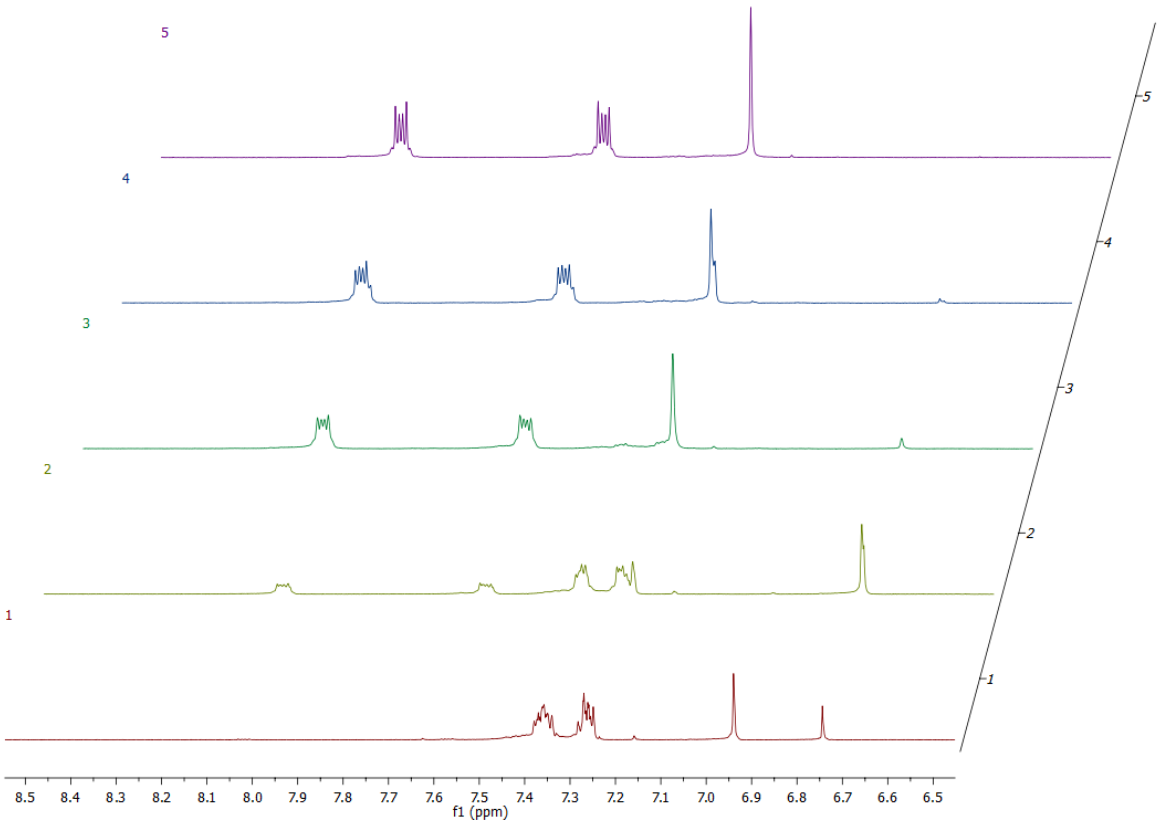

Figure 62. Evolution of the NMR spectra of TBAF introduced-naphthalene-endoperoxide with time at room temperature in DMSO-d_6 as the solvent.

(Spectra 1- 0 hours, Spectra 2- 3.5 hours, Spectra 3- 20 hours, Spectra 4- 27.5 hours, Spectra 5- 45.5 hours).

NMR spectra which is given above represents the evolution of peaks (8.03-8.0, 7.58-7.55, and 7.24 ppm) which belongs to 1,4-dimethyl naphthalene due to endoperoxide cycloreversion. After the addition of TBAF, when the peaks of parent naphthalene increases, the peaks of endoperoxide/Compound 25 (7.38-7.34, 7.27-7.25, and 6.94 ppm) decreases.

4.3. Conclusion

The kinetic investigation of TMS-endoperoxide and deprotected-TMS-endoperoxide is presently principle of proof study. However, the results which are presented earlier in the chapter are very promising. The observation of around 170-fold increase of cycloreversion rate when TMS deprotected with fluoride anions is a very good demonstration of how can one control/regulate the singlet oxygen release. As a conclusion, synthesis and in vitro experimentation for singlet oxygen release has been completed successfully. In vivo cell culture experimentation will be performed by our collaborators in China (Dalian University of Technology). Along wih this project, various other studies of controlling singlet oxygen generation rate is already in progress in our laboratories.

4.4. Experimental Details

4.3.1. Materials

All reagents and solvents were purchased from commercial suppliers and used without further purification. Reactions were monitored by thin layer chromatography using Merck TLC Silica gel 60 F_{254}. Column chromatography was performed by using Merck Silica Gel 60 (particle size: 0.040-0.063 mm, 230-400 mesh ASTM).

4.3.2. Instrumentation

The ^{1}H and ^{13}C NMR spectra were recorded using Bruker DPX-400 (operating at 400 MHz for ^{1}H NMR and 100 MHz for ^{13}C NMR) at 298 K using deuterated solvents with tetramethylsilane (TMS) as internal standard. Chemical shifts were reported in parts per million (ppm) and coupling constants (*J* values) are given in Hz. Splitting patterns are indicated as follow s, singlet; d, doublet; t, triplet; m, multiplet. Fluorescence Emission Spectra were performed by using Varian Cary Eclipse fluorescence spectrophotometer. Mass spectra were recorded with Agilent Technologies 6224 TOF LC/MS.

4.3.3. Synthesis

Compound 23:

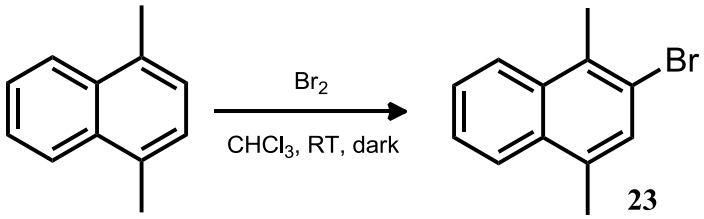

Figure 63. Synthesis of Compound 23.

1,4-Dimethyl naphtelene (1.56 g, 10.0 mmol) was dissolved in 15 mL chloroform under Argon atmosphere and exclusion of light. Bromine solution (0.54 mL, 10.5 mmol) was added to the reaction mixture over 10 minutes period of time at 0 °C, in an ice bath. Reaction was allowed to warm at room temperature for 2 hours while it was stirring.

Reaction was monitored by TLC. Then, the reaction mixture was diluted with 20 mL chloroform and washed with 25 mL saturated $Na_2S_2O_3$ solution, 25 mL water, and 25 mL saturated NaCl solution, accordingly. Organic layer was combined and dried over anhydrous Na_2SO_4. The solution was filtered through a thin pad of silica gel. After removal of the solvent by rotary evaporator, the crude product was purified by silica gel column chromatography with Hexane as the eluent. The product was obtained in colorless oil form with 93% yield (2.18 g, 9.3 mmol). ^{1}H NMR (400 MHz, $CDCl_3$): δ 8.08-8.06 (m, 1H), 8.00-7.98 (m, 1H), 7.57 (t, *J* = 4 Hz, 2H), 7.51 (s, 1H), 2.80 (s, 3H), 2.66 (s, 3H). ^{13}C NMR (100 MHz, $CDCl_3$): δ 133.94, 133.53, 131.77, 131.27, 130.5, 126.4, 125.5, 124.97, 124.81, 122.4, 18.97, 18.65.

Compound 24:

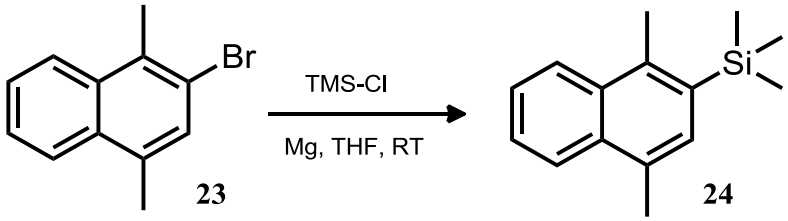

Figure 64. Synthesis of Compound 24.

First of all, Mg (0.15 g, 6.2 mmol) was activated with catalytic amount of iodine in 5 mL of THF for 15 minutes with vigorous stirring. Including the first step, all reaction conditions were carried out under $CaCl_2$ tube. Compound **23** (0.60 g, 2.6 mmol) was added to the reaction mixture in ice-bath. Followingly, TMSCl (0.33 g, 3.1 mmol) was

dissolved in 3 mL THF and was added to the reaction mixture dropwise. The reaction mixture was allowed to stir at room temperature for 24 hours. Then, the mixture was extracted with water and DCM for three times. After removal of the solvent by rotary evaporator, the crude product was purified by silica gel column chromatography with Hexane: EtOAc (95:5, v/v) as the eluent. The product was obtained in colorless oil form with 48% yield (0.29 g, 1.25 mmol). ^{1}H NMR (400 MHz, DMSO): δ 8.11-8.08 (m, 1H), 8.01-7.98 (m, 1H), 7.57 (t, *J* = 4 Hz, 2H), 7.35 (s, 1H), 2.74 (s, 3H), 2.61 (s, 3H), 0.38 (s, 9H). MS (TOF-ESI) m/z calcd for $C_{15}H_{20}Si$: 227.1262 $[M-H]^-$, found: 227.1234 $[M-H]^-$, Δ= 12.02 ppm. ^{13}C NMR (100 MHz, $CDCl_3$): δ 138.8, 133.0, 132.5, 131.4, 130.9, 126.47, 126.06, 124.91, 124.84, 19.65, 19.58, 0.9.

Compound 25:

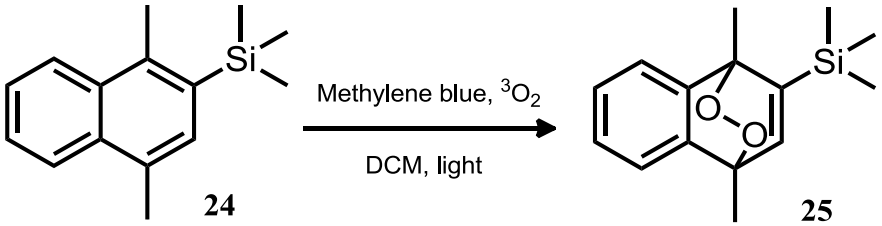

Figure 65. Synthesis of Compound 25.

Compound **24** (0.15 g, 0.66 mmol) was dissolved in 20 mL DCM. The reaction mixture was cooled to – 78 °C. Methylene blue (0.02 g, 0.07 mmol) was added into the solution and mixture was stirred for 10 hours under oxygen atmosphere. During the reaction water-cooled 400 W Hg arc lamp (white light irradiation) was used. After removal of the

solvent by rotary evaporator, the crude product was purified by silica gel column chromatography with Hexane: EtOAc (95:5, v/v) as the eluent. The product was obtained in colorless oil form with 51% yield (0.09 g, 0.34 mmol). ^{1}H NMR (400 MHz, DMSO): δ 7.38-7.34 (m, 2H), 7.27-7.25 (m, 2H), 6.94 (s, 1H), 1.86 (s, 3H), 1.77 (s, 3H), 0.15 (s, 9H). MS (TOF-ESI) m/z calcd for $C_{15}H_{20}O_2Si$: 261.1305 $[M+H]^+$, found: 261.1296 $[M+H]^+$, Δ= 3.46 ppm.

Bibliography

[1] J. W. Steed and J. L. Atwood, *Supramolecular Chemistry*. John Wiley & Sons: West Sussex, 2009.

[2] J.M. Lehn, "Supramolecular Chemistry: Where from? Where to?," *Chem. Soc. Rev.*, vol. 46, pp. 2378-2379, 2017.

[3] D. B. Amabilino, D. K. Smith, and J.W. Steed, "Supramolecular Materials," *Chem. Soc. Rev.*, vol. 46, pp. 2404-2420, 2017.

[4] F. Huang and E. V. Anslyn, "Introduction: Supramolecular Chemistry," *Chem. Rev.*, vol. 115, no. 15, pp. 6999-7000, 2015.

[5] J. W. Steed, D. R. Turner, and K. J. Wallace, *Core Concepts in Supramolecular Chemistry and Nanochemistry.* John Wiley & Sons: West Sussex, 2007.

[6] H. J. Schneider and A. K. Yatsimirsky, "Selectivity in Supramolecular Host-Guest Complexes," *Chem. Soc. Rev.*, vol. 37, pp. 263-277, 2008.

[7] H. Yang, B. Yuan and X. Zhang, "Supramolecular Chemistry at Interfaces: Host-Guest Interactions for Fabricating Multifunctional Biointerfaces," *Acc. Chem. Res.*, vol. 47, no.7, pp. 2106-215, 2014.

[8] G. M. Whitesides and M. Boncheva, "Beyond Molecules: Self-Assembly of Mesoscopic and Macroscopic Components," *PNAS*, vol. 99, no. 8, pp. 4769-4774, 2002.

[9] A. Harada, *Supramolecular Polymer Chemistry.* WILEY-VCH Verlag GmbH & Co. KGaA, 2012.

[10] S. I. Stupp and L. C. Palmer, "Supramolecular Chemistry and Self-Assembly in Organic Materials Design," *Chem. Mater.*, vol.26, no.1, pp. 507-518, 2014.

[11] H. J. Schneider, T. Schiestel and P. Zimmermann, "The Incremental Approach to Noncovalent Interactions: Coulomb and van der Walls Effects in Organic Ion Pairs," *J. Am. Chem. Soc.*, vol. 114, pp. 7698-7703, 1992.

[12] L. G. Suarez, W. Verboom, R. J. M. Egberink, S. Sarkar, V. Mahalingam and J. Huskens, "Host-Guest and Electrostatic Interactions in Supramolecular Nanoparticle Clusters," *Eur. J. Org. Chem.*, pp. 5511-5518, 2016.

[13] M. Saccone, V. Dichiarante, A. Forni, A. G. Hanssens, G. Cavallo, J. Vapaavuori, G. Terraneo, C. J. Barrett, G. Resnati, P. Metrangolo and A. Priimagi, "Supramolecular Hierarchy Among Halogen and Hydrogen Bond Donors in Light-Induced Surface Patterning," *J. Mater. Chem. C.*, vol. 3, pp. 759-768, 2015.

[14] G. R. Desiraju and T. Steiner, *The Weak Hydrogen Bond: Instructural Chemistry and Biology.* Oxford University Press, 2001.

[15] J. L. Atwood, G. W. Gokel and L. J. Barbour, *Comprehensive Supramolecular Chemistry II.* ELSEVIER, 2017.

[16] J. Teyssandier, S. D. Feyter and K. S. Mali, "Host-Guest Chemistry in Two-Dimensional Supramolecular Networks," *Chem. Commun.*, vol. 52, pp. 11465-11487, 2016.

[17] J. Hermann, D. Alfe and A. Tkatchenko, "Nanoscale π-π Stacked Molecules are Bound by Collective Charge Fluctuations," *Nature Communications*, vol.8, 14052, 2017.

[18] A. S. Mahadevi and G. N. Sastry, "Cation-π Interaction: Its Role and Relevance in Chemistry, Biology and Materials Science," *Chem. Rev.*, vol. 113, no. 3, pp. 2100-2038, 2013.

[19] F. Biedermann, W. M. Nau and H. J. Schneider, "The Hydrophobic Effect Revisited-Studies with Supramolecular Complexes Imply High-Energy Water as a Noncovalent Driving Force," *Angew. Chem. Int. Ed.*, vol. 53, pp. 11158-11171, 2014.

[20] M. B. Hillyer and B. C. Gibb, "Molecular Shape and the Hydrophobic Effect," *Annu. Rev. Phys. Chem.*, vol. 67, pp. 307-329, 2016.

[21] B. Valeur, *Molecular Fluorescence: Principles and Application*. Wiley VCH-Weinheim, 2005.

[22] J. R. Lakowicz, *Priciples of Fluorescence Spectroscopy*. Springer: New York, 2006.

[23] A. P. Castell, E. Tyystjarvi, J. Atherton, C. van der Tol, J. Flexas, E. E. Pfündel, J. Moreno, C. Frankenberg and J. A. Berry, "Linking Chlorophyll a Fluorescence to Photosynthesis for Remote Sensing Applications: Mechanisms and Challenges," *Journal of Experimental Botany*, vol. 65, no. 15, pp. 4065-4095, 2014.

[24] J. H. Easter, R. P. Detoma and L. Brand, "Nanosecond Time-Resolved Emission Spectroscopy of a Fluorescence Probe Adsorbed to L-α-EGG Lecithin Vesicles," *Biophysical Journal*, vol. 16, pp. 571-583, 1976.

[25] M. Ethirajan, Y. Chen, P. Joshi and R. K. Pandey, "The Role of Porphyrin Chemistry in Tumor Imaging and Photodynamic Therapy," *Chem. Soc. Rev.*, vol. 40, pp. 340-362, 2011.

[26] Y. C. Duan, L. L. Wen, Y. Gao, Y. Wu, L. Zhao, Y. Geng, G. G. Shan, M. Zhang and Z. M. Su, "Fluorescence, Phosphorescence, or Delayed Fluorescence?- A Theoretical Exploration on the Reason Why a Series of Similar Organic Molecules Exhibit Different Luminescence Types," *J. Phys. Chem. C*, vol. 122, no. 40, pp. 23091-23101, 2018.

[27] G. A. Crosby and J. N. Demas, "Measurement of Photoluminescence Quantum yields. A Review," *J. Phys. Chem.*, vol. 75, no. 8, pp. 991-1024, 1971.

[28] P. Agostinis, K. Berg, K. A. Cengel, T. H. Foster, A. W. Girotti, S. O. Gollnick, S. M. Hahn, M. R. Hamblin, A. Juzeniene, D. Kessel, M. Korbelik, J. Moan, P. Mroz, D. Nowis, J. Piette, B. C. Wilson and J. Golab, "Photodynamic Therapy of Cancer: An Update," *CA Cancer J Clin.*, vol. 61, no. 4, pp. 250-281, 2011.

[29] M. Triesscheijn, P. Baas, J. H. Schellens and F. A. Stewart, " Photodynamic Therapy in Oncology," *Oncologist*, vol. 11, no.9, pp. 1034-1044, 2006.

[30] A. P. Castano, T. N. Demidova and M. R. Hamblin, "Mechanisms in Photodynamic Therapy: Part-One Photosensitizers, Photochemistry and Cellular Localization," *Photodiagnosis Photodyn. Ther.*, vol. 1, no. 4, pp. 279-293, 2004.

[31] K. Szacilowski, W. Macyk, A. Drzewiecka-Matuszek, M. Brindell and G. Stochel, "Bioinorganic Photochemistry: Frontiers and Mechanisms," *Chem. Rev.*, vol. 105, no. 6, pp. 2647-2694, 2005.

[32] K. J. A. Davies, "Protein Damage and Degradation by Oxygen Radicals," *J. Biol. Chem.*, vol. 262, no. 20, pp. 9895-9901, 1987.

[33] D. E. Dolmans, D. Fukumura and R. K. Jain, "Photodynamic Therapy for Cancer," *Nat. Rev. Cancer*, vol. 3, no. 5, pp. 380-387, 2003.

[34] M. D. Daniell and J. S. Hill, " A History of Photodynamic Therapy," *Aust. N Z J Surg.*, vol. 61, no.5, pp. 340-348, 1991.

[35] M. H. Abdel-Kader, *Photodynamic Therapy: From Theory to Application.* Springer-Verlag Berlin Heidelberg, 2014.

[36] R. Ackroyd, C. Kelty, N. Brown and M. Reed, "The History of Photodetection and Photodynamic Therapy," *Photochemistry and Photobiology*, vol. 74, no. 5, pp. 656-669, 2001.

[37] I. Yoon, J. Z. Li and Y. K. Shim, "Advance in Photosensitizers and Light Delivery for Photodynamic Therapy," *Clin. Endosc.*, vol. 46, no. 1, pp. 7-23, 2013.

[38] L. B. Josefsen and R. W. Boyle, "Photodynamic Therapy and the Development of Metal-Based Photosensitizers," *Met. Based Drugs*, vol. 2008, Article ID 276109, 23 pages, 2008.

[39] R. Bonnett and G. Martinez, "Photobleaching of Sensitizers Used in Photodynamic Therapy," *Tetrahedron*, vol. 57, no. 47, pp. 9513-9547, 2001.

[40] I. J. MacDonald and T. J. Dougherty, "Basic Principles of Photodynamic Therapy," *Journal of Porphyrins and Phthalocyanines*, vol. 5, no.2, pp. 105-129, 2001.

[41] N. S. Konstantin and E. A. Borisevich, "Intramolecular Heavy-Atom Effect in the Photophysics of Organic Molecules," *Physics-Uspekhi*, vol. 48, no.3, pp. 231, 2005.

[42] Y. Liu, M. Lin and Y. Zhao, "Intersystem Crossing Rates of Isolated Fullerenes: Theoretical Calculations," *J. Phys. Chem. A*, vol. 121, no. 5, pp. 1145-1152, 2017.

[43] J. O. Yoo and K. S. Ha, "Ch. 4: New Insights Into the Mechanisms for Photodynamic Therapy-Induced Cancer Cell Death," *International Review of Cell and Molecular Biology*, vol. 295, pp. 139-174, 2012.

[44] H. Abrahamse and M. R. Hamblin, "New Photosensitizers for Photodynamic Therapy," *Biochem J.*, vol. 473, no. 4, pp. 347-364, 2016.

[45] D. M. McDonald and P. Baluk, “Significance of Blood Vessel Leakiness in Cancer,” *Cancer Res.*, vol. 62, no.18, pp. 5381-5385, 2002.

[46] R. Ngoune, A. Peters, D. Von Elverfeldt, K. Winkler and G. Pütz, “Accumulating nanoparticles by EPR: A Route of No Return,” *Journal of Controlled Release*, vol. 238, pp. 58-70, 2016.

[47] C. Ash, M. Dubec, K. Donne and T. Bashford, “Effect of Wavelength and Beam Width on Penetratioon in Ligth-Tissue Interaction Using Computational Methods,” *Lasers Med. Sci.*, vol. 32, no. 8, pp. 1909-1918, 2017.

[48] T. C. Zhu and J. C. Finlay, “ The Role of Photodynamic Therapy (PDT) Physics,” *Med. Phys.*, vol. 35, no. 7, pp. 3127-3136, 2008.

[49] G. H. Beaven and E. R. Holiday, “Ultraviolet Absorption Spectra of Proteins and Amino Acids,” *Advances in Protein Chemistry*, vol. 7, pp. 319-386, 1952.

[50] T. L. Troy and S. N. Thennadil, “Optical Properties of Human Skin in the Near Infrared Wavelength Range of 1000 to 2000 nm,” *J. Biomed. Opt.*, vol. 6, no. 2, pp. 167-176, 2001.

[51] X. S. Li, S. Kolemen, J. Yoon and E. U. Akkaya, “Activatable Photosensitizers: Agents for Selective Photodynamic Therapy,” *Adv. Func. Mater.*, vol. 27, no. 5, pp. 1604053, 2017.

[52] J. Dang, H. He, D. Chen and L. Yin, “Manipulating Tumor Hypoxia Toward Enhanced Photodynamic Therapy,” *Biomater. Sci.*, vol. 5, no. 8, pp. 1500-1511, 2017.

[53] S. Ozlem, and E. U. Akkaya, “ Thinking Outside the Silicon Box: Molecular and Logic as an Additional Layer of Selectivity in Singlet Oxygen Generation for Photodynamic Therapy,” *J. Am. Chem. Soc.*, vol. 131, no.1, pp. 48-49, 2009.

[54] Y. Ichikawa, M. Kamiya, F. Obata, M. Miura, T. Terai, T. Kumatsu, T. Ueno, K. Hanaoka, T. Nagano and Y. Urano, "Selective Ablation of β-Galactosidase-Expressing Cells with a Rationally Designed Activatable Photosensitizer," *Angew. Chem. Int. Ed.*, vol. 53, no. 26, pp. 6772-6775, 2014.

[55] S. Erbas-Cakmak and E. U. Akkaya, " Cascading of Molecular Logic Gates for Advanced Functions: A Self-Reporting, Activatable Photosensitizer," *Angew. Chem. Int. Ed.*, vol. 52, pp. 11364-11368, 2013.

[56] X. Li, C. Y. Kim, S. Lee, D. Lee, H.-M. Chung, G. Kim, S. H. Heo, C. Kim, K. S. Hong and J. Yoon, "Nanostructured Phthalocyanine Assemblies with Protein-Driven Switchable Photoactivities for Biophotonic Imaging and Therapy," *J. Am. Chem. Soc.*, vol. 139, no. 31, pp. 10880–10886, 2017.

[57] I. S. Turan, F. P. Cakmak, D. C. Yildirim, R. Cetin-Altay and E. U. Akkaya, "Near-IR Absorbing BODIPY Derivatives as Glutathione-Activated Photosensitizers for Selective Photodynamic Action," *Chem. Eur. J.*, vol. 20, no. 49, pp. 16088-16092, 2014.

[58] X. J. Jiang, J. T. F. Lau, Q. Wang, D. K. P. Ng and P.- C. Lo, "pH and Thiol-Responsive BODIPY-Based Photosensitizers for Targeted Photodynamic Therapy," *Chem. Eur. J.*, vol. 22, no. 24, pp. 8273-8281, 2016.

[59] B. B. Zhang, D. G. Wang, F. F. Guo and C. Xuan, "Mitochondrial Membrane Potential and Reactive Oxygen Species in Cancer Stem Cells," *Familial Cancer*, vol.14, no.1, pp. 19-23, 2015.

[60] C. A. Robertson, D. H. Evans and H. Abrahamse, "Photodynamic Therapy (PDT): A Short Review on Cellular Mechanisms and Cancer Research Applications for PDT," *J. Photochem. Photobiol. B*, vol. 96, no. 1, pp. 1-8, 2009.

[61] M. A. Houston, L. H. Augenlicht and B. G. Heerdt, "Stable Differences in Intrinsic Mitochondrial Membrane Potential of a Tumor Cell Subpopulations Reflect Phenotypic Heterogeneity," *Int. J. Cell Biol*., vol. 2011, pp. 978583, 2011.

[62] V. R. Fantin, J. St-Pierre and P. Leder, "Attenuation of LDH-A Expression Uncovers a Link between Glycolysis, Mitochondrial Physiology, and Tumor Maintenance," *Cancer Cell*, vol. 9, no. 6, pp. 425-434, 2006.

[63] S. Mori, J. T. Chang, E. R. Andrachek, N. Matsumura, T. Baba, G. Yao, J. W. Kim, M. Gatza, S. Murphy and J. R. Nevins, "Anchorage-Independent Cell Growth Signature Identifies Tumors with Metastatic Potential," *Oncogene*, vol. 28, no. 31, pp. 2796-2805, 2009.

[64] S. Ito, T. Murashima, N. Ono and H. Uno, "A New Synthesis of Benzoporphyrins Using 4,7-Dihydro-4,7-ethano-2H-isoindole as a Synthon of Isoindole," *Chem. Commun.*, vol. 0, pp. 1661-1662, 1998.

[65] M. C. Frantz and P. Wipf, "Mitochondria as a Target in Treatment," *Environ Mol Mutagen*., vol. 51, no.5, pp. 462-475, 2010.

[66] A. Treibs and F. H. Kreuzer, "Difluorboryl-Komplexe von Di- und Tripyrrylmethenen*," Liebigs Ann. Chem*., vol. 718, pp. 208-223, 1968.

[67] I. D. Johnson, H. C. Kang and R. P. Haugland, "Fluorescent Membrane Probes Incorporating Dipyrrometheneboron Difluoride Fluorophores," *Anal. Biochem.*, vol. 198, pp. 228-237, 1991.

[68] I. A. Boldyrev, X. Zhai, M. M. Momsen, H. L. Brockman, R. E. Brown and J. G. Molotkovsky, "New BODIPY Lipid Probes for Fluorescence Studies of Membranes," *J. Lipid Res.*, vol. 48, no. 7, pp. 1518-1532, 2007.

[69] A. Loudet and K. Burgess, "BODIPY Dyes and Their Derivatives: Synthesis and Spectroscopic Properties," *Chem. Rev*., vol. 107, no. 11, pp. 4891-4932, 2007.

[70] X. Zhang, Y. Xiao, J. Qi, B. Kim, X. Yue and K. D. Belfield, "Long-Wavelength, Photostable, Two-Photon Excitable BODIPY Fluorophores Readily Modifiable for Molecular Probes," *J. Org. Chem.*, vol.78, no. 18, pp. 9153-9160, 2013.,

[71] T. A. Golovkova, D. V. Kozlov and D. C. Neckers, "Synthesis and Properties of Novel Fluorescent Switches," *J. Org. Chem.*, vol. 70, no. 14, pp. 5545-5549, 2005.

[72] A. Kamkaew, S. H. Lim, H. B. Lee, L. V. Kiew, L. Y. Chung and K. Burgess, "BODIPY Dyes in Photodynamic Therapy," *Chem. Soc. Rev.*, vol. 42, pp. 77-78, 2013.

[73] S. Ertan-Ela, M. D. Yılmaz, B. Icli, Y. Dede, S. Icli and E. U. Akkaya, " A Panchromatic Boradiazaindacene (BODIPY) Sensitizer for Dye-Sensitized Solar Cells," *Org. Lett.*, vol. 10, pp. 3299-3302, 2008.

[74] Z. Kostereli, T. Ozdemir, O. Buyukcakir and E. U. Akkaya, "Tetrastyryl-BODIPY-Based Dendritic Light Harvester and Estimation of Energy Transfer Efficiency," *Org. Lett.*, vol. 14, pp. 3636-3639, 2012.

[75] V. Lakshmi, M. R. Rao and M. Ravikanth, "Halogenated Boron-Dipyrromethenes: Synthesis, Properties and Applications," *Org. Biomol. Chem.*, vol. 13, pp. 2501-2517, 2015.

[76] S. Fulda, L. Galluzzi and G. Kroemer, "Targeting Mitochondria for Cancer Therapy," *Nature Reviews Drug Discovery*, vol. 9, pp. 447-464, 2010.

[77] B. M. Trost and I. Fleming, *Comprehensive Organic Synthesis*, Pergamon Press: Oxford, 1991.

[78] L. F. Tietze, “Domino Reactions in Organic Synthesis,” *Chem. Rev.*, vol. 96, no. 1, pp. 115-136, 1996.

[79] E. Deniz, G. C. Isbasar, Ö. A. Bozdemir, L. T. Yildirim, A. Siemiarczuk and E. U. Akkaya, “Bidirectional Switching of Near IR Emitting Boradiazaindacene Fluorophores,” *Org. Lett.*, vol. 10, no. 16, pp. 3401-3403, 2008.

[80] S. Y. Kim and J. W. Park, “Cellular Defense Against Singlet Oxygen-Induced Oxidative Damage by Cytosolic NADP+- Dependent Isocitrate Dehydrogenase,” *Free Radic. Res.*, vol. 37, no. 3, pp. 309-316, 2003.

[81] C. Triantaphylides, M. Krischke, F. A. Hoeberichts, B. Ksas, G. Gresser, M. Havaux, F. V. Breusegem and M. J. Mueller, “Singlet Oxygen is the Major Reactive Oxygen Species Involved in Photooxidative Damage to Plants,” *Plant Physiol.*, vol. 148, no. 2, pp. 960-968, 2008.

[82] M. Bregnhoj, M. Westberg, F. Jensen and P. R. Ogilby, “Solvent-Dependent Singlet Oxygen Lifetimes: Temperature Effects Implicate Tunneling and Charge-Transfer Interactions,” *Phys. Chem. Chem. Phys.*, vol. 18, pp. 22946-22961, 2016.

[83] L. Ozog and D. Aebisher, “Singlet Oxygen Lifetime and Diffusion Measurements,” *Eur. J. Clin. Exp. Med.*, vol. 16, no. 2, pp. 123-126, 2018.

[84] M. S. Baptista, J. Cadet, P. Di Mascio, A. A. Ghogare, A. Greer, M. R. Hamblin, C. Lorente, S. C. Nunez, M. S. Ribeiro, A. H. Thomas, M. Vignoni and T. M. Yoshimura, “Type I and Type II Photosensitized Oxidation Reactions: Guidelines and Mechanistic Pathways,” *Photochem. Photobiol.*, vol. 93, no.4, pp. 912-919, 2017.

[85] A. C. Moor, “Signaling Pathways in Cell Death and Survival After Photodynamic Therapy,” *J. Photochem. Photobiol. B.*, vol. 57, no.1, pp. 1-13, 2000.

[86] P. Mroz, A. Yaroslavskyi, G. B. Kharkwal and M. R. Hamblin, "Cell Death Pathways in Photodynamic Therapy of Cancer," *Cancers(Basel)*, vol. 3, no. 2, pp. 2516-2539, 2011.

[87] W. Lv, Z. Zhang, K. Y. Zhang, H. Yang, S. Liu, A. Xu, S. Guo, Q. Zhao and W. Huang, "A Mitochondria-Targeted Photosensitizer Showing Improved Photodynamic Therapy Effects Under Hypoxia," *Angew. Chem. Int. Ed.*, vol. 55, pp. 9947-9951, 2016.

[88] L. Tan, J. Li, X. Liu, Z. Cui, X. Yang, K. W. K. Yeung, H. Pan, Y. Zheng, X. Wang and S. Wu, "In Situ Disinfection through Photoinspired Radical Oxygen Species Storage and Thermal-Triggered Release from Black Phosphorous with Strengthened Chemical Stability," *Small.*, vol. 14, no. 9, 2018.

[89] M. A. Filatov and M. O. Senge, "Molecular Devices Based on Reversible Singlet Oxygen Binding in Optical and Photochemical Applications," *Mol. Syst. Des. Eng.*, vol. 1, pp. 258-272, 2016.

[90] S. Uttiya, L. Miozzo, E. M. Fumagalli, S. Bergantin, R. Ruffo, M. Parravicini, A. Papagni, M. Moret and A. Sassella, "Connecting Molecule Oxidation to Singlet Crystal Structural and Charge Transport Properties in Rubrene Derivatives," *J. Mater. Chem. C.*, vol. 2, pp. 4147-4155, 2014.

[91] H. H. Wasserman, J. R. Scheffer and J. L. Cooper, "Singlet Oxygen Reactions with 9,10-Diphenylanthracene Peroxide," *J. Am. Chem. Soc.*, vol. 94, no. 14, pp. 4991-4996, 1972.

[92] C. W. Jefford and A. F. Boschung, "The Reaction of Biadamantylidene with Singlet Oxygen in the Presence of Dyes," *Helvetica*, vol. 60, no. 8, pp. 2673-2685, 1977.

[93] S. Miyamoto, G. R. Martinez, M. H. Medeiros and P. Di Mascio, " Singlet Oxygen Generated by Biological Hydroperoxides," *J. Photochem. Photobiol. B.*, vol. 139, pp. 24-33, 2014.

[94] D. Lopez, E. Quinoa and R. Riguera, " The [4+2] Addition of Singlet Oxygen to Thebaine: New Access to Highly Functionalized Morphine Derivatives via Opioid Endoperoxides," *J. Org. Chem.*, vol. 65, no. 15, pp. 4671-4678, 2000.

[95] M. C. DeRosa and R. J. Crutchley, " Photosensitized Singlet Oxygen and Its Applications," *Coordination Chem. Rev.*, vol. 233-234, pp. 351-371, 2002.

[96] E. L. Clennan, X. Chen and J. J. Koola, "Steric and Electronic Effects on the Conformations and Singlet Oxygen Ene Regiochemistries of Substituted Tetramethylethylenes. The Origin of Geminal Effect," *J. Am. Chem. Soc.*, vol. 112, no. 13, pp. 5193-5199, 1990.

[97] A. R. Reddy and M. Bendikov, " Diels-Alder Reaction of Acenes with Singlet and Triplet Oxygen- Theoretical Study of Two-State Reactivity," *Chem. Comm.*, vol. 0, pp. 1179-1181, 2006.

[98] E. L. Clennan and M. E. Mehrsheikh-Mohammadi, "Mechanism of Endoperoxide Formation. 3. Utilization of the Young and Carlsson Kinetic Techniques," *J. Am. Chem. Soc.*, vol. 106, no. 23, pp. 7112-7118, 1984.

[99] E. L. Clennan and M. E. Mehrsheikh-Mohammadi, "Addition of Singlet Oxygen to Conjugated Dienes. The Mechanism of Endoperoxide Formation," *J. Am. Chem. Soc.*, vol. 105, no. 18, pp. 5932-5933, 1983.

[100] R. Schmidt, W. Drews and H. D. Brauer, "Photolysis of the Endoperoxide of Heterocoerdianthrone. A Concerted, Adiabatic Cycloreversion Originating From an Upper Excited Singlet State," *J. Am. Chem. Soc.*, vol. 102, no. 8, pp. 2791-2797, 1980.

[101] G. Sartori, R. Ballini, F. Bigi, G. Bosica, R. Maggi and P. Righi, "Protection (and Deprotection) of Functional Groups in Organic Synthesis by Heterogenous Catalysis," *Chem. Rev.*, vol. 104, no. 1, pp. 199-250, 2004.

[102] P. G. M. Wuts and T. W. Greene, *Greene's Protective Groups in Organic Synthesis*. Wiley-Interscience, 2006.

[103] M. Bols and C. M. Pedersen, "Silyl-Protective Groups Influencing the Reactivity and Selectivity in Glycosylations," *Beilstein J. Org. Chem.*, vol. 13, pp. 93-15, 2017.

[104] U. Ragnarsson and L. Grehn, "Dual Protection of Amino Functions Involving Boc," *RSC Adv.*, vol. 3, pp. 18691-18697, 2013.

[105] Y. Kaburagi and Y. Kishi, "An Operationally Simple and Efficient Work-up Procedure for TBAF-Mediated Desilylation; Application to Halichondrin Synthesis," *Org. Lett.*, vol. 9, no. 4, pp. 723-726, 2007.

[106] H. Yan, J. S. Oh and C. E. Song, "A Mild and Efficient Method for the Selective Deprotection of Silyl Ethers Using KF in the Presence of Tetraethylene Glycol," *Org. Biomol. Chem.*, vol. 9, pp. 8119-8121, 2011.

[107] G. Günther, E. Lemp and A. L. Zanocco, "Determination of Chemical Rate Constants in Singlet Molecular Oxygen Reactions by Using 1,4-Dimethylnaphthalene Endoperoxide," *J. Photochem. Photobiol. A.*, vol. 151, pp. 1-5, 2002.

[108] B. K. Ohta and C. S. Foote, "Characterization of Endoperoxide and Hydroperoxide in the Reaction of Pyridoxine with Singlet Oxygen," *J. Am. Chem. Soc.*, vol. 124, no. 41, pp. 12064-12065, 2002.

[109] M. R. Wixom, "Time-Dependent Reaction Rates in the Thermolysis of a Poly (vinylnaphthalene endoperoxide)," *J. Phys. Chem.*, vol. 94, no. 12, pp. 4926-4929, 1977.

[110] N. Nishide and N. Miyoshi, "Singlet Oxygen Trapping by DRD156 in Micellar Solutions," *Life Sci.*, vol. 72, no. 3, pp. 321-328, 2002.

[111] S. Kim, M. Fujitsuka and T. Majima, "Photochemistry of Singlet Oxygen Sensor Green," *J. Phys. Chem. B.*, vol. 117, no. 45, pp. 13985-13992, 2013.

[112] W. Adam, D. V. Kazakov and V. P. Kazakov, "Singlet-Oxygen Chemiluminescence in Peroxide Reactions," *Chem. Rev.*, vol. 105, pp. 3371-3387, 2005.

[113] H. H. Wasserman, K. B. Wiberg, D. L. Larsen and J. Parr, "Photooxidation of Methylnaphthalenes," *J. Org. Chem.*, vol. 70, no.1, pp. 105-109, 2005.

[114] D. Posavec, M. Zabel, G. Bernhardt and G. Knör, "Functionalized Derivatives of 1,4-Dimethylnaphthalene as Precursors for Biomedical Applications: Synthesis, Structures, Spectroscopy and Photochemical Activation in the Presence of Dioxygen," *Org. Biomol. Chem.*, vol. 10, pp. 7062-7069, 2012.

[115] A. Chichel, J. Skowronek, M. Kubaszewska and M. Kanikowski, "Hyperthermia-Description of a Method and A Review of Clinical Applications," *Reports of Practical Oncology & Radiotherapy*, vol. 12, no. 5, pp. 267-275, 2007.

[116] W. Rao, Z. S. Deng and J. Liu, "A Rewiev of Hyperthermia Combined with Radiotherapy/Chemotherapy on Malignant Tumors," *Crit. Rev. Biomed. Eng.*, vol. 38, no. 1, pp. 101-116, 2010.

[117] S. Jha, P. K. Sharma and R. Malviya, "Hyperthermia: Role and Risk Factors for Cancer Treatment," *Achievements in the Life Sciences*, vol. 10, no. 2, pp. 161-167, 2016.

[118] A. Jordan, P. Wust, H. Fähling, W. John, A. Hinz, and R. Felix, "Inductive Heating of Ferrimagnetic Particles and Magnetic Fluids: Physical Evaluation of Their Potential for Hyperthermia," *International Journal of Hyperthermia*, vol. 9, no. 1, pp. 51–68, 1993.

[119] A. Sohail, Z. Ahmad, O. A. Beg, S. Arshad and L. Sherin, "A Review on Hyperthermia via Nanoparticle-Mediated Therapy," *Bull Cancer*, vol. 104, no. 5, pp. 452-461, 2017.

[120] L. Bubnovskaya, A. Belous, S.Solopan, A. Kovelskaya, L. Bovkun, A. Podoltsev, I. Kondtratenko and S. Osinsky, "Magnetic Fluid Hypertermia of Rodent Tumors Using Manganese Perovskite Nanoparticles," *Journal of Nanoparticles*, vol. 2014, Article ID 278761, 9 pages, 2014.

[121] V. Herynek, K. Turnovcova, P. Veverka, T. Dedourkova, P. Zvatora, P. Jendelova, A. Galisova, L. Kosinova, K. Jirakova and E. Sykova, "Using Ferromagnetic Nanoparticles with Low Curie Temperature for Magnetic Resonance Imaging-Guided Thermoablation," *Int. J. Nanomedicine*, vol. 11, pp. 3801-3811, 2016.

[122] Y. Shlapa, S. Solopan, A. Bodnaruk, M. Kulyk, V. Kalita, Y. Tykhonenko-Polishchuk, A. Tovstolytkin and A. Belous, "Effect of Synthesis Temperature on Structure and Magnetic Properties of $(La, Nd)_{0.7}Sr_{0.3}MnO_3$ Nanoparticles," *Nanoscale Res. Lett.*, vol. 12, no.1, 100, 2017.

[123] P. B. Santhosh, B. Drasler, D. Drobne, M. E. Kreft, S. Kralj, D. Makovec and N. P. Ulrih, "Effect of Superparamagnetic Iron Oxide Nanoparticles on Fluidity and Phase

Transition of Phosphatidylcholine Liposomal Membranes," *Int. J. Nanomedicine*, vol. 10, pp. 6089-6104, 2015.

[124] T. T. T. N'Guyen, H. T. T. Duong, J. Basuki, V. Montembault, S. Pascual, C. Guibert, J. Fresnais, C. Boyer, M. R. Whittaker, T. P. Davis and L. Fontaine, "Functional Iron Oxide Magnetic Nanoparticles with Hyperthermia-Induced Drug Release Ability by Using a Combination of Orthogonal Click Reactions," *Angew. Chem. Int. Ed.*, vol. 52, pp. 14152-14156, 2013.

[125] M. G. Weimuller, M. Zeisberger and K. M. Krishnan, "Size-Dependent Heating Rates of Iron Oxide Nanoparticles for Magnetic Fluid Hyperthermia," *J. Magn. Magn. Mater.*, vol. 321, no. 13, pp. 1947-1950, 2009.

[126] B. Kozissnik, A. C. Bohorquez, J. Dobson and C. Rinaldi, "Magnetic Fluid Hyperthermia: Advances, Challenges, and Opportunity," *Int. J. Hyperthermia*, vol. 29, no. 8, pp. 706-714, 2013.

[127] R. Kappiyoor, M. Liangruska, R. Ganguly and I. K. Puri, " The Effects of Magnetic Nanoparticle Properties on Magnetic Fluid Hyperthermia," *Journal of Applied Physics*, vol. 108, 094702, 2010.

[128] S. Laurent, S. Dutz, U. O. Hafeli and M. Mahmoudi, "Magnetic Fluid Hyperthermia: Focus on Superparamagnetic Iron Oxide Nanoparticles," *Advances in Colloid and Interface Science*, vol. 166, pp. 8-23, 2011.

[129] P. Kandesar, P. Chikode and S. Sabale, "Perspective of Magnetic Fluid Hyperthermia (MFH) for the Treatment of Tumor," *Tumor Res.*, vol. 2, no.1, 1000111, 2016.

[130] S. Santra, C. Kaittanis, J. Grimm and J. M. Perez, "Drug/Dye-Loaded, Multifunctional Iron Oxide Nanoparticles for Combined Targeted Cancer Theraphy and Dual Optical/MR-Imaging," *Small.*, vol. 5, no. 16, pp. 1862-1868, 2009.

[131] J. Lim, S. P. Yeap, H. X. Che and S. C. Low, " Characterization of Magnetic Nanoparticle by Dynamic Light Scattering," *Nanoscale Research Letters*, vol. 8, 381, 2013.

[132] S. Kumar, C. Ravikumar and R. Bandyopadhyaya, "State of Dispersion of Magnetic Nanoparticles in an Aqueous Medium: Experiments and Monte Carlo Simulation," *Langmuir*, vol. 26, no. 3, pp. 18320-18330, 2010.

[133] S. H. Huang, M. H. Liao and D. H. Chen, "Fast and Efficient Recovery of Lipase by Polyacrylic Acid-Coated Magnetic Nano-Adsorbent with High Activity Retention," *Separation and Purification Technology*, vol. 51, pp. 113-117, 2006.

[134] D. Couto, M. Freitas, V. Vilas-Boas, I. Dias, G. Porto, M. A. Lopez-Quintela, J. Rivas, P. Freitas, F. Carvalho and E. Fernandes, "Interaction of Polyacrylic Acid Coated and non-Coated Iron Oxide Nanoparticles with Human Neutrophils," *Toxicology Letters*, vol. 225, pp. 57-65, 2014.

[135] S. Campelj, D. Makovec and M. Drofenik, "Preparation and Properties of Water-Based Magnetic Fluids," *J. Phys.: Condens. Matter*, vol. 20, 204101, 5 pages, 2008.

[136] O. Veiseh, J. W. Gunn and M. Zhang, "Design and Fabrication of Magnetic Nanoparticles for Targeted Drug Delivery and Imaging," *Advanced Drug Delivery Reviews*, vol. 62, pp. 284-304, 2010.

[137] X. Kong, F. Su, L. Zhang, J. Yaron, F. Lee, Z. Shi, Y. Tian and D. R. Meldrum, "A Highly Selective Mitochondria-Targeting Fluorescent K^+ Sensor," *Angew. Chem. Int. Ed.*, vol. 54, pp. 12053-12057, 2015.

[138] D. Han and N. Kaplowitz, *Mitochondria in Liver Disease*, CRC Press, 2015.

[139] S. Kolemen, T. Ozdemir, D. Lee, G. M. Kim, T. Karatas, J. Yoon and E. U. Akkaya, "Remote-Controlled Release of Singlet Oxygen by the Plasmonic Heating of Endoperoxide-Modified Gold Nanorods: Towards a Paradigm Change in Photodynamic Therapy," *Angew. Chem. Int. Ed.*, vol. 55, no. 8, pp. 3606-3610, 2016.

[140] R. Massart, "Preparation of Aqueous Magnetic Liquids in Alkaline and Acidic Media," *IEEE Trans. Magn.*, vol. 17, no. 2, pp. 1247-1248, 1981.

[141] Y. Chen, J. Zhao, H. Guo and L. Xie, "Geometry Relaxation-Induced Large Stokes Shift in Red-Emitting Borondipyrromethenes (BODIPY) and Applications in Fluorescent Thiol Probes," *J. Org. Chem.*, vol. 77, no. 5, pp. 2192-2206, 2012.

[142] A. Yokoyama, T. Maruyama, K. Tagami, H. Masu, K. Katagiri, I. Azumaya and T. Yokozawa, "One-Pot Synthesis of Cyclic Triamides with a Triangular Cavity from *trans*-Stilbene and Diphenylacetylene Monomers," *Org. Lett.*, vol. 10, no. 15, pp. 3207-3210, 2008.

[143] G. A. Andrade, A. J. Pistner, G. P. A. Yap, D. A. Lutterman and J. Rosenthal, "Photocatalytic Conversion of CO_2 to CO Using Rhenium Bipyridine Platforms Containing Ancillary Phenyl or BODIPY Moieties," *ACS Catal.*, vol. 3, no. 8, pp. 1685-1692, 2013.

Appendix A

NMR Spectra

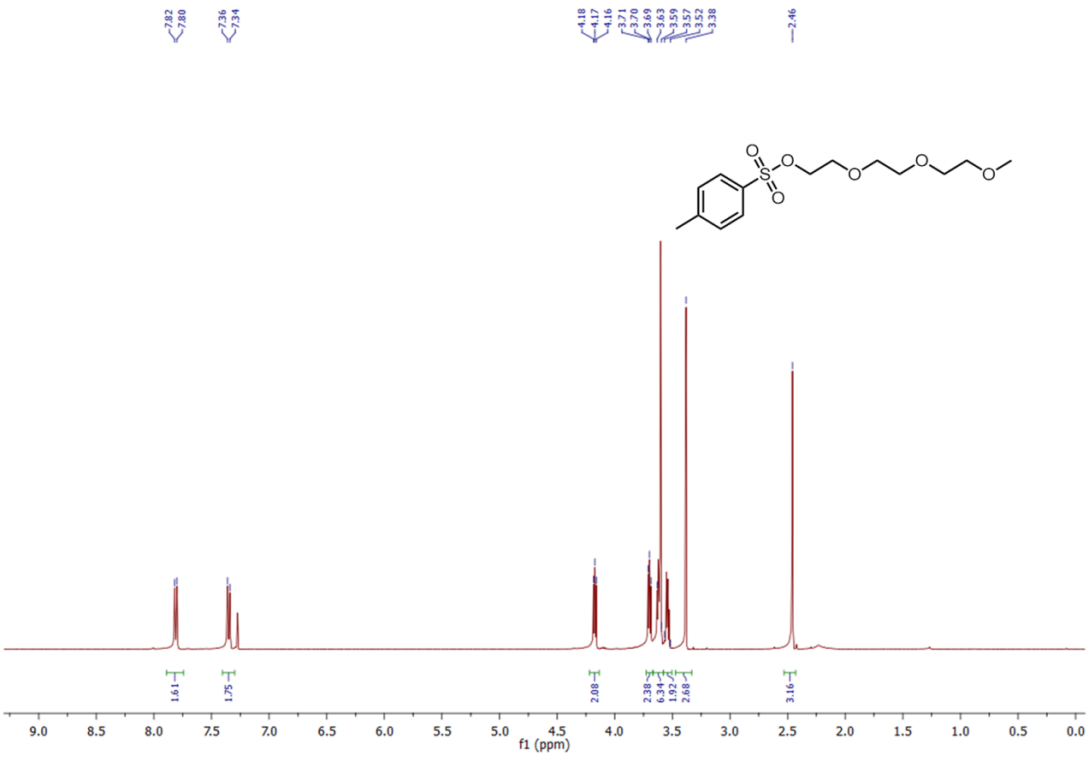

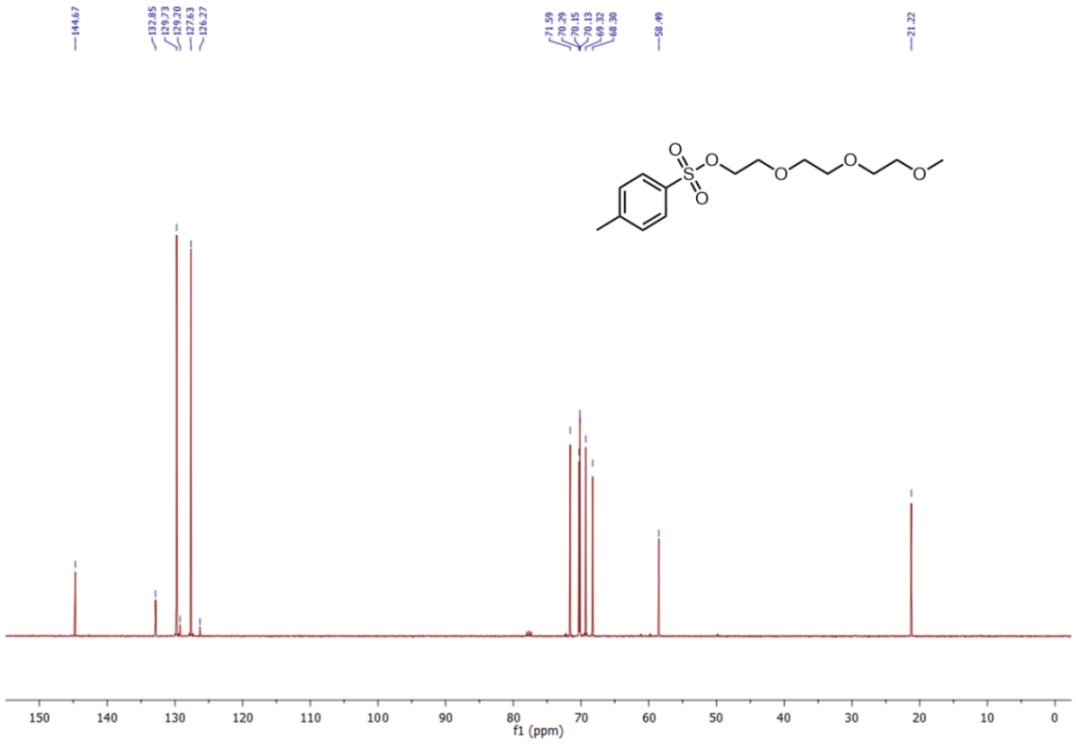
144.67
132.85
129.73
129.20
127.63
126.27
71.59
70.29
70.15
70.13
69.32
68.30
58.49
21.22
f1 (ppm)

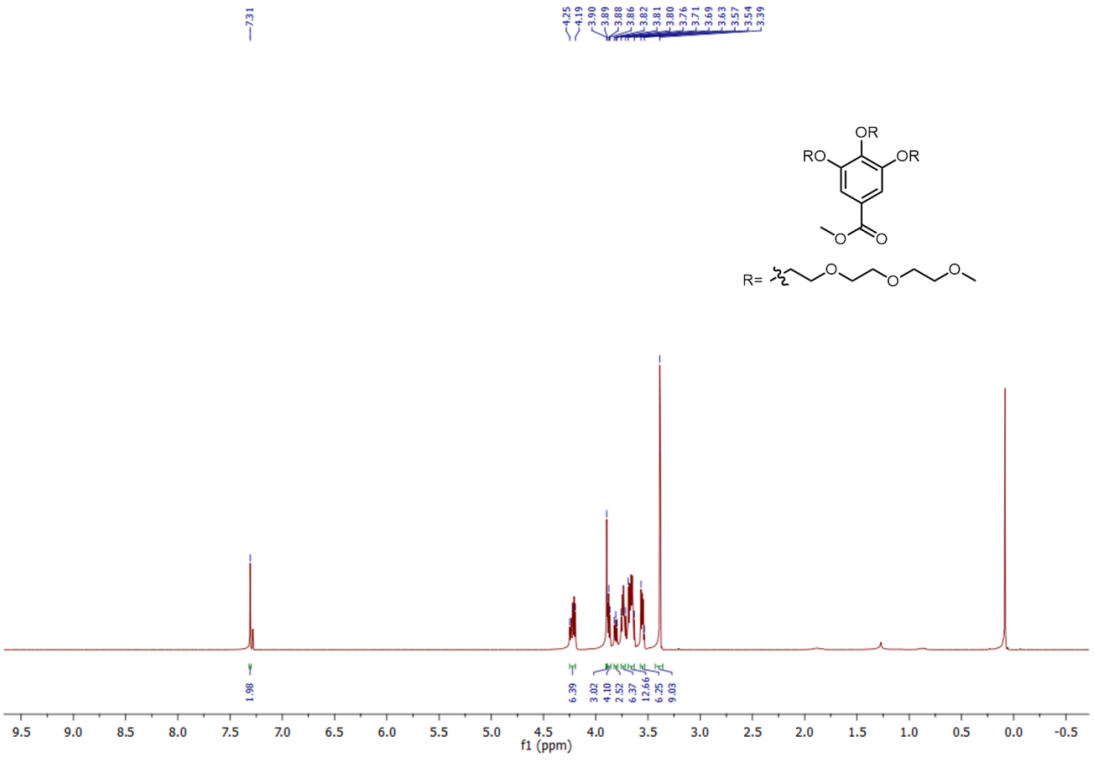
7.31
4.25
4.19
3.90
3.89
3.88
3.86
3.82
3.81
3.80
3.76
3.71
3.69
3.63
3.57
3.54
3.39
OR
RO
OR
R=
1.98
6.39
3.02
4.10
2.52
6.37
12.66
6.25
9.03
f1 (ppm)

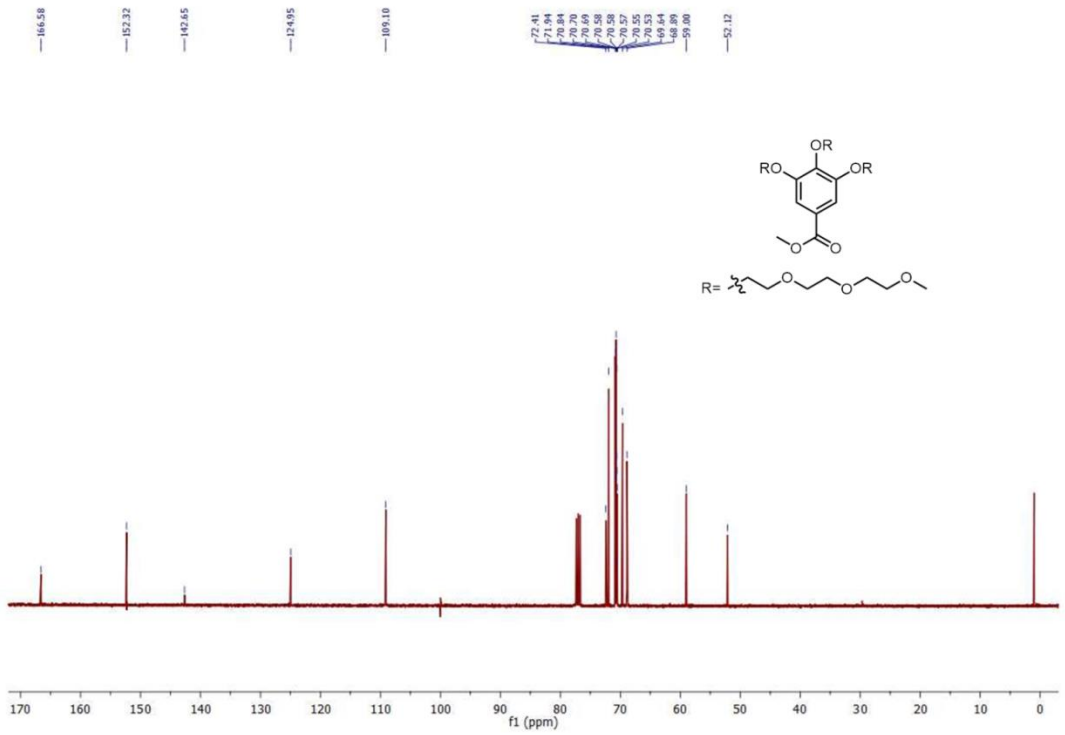
166.58
152.32
142.65
124.95
109.10
72.41
71.94
70.84
70.70
70.69
70.58
70.57
70.55
70.53
69.64
68.89
59.00
52.12
OR
RO
OR
O
O
R=
O
O
O
170
160
150
140
130
120
110
100
90
80
70
60
50
40
30
20
10
0
f1 (ppm)

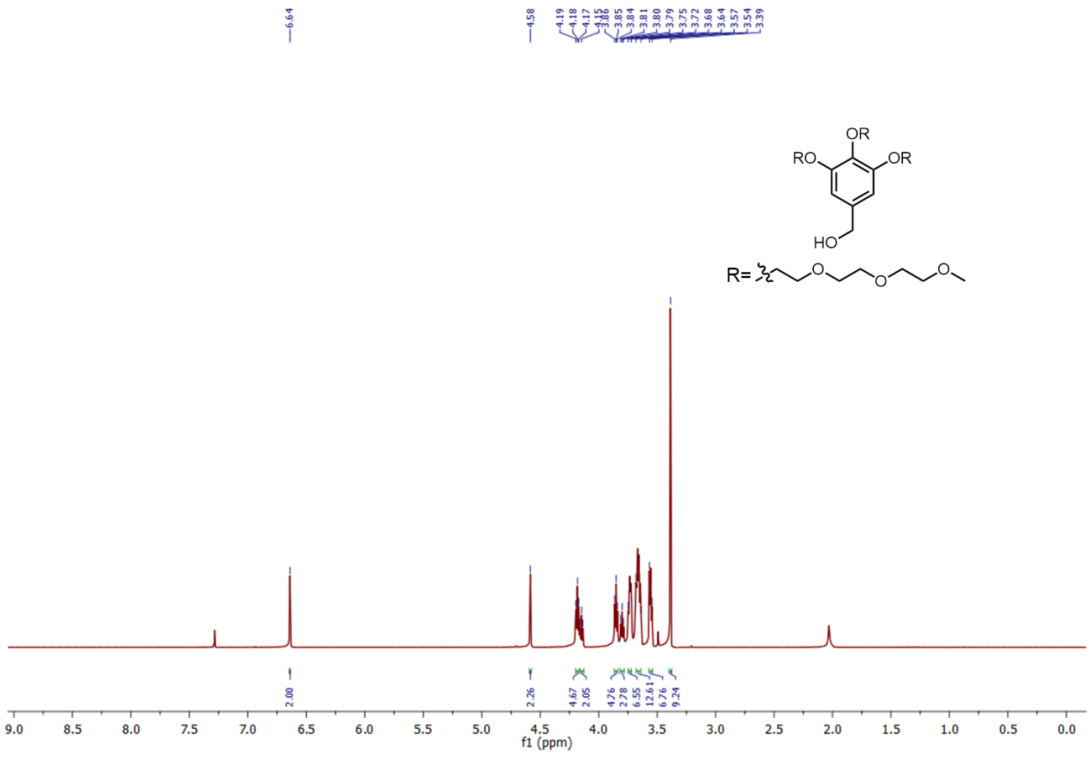
6.64
4.58
4.19
4.18
4.17
3.86
3.85
3.84
3.81
3.80
3.79
3.75
3.72
3.68
3.64
3.57
3.54
3.39
OR
RO
OR
HO
R=
O
O
O
2.00
2.26
4.67
2.05
4.76
2.78
6.55
12.61
6.76
9.24
9.0
8.5
8.0
7.5
7.0
6.5
6.0
5.5
5.0
4.5
4.0
3.5
3.0
2.5
2.0
1.5
1.0
0.5
0.0
f1 (ppm)

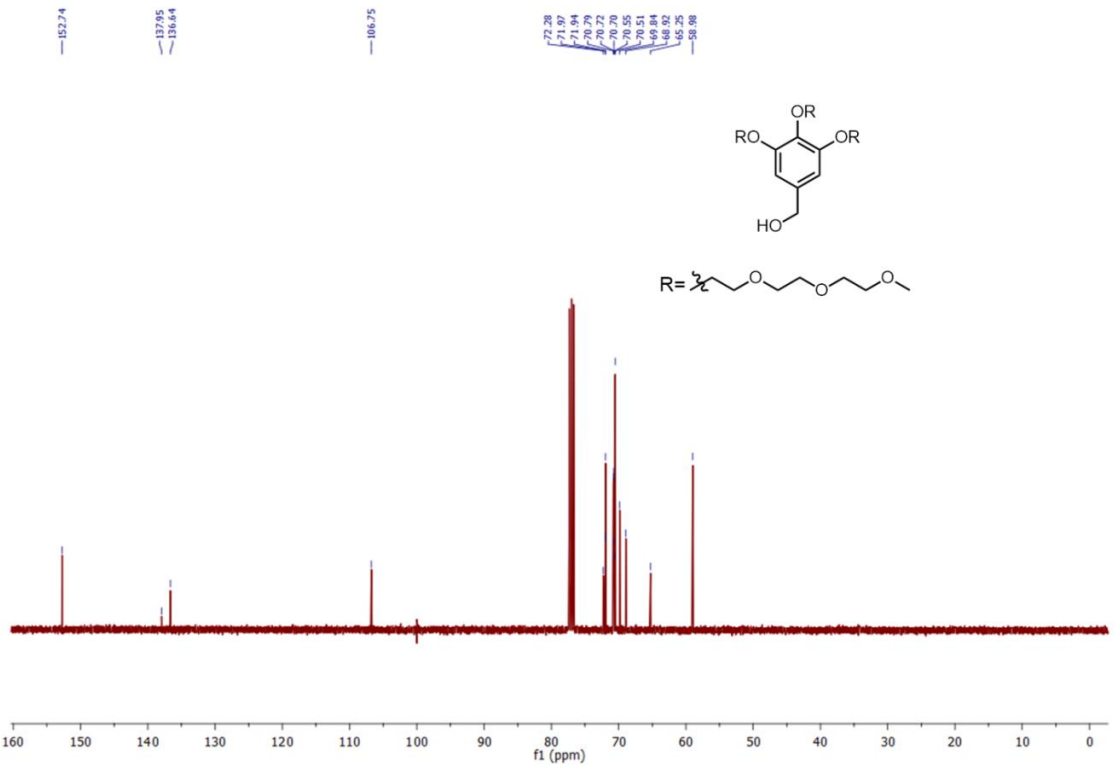
152.74
137.95
136.64
106.75
72.28
71.97
71.94
70.79
70.72
70.70
70.55
70.51
69.84
68.82
65.25
58.98
OR
RO
OR
HO
R=
160 150 140 130 120 110 100 90 80 70 60 50 40 30 20 10 0
f1 (ppm)

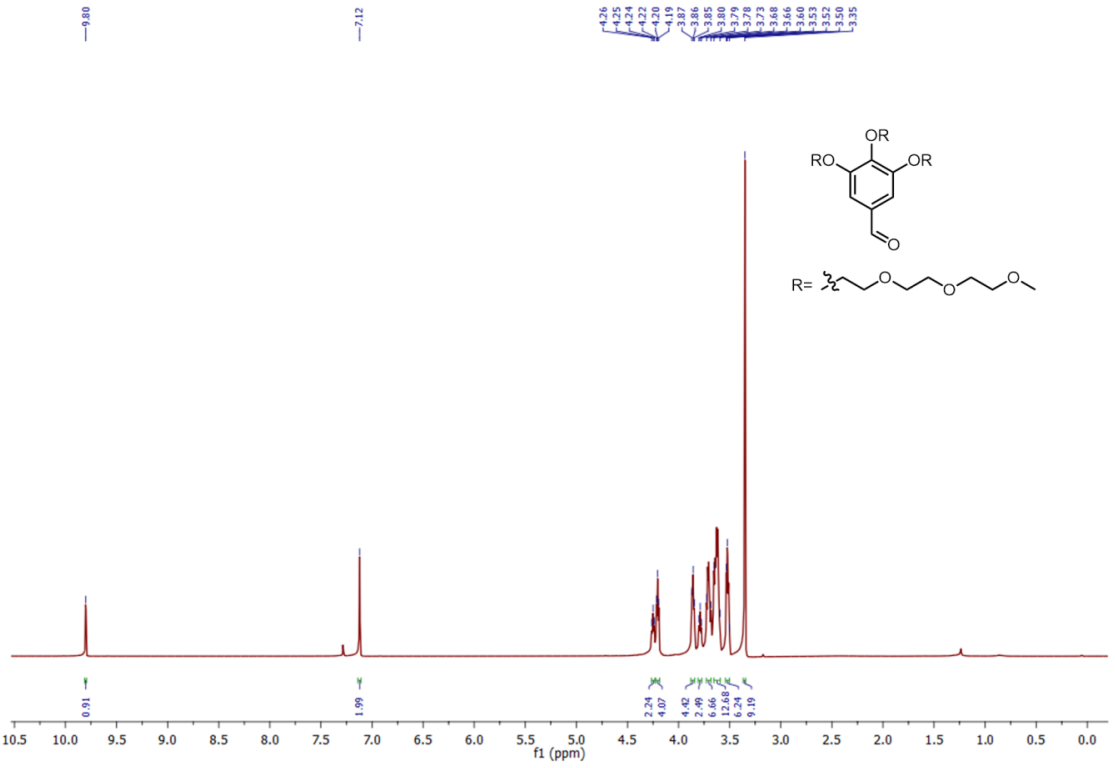
9.80
7.12
4.26
4.25
4.24
4.22
4.20
4.19
3.87
3.86
3.85
3.80
3.79
3.78
3.73
3.68
3.66
3.60
3.53
3.52
3.50
3.35
OR
RO
OR
O
R=
0.91
1.99
2.24
4.07
4.42
2.49
6.66
12.68
6.24
9.19
10.5 10.0 9.5 9.0 8.5 8.0 7.5 7.0 6.5 6.0 5.5 5.0 4.5 4.0 3.5 3.0 2.5 2.0 1.5 1.0 0.5 0.0
f1 (ppm)

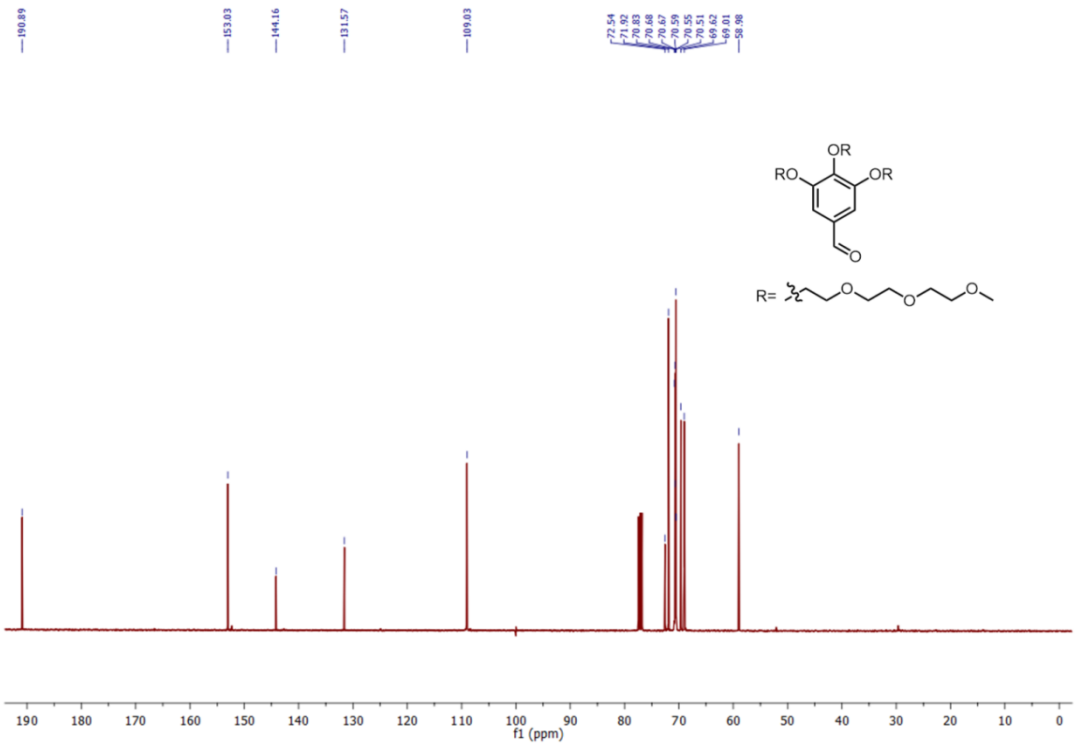
190.89
153.03
144.16
131.57
109.03
72.54
71.92
70.83
70.68
70.67
70.59
70.55
70.51
69.62
69.01
58.98
OR
RO
OR
O
R=
O
O
O
190
180
170
160
150
140
130
120
110
100
90
80
70
60
50
40
30
20
10
0
f1 (ppm)

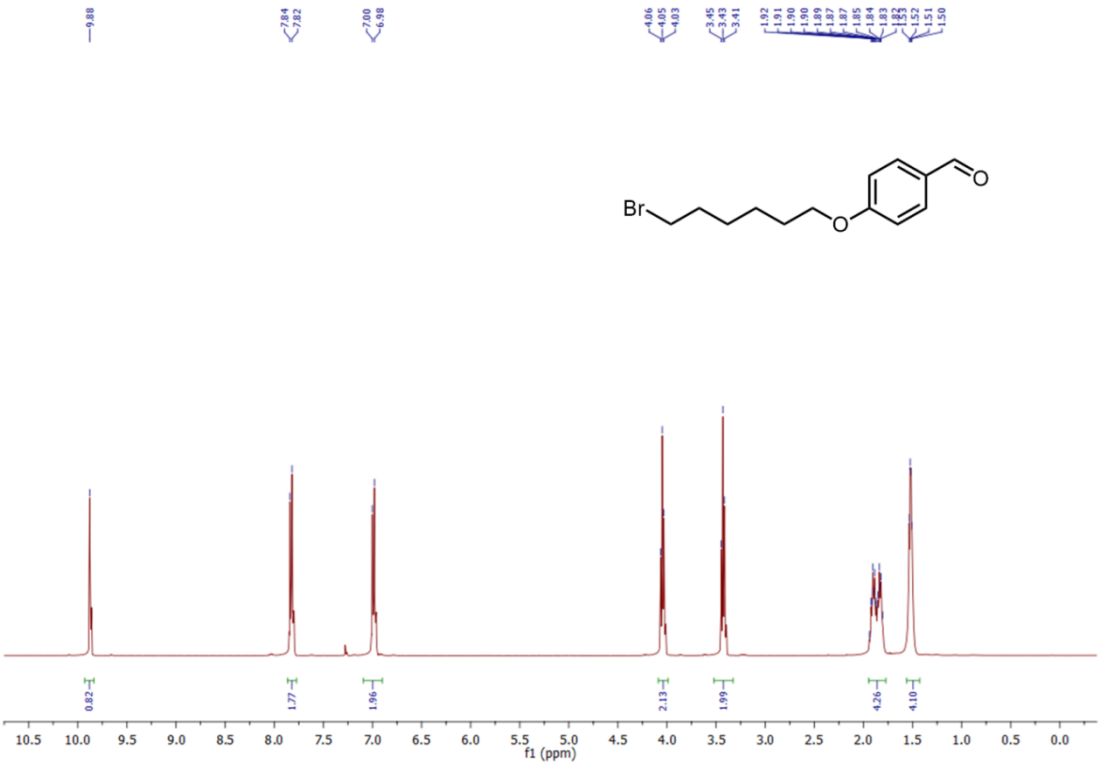
9.88
7.84
7.82
7.00
6.98
4.06
4.05
4.03
3.45
3.43
3.41
1.92
1.91
1.90
1.90
1.89
1.87
1.87
1.85
1.84
1.83
1.52
1.51
1.50
Br
O
O
0.82
1.77
1.96
2.13
1.99
4.26
4.10
10.5
10.0
9.5
9.0
8.5
8.0
7.5
7.0
6.5
6.0
5.5
5.0
4.5
4.0
3.5
3.0
2.5
2.0
1.5
1.0
0.5
0.0
f1 (ppm)

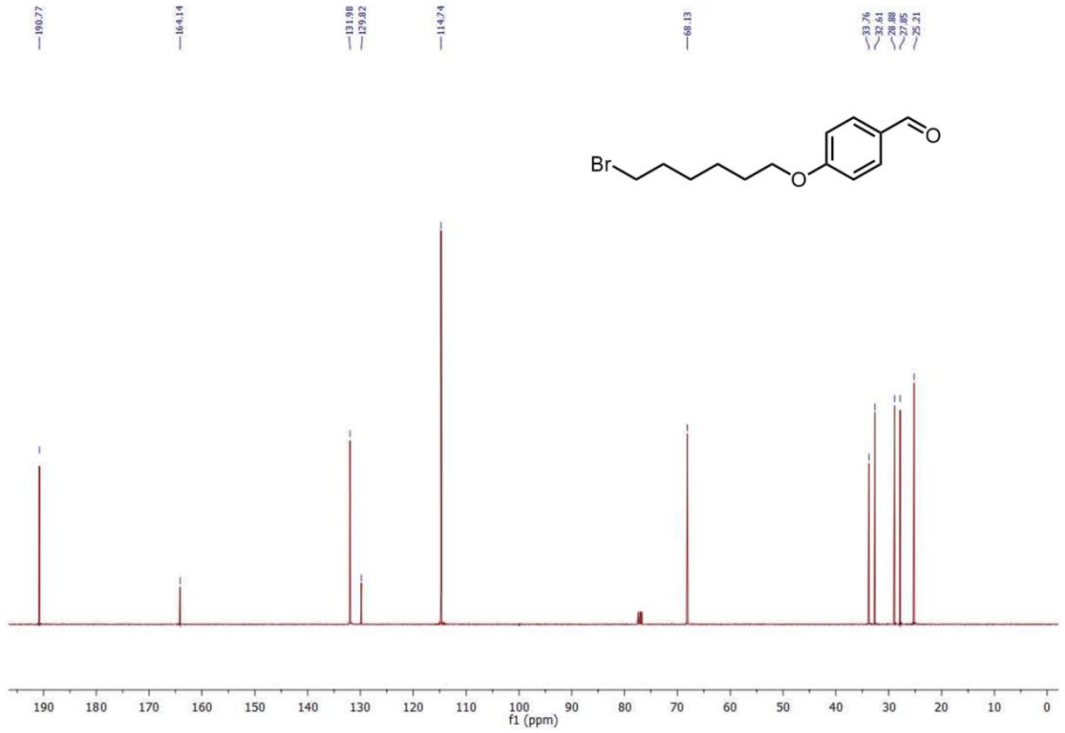
190.77
164.14
131.98
129.82
114.74
68.13
33.76
29.61
28.88
27.85
25.21
Br
O
O
f1 (ppm)


9.79
9.78
7.81
7.79
7.79
7.78
7.77
7.76
7.75
7.75
7.73
7.72
7.72
7.68
7.68
7.67
7.67
7.66
7.65
6.92
6.92
6.90
6.90
3.99
3.97
3.95
3.80
3.74
3.68
1.73
1.72
1.70
1.64
1.63
1.61
1.47
1.45
1.44
1.44
1.42

Br
O(CH2)6PPh3
O
0.88
17.40
1.91
1.96
1.97
4.11
1.98
1.98
f1 (ppm)

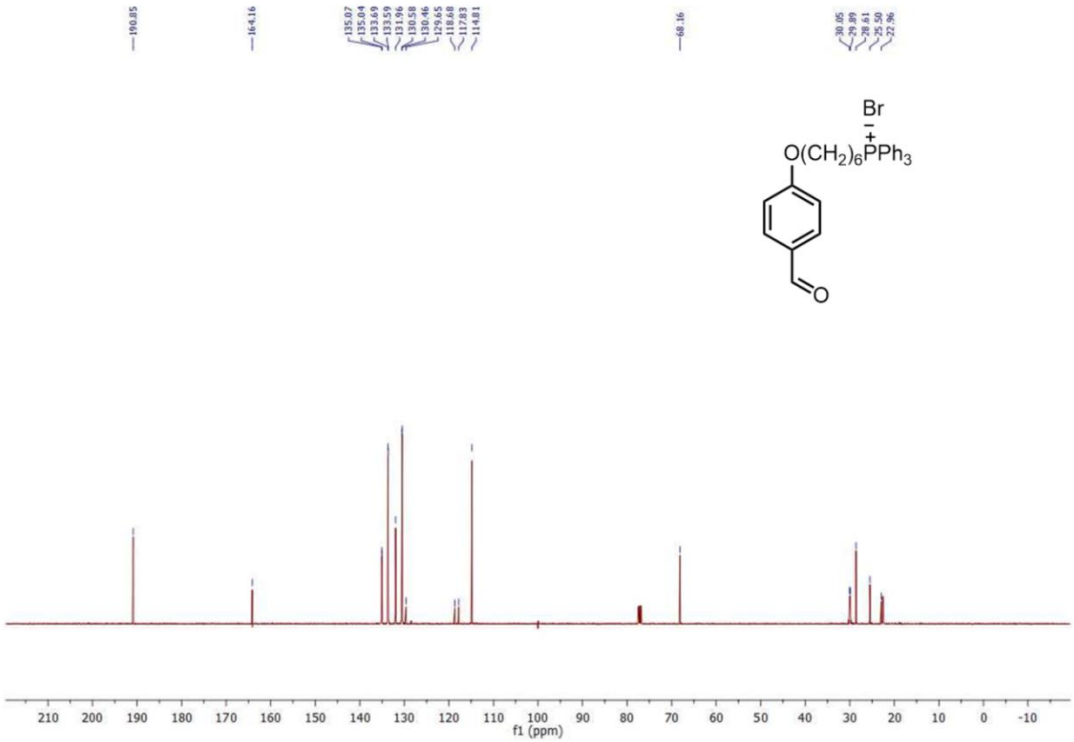
190.85
164.16
135.07
135.04
133.69
133.59
131.96
130.58
130.46
129.65
117.68
117.23
114.81
68.16
30.05
29.89
28.61
25.50
22.96
Br
O(CH2)6PPh3
O
f1 (ppm)

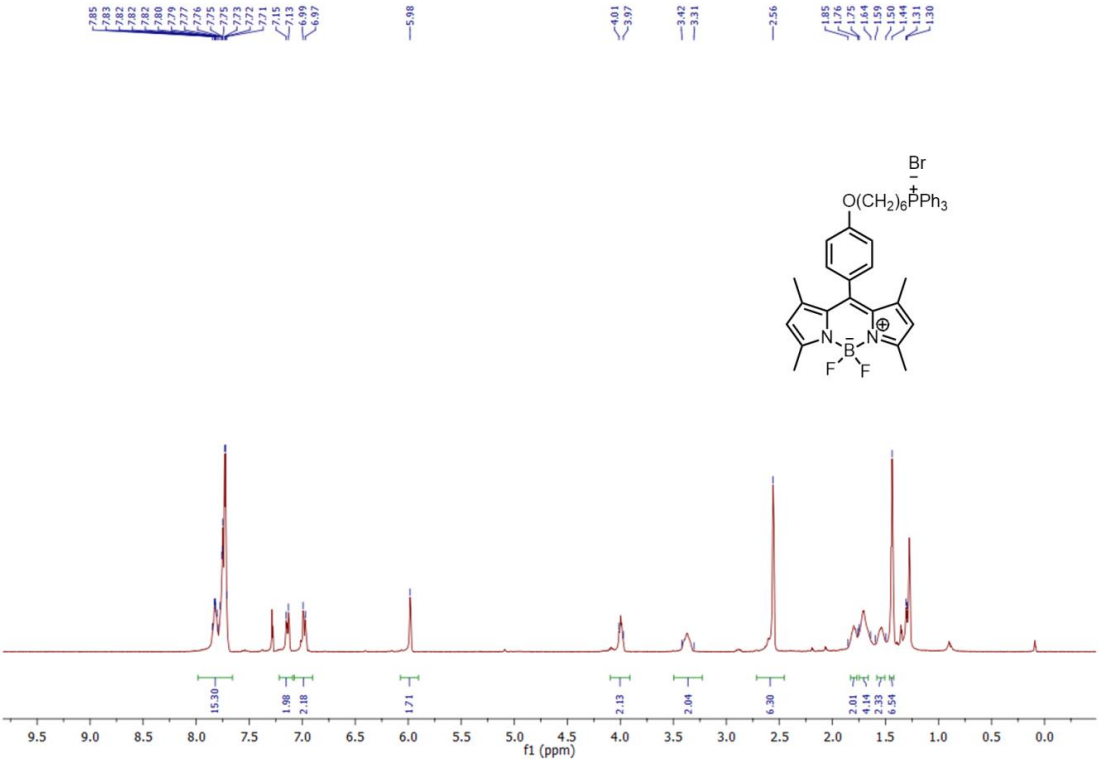
7.85
7.83
7.82
7.82
7.82
7.80
7.79
7.77
7.76
7.75
7.75
7.73
7.72
7.71
7.15
7.13
6.99
6.97
5.98
4.01
3.97
3.42
3.31
2.56
1.85
1.76
1.75
1.64
1.59
1.50
1.44
1.31
1.30
Br
O(CH2)6PPh3
N
B
F
F
15.30
1.98
2.18
1.71
2.13
2.04
6.30
2.01
4.14
2.33
6.54
f1 (ppm)

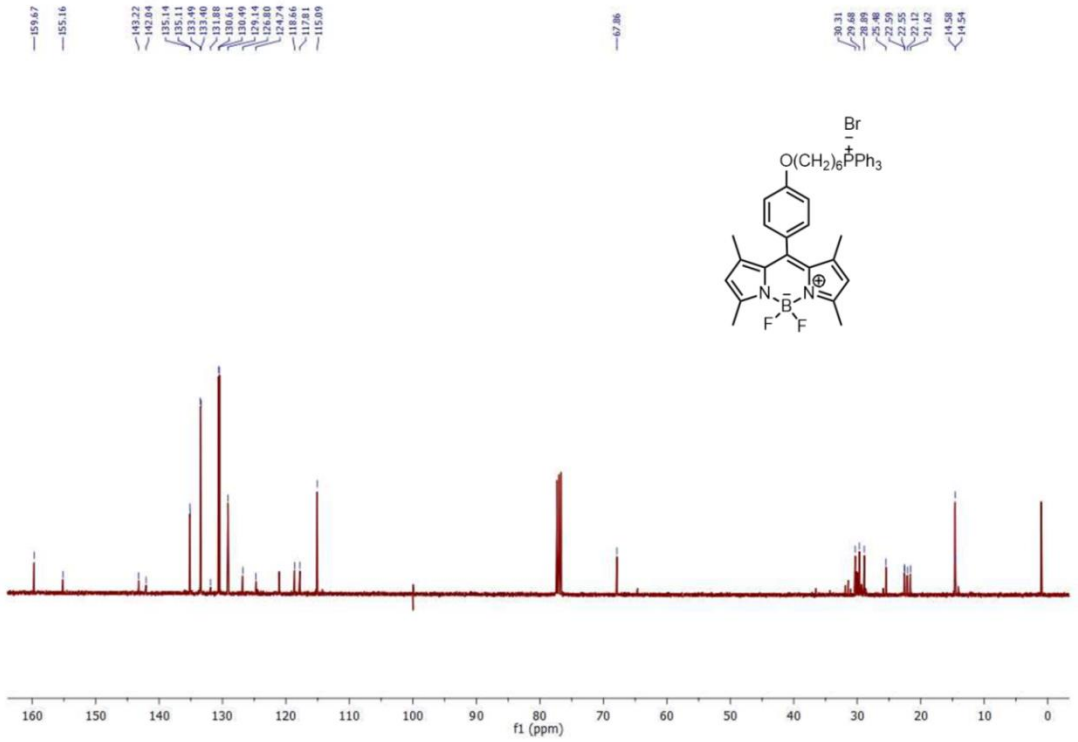
159.67
155.16
143.22
142.04
135.14
135.11
133.49
133.40
131.88
130.61
130.49
129.14
128.66
124.74
118.66
117.81
115.09
67.86
30.31
29.68
28.89
25.48
22.59
22.55
22.12
21.62
14.58
14.54
Br
O(CH2)6PPh3
N
B
F
F
160
150
140
130
120
110
100
90
80
70
60
50
40
30
20
10
0
f1 (ppm)

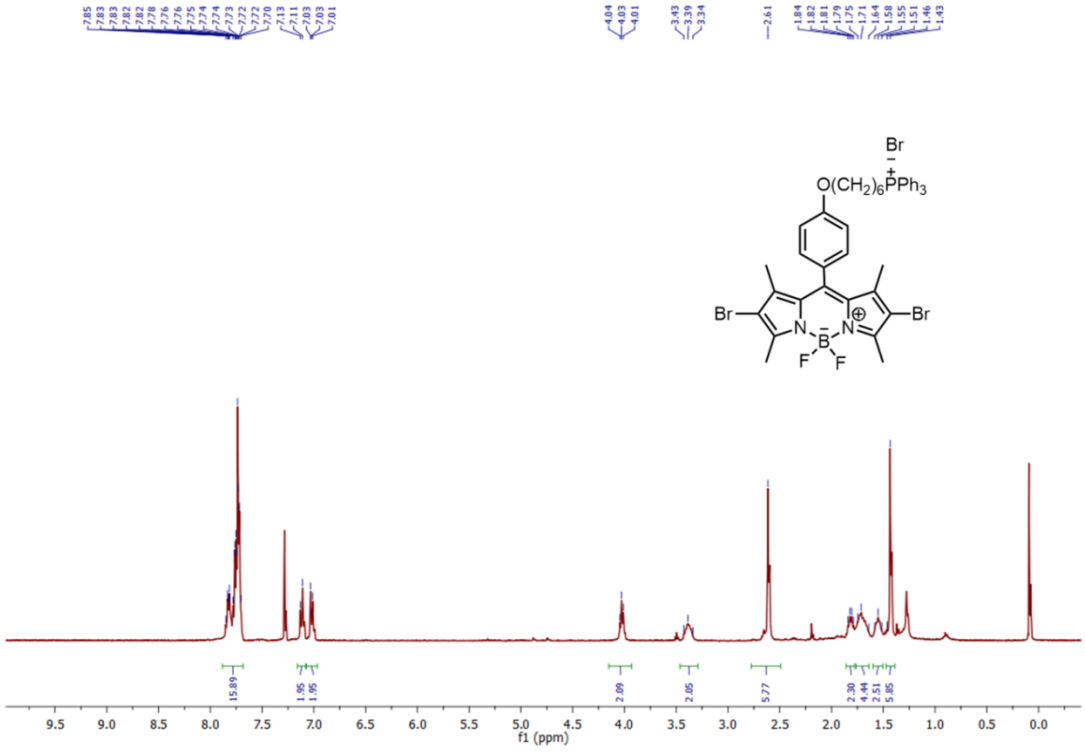
7.85
7.83
7.83
7.82
7.82
7.78
7.76
7.76
7.75
7.74
7.74
7.73
7.72
7.72
7.70
7.13
7.11
7.03
7.03
7.01
4.04
4.03
4.01
3.43
3.39
3.34
2.61
1.84
1.82
1.81
1.79
1.75
1.71
1.64
1.58
1.55
1.51
1.46
1.43
Br
O(CH2)6PPh3
Br
Br
N
B
F
F
15.89
1.95
1.95
2.09
2.05
5.77
2.30
4.44
2.51
5.85
9.5
9.0
8.5
8.0
7.5
7.0
6.5
6.0
5.5
5.0
4.5
4.0
3.5
3.0
2.5
2.0
1.5
1.0
0.5
0.0
f1 (ppm)

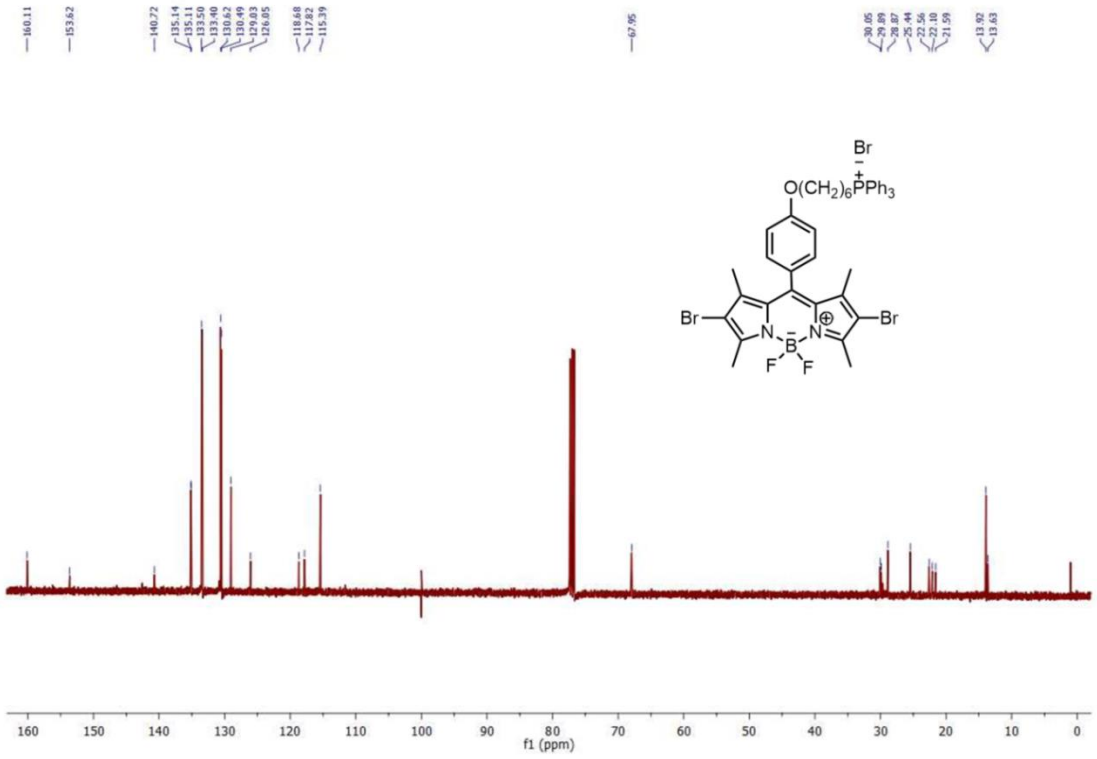
Br
O(CH2)6PPh3
Br
Br
N
B
N
F
F
f1 (ppm)

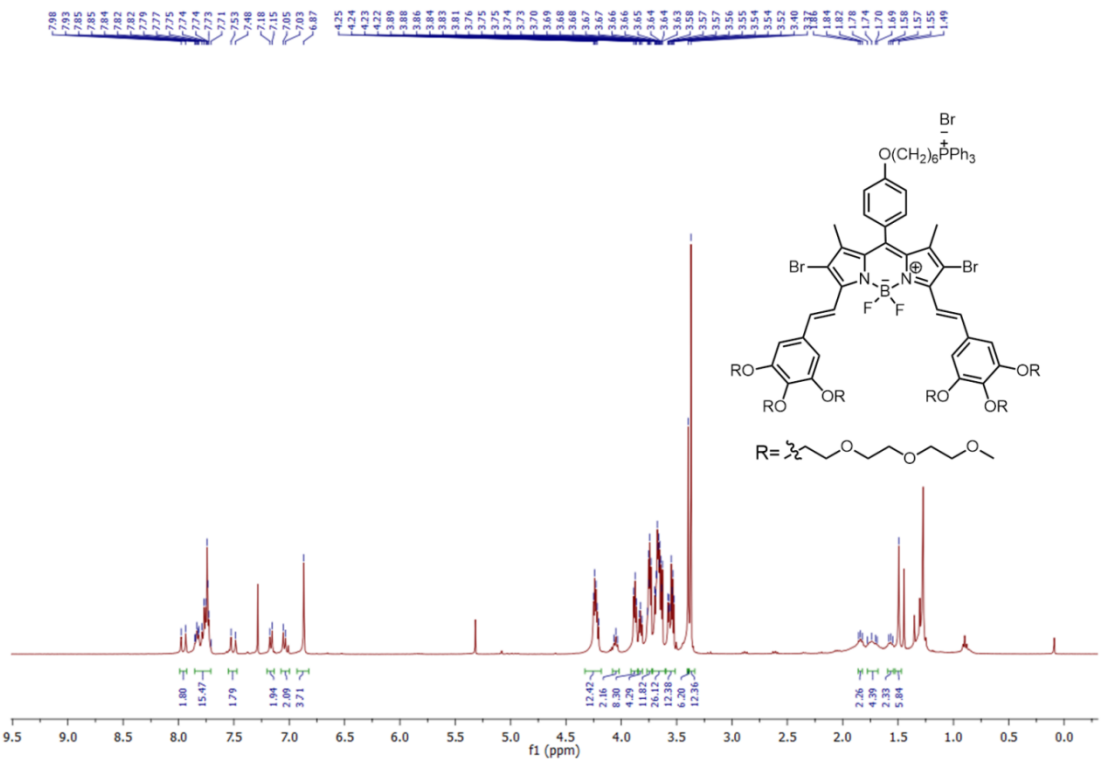
Br
O(CH2)6PPh3
Br
Br
RO
OR
R=
f1 (ppm)

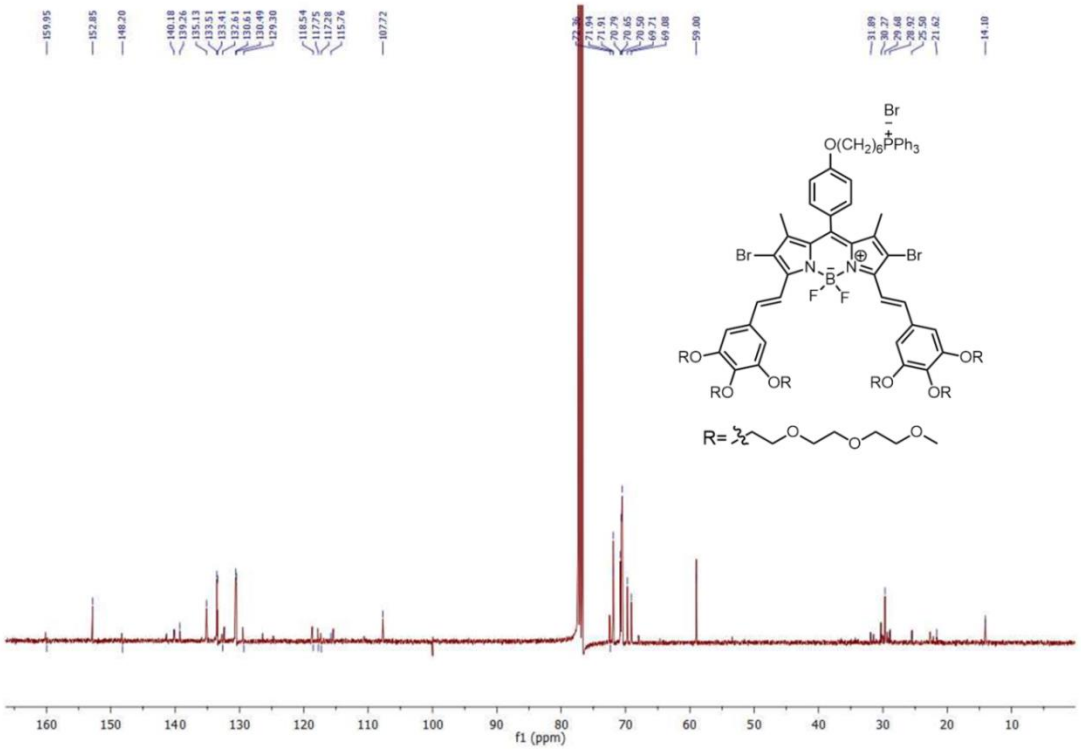
f1 (ppm)
R=

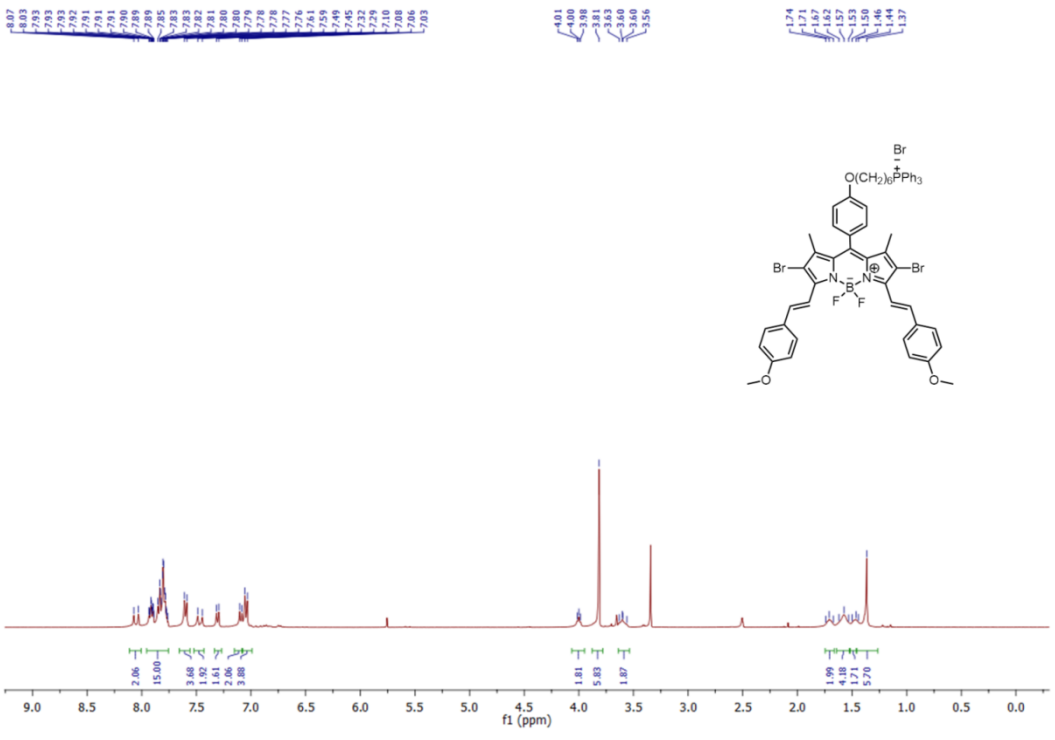
f1 (ppm)

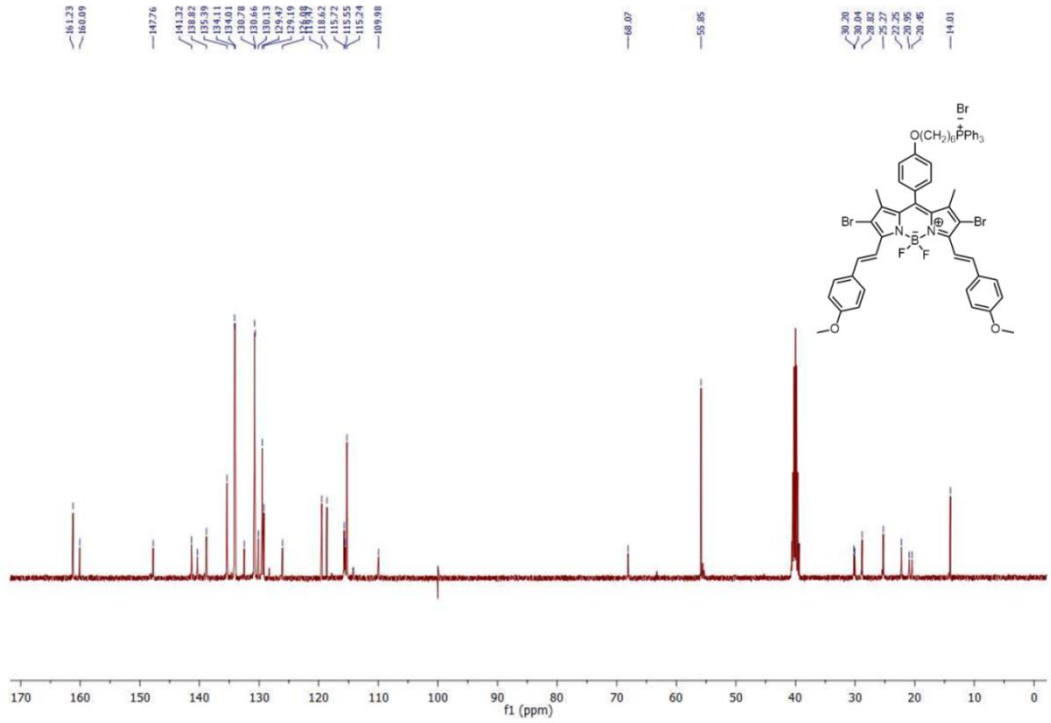
161.23
160.09
147.76
141.32
138.82
135.59
134.11
131.61
130.78
130.66
130.13
129.47
129.19
118.62
115.72
115.55
115.24
109.98
68.07
55.85
30.20
30.04
28.82
25.27
23.25
20.95
20.45
14.01
Br
O(CH2)6PPh3
Br
Br
N
B
F
F
O
O
170
160
150
140
130
120
110
100
90
80
70
60
50
40
30
20
10
0
f1 (ppm)

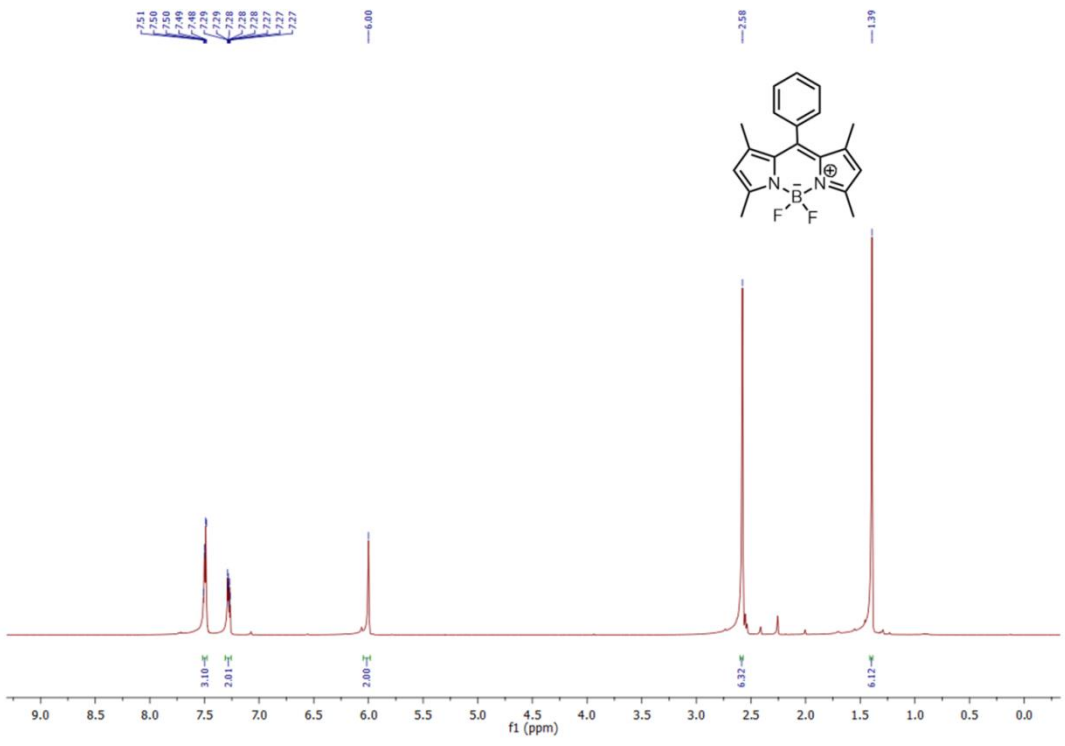
7.51
7.50
7.50
7.49
7.48
7.29
7.29
7.28
7.28
7.28
7.27
7.27
7.27
6.00
2.58
1.39
N
B
F
F
3.10
2.01
2.00
6.32
6.12
9.0
8.5
8.0
7.5
7.0
6.5
6.0
5.5
5.0
4.5
4.0
3.5
3.0
2.5
2.0
1.5
1.0
0.5
0.0
f1 (ppm)

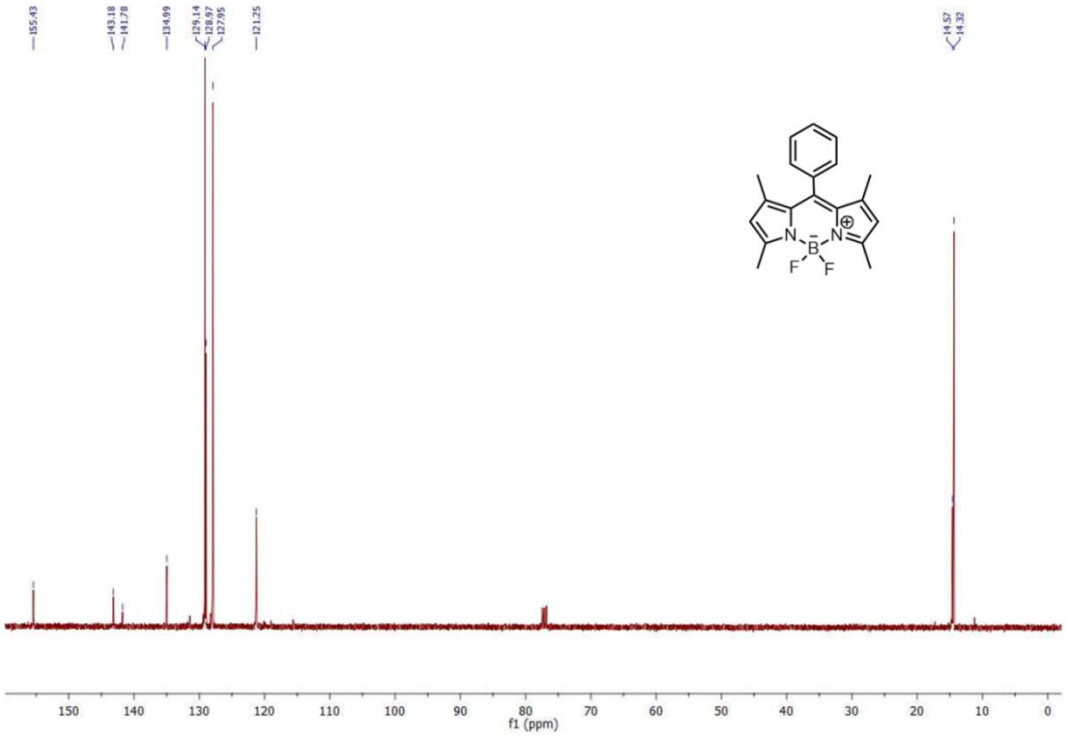
155.43
143.18
141.78
134.99
129.14
128.97
127.95
121.25
14.57
14.32
F
B
F
N
N
150
140
130
120
110
100
90
80
70
60
50
40
30
20
10
0
f1 (ppm)

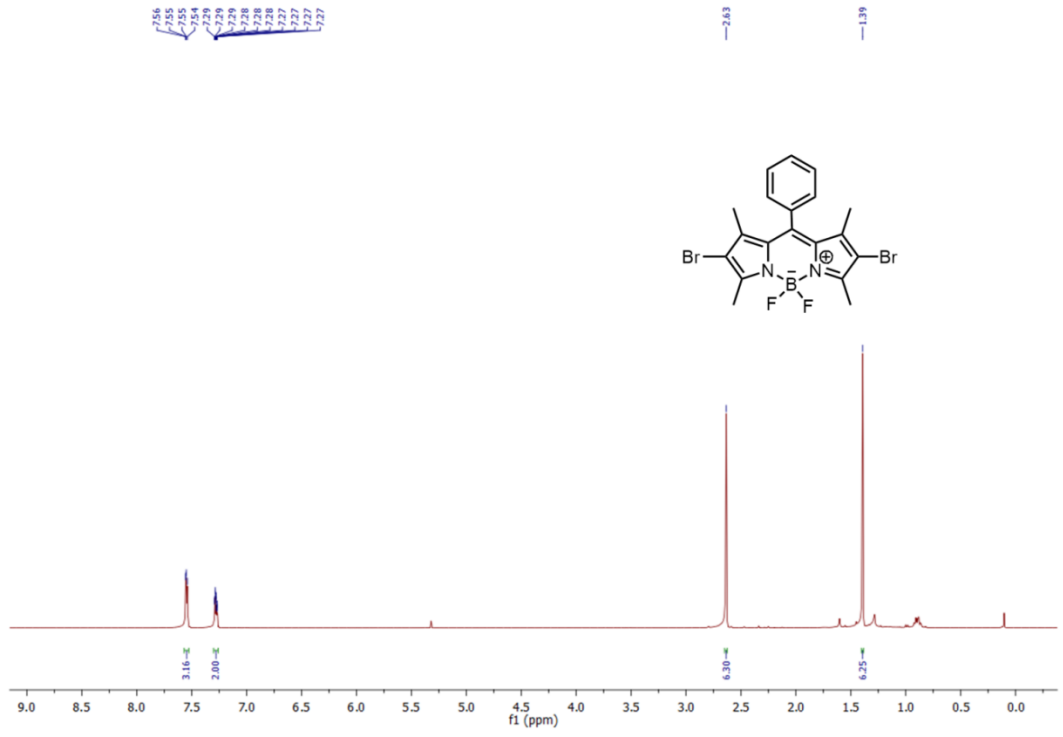
7.56
7.55
7.55
7.54
7.29
7.29
7.29
7.28
7.28
7.28
7.27
7.27
7.27
7.27
2.63
1.39
Br
Br
F
B
F
N
N
3.16
2.00
6.30
6.25
9.0
8.5
8.0
7.5
7.0
6.5
6.0
5.5
5.0
4.5
4.0
3.5
3.0
2.5
2.0
1.5
1.0
0.5
0.0
f1 (ppm)

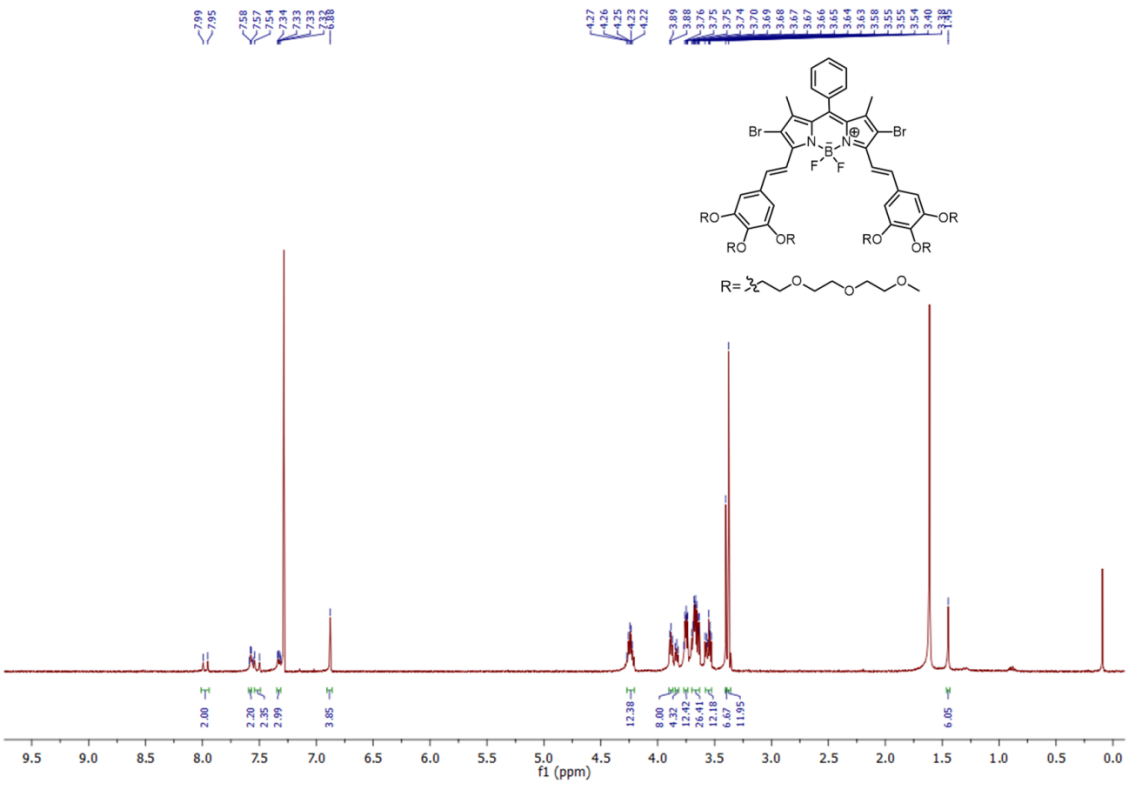
Br
Br
N
B
F
F
RO
OR
RO
OR
RO
OR
RO
OR
R=
O
O
O
f1 (ppm)

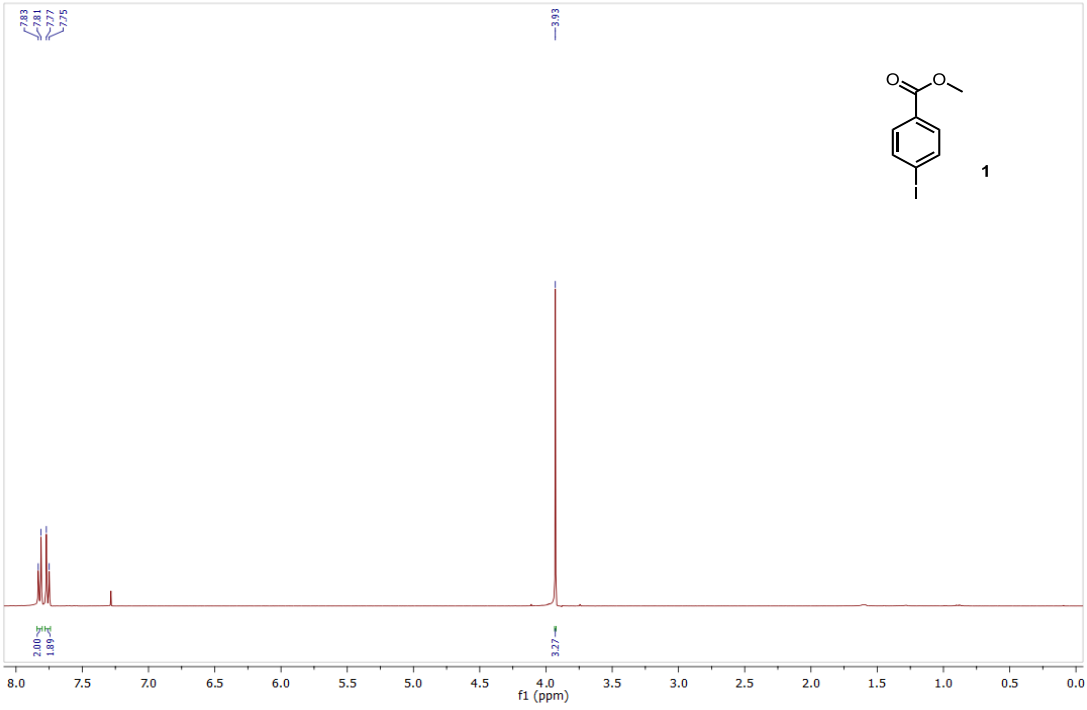
O
O
I
1
f1 (ppm)

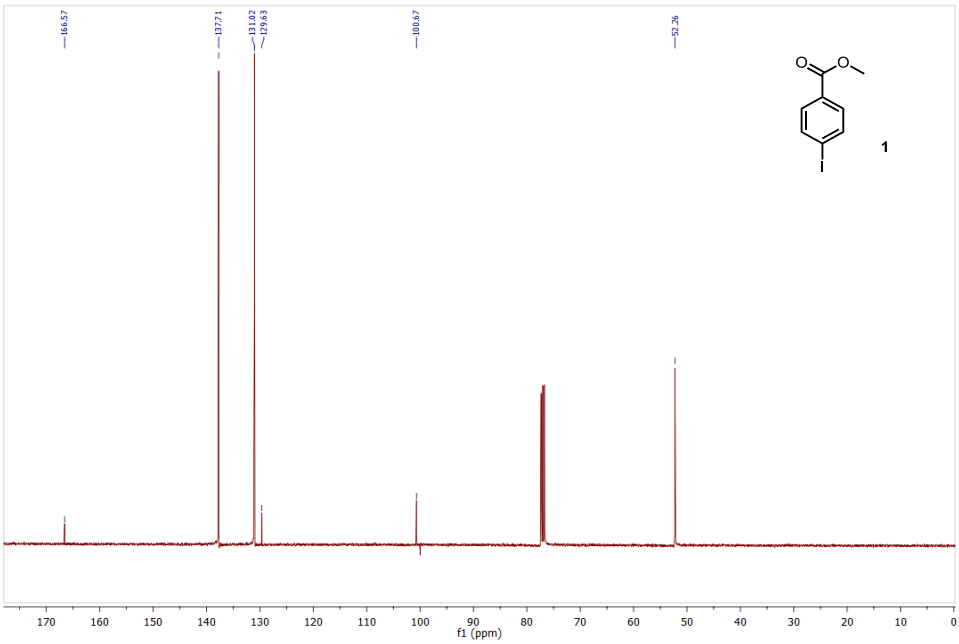
166.57
137.71
131.02
129.83
100.67
52.26
1
f1 (ppm)

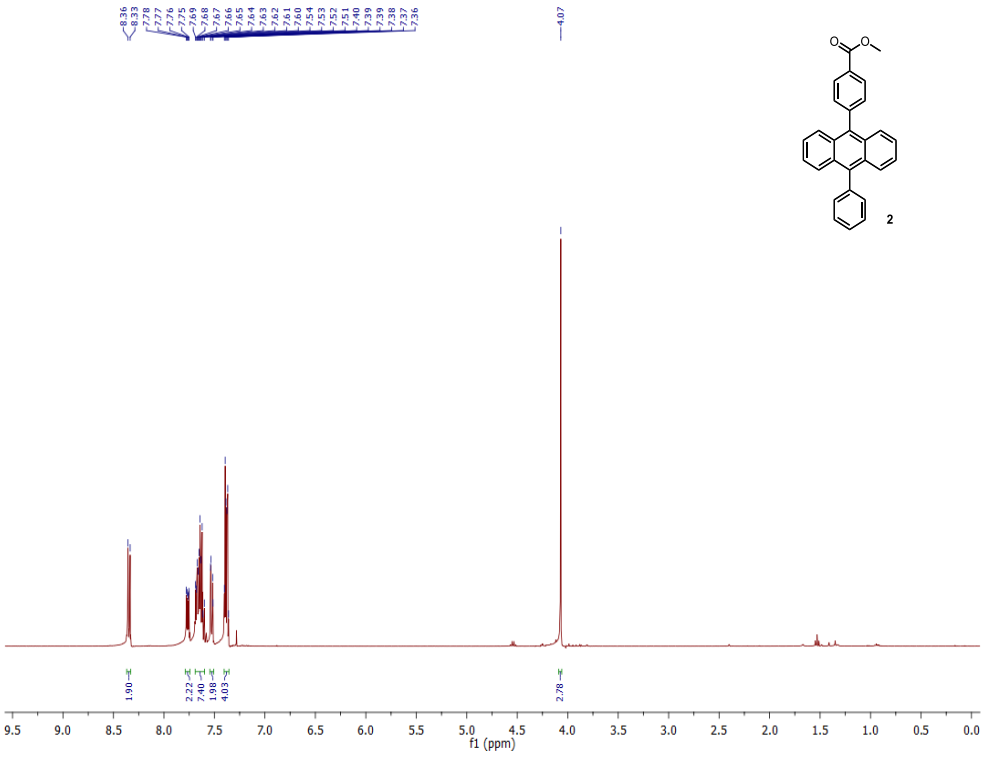
8.36
8.33
7.78
7.77
7.76
7.75
7.69
7.68
7.67
7.66
7.65
7.64
7.63
7.62
7.61
7.60
7.54
7.53
7.52
7.51
7.40
7.39
7.38
7.37
7.36
4.07
2
1.90
2.22
7.40
1.98
4.03
2.78
f1 (ppm)

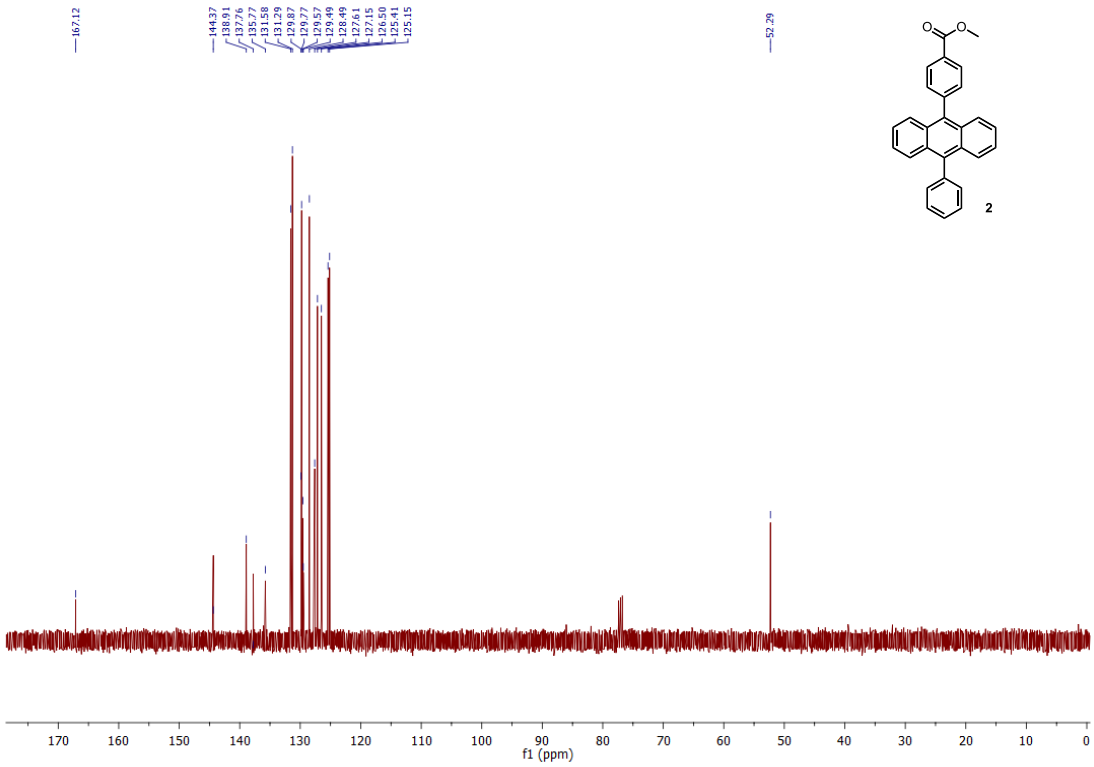
167.12
144.37
138.91
137.76
135.77
131.58
131.29
129.87
129.77
129.57
129.49
128.49
127.61
127.15
126.50
125.41
125.15
52.29
O
O
2
170
160
150
140
130
120
110
100
90
80
70
60
50
40
30
20
10
0
f1 (ppm)

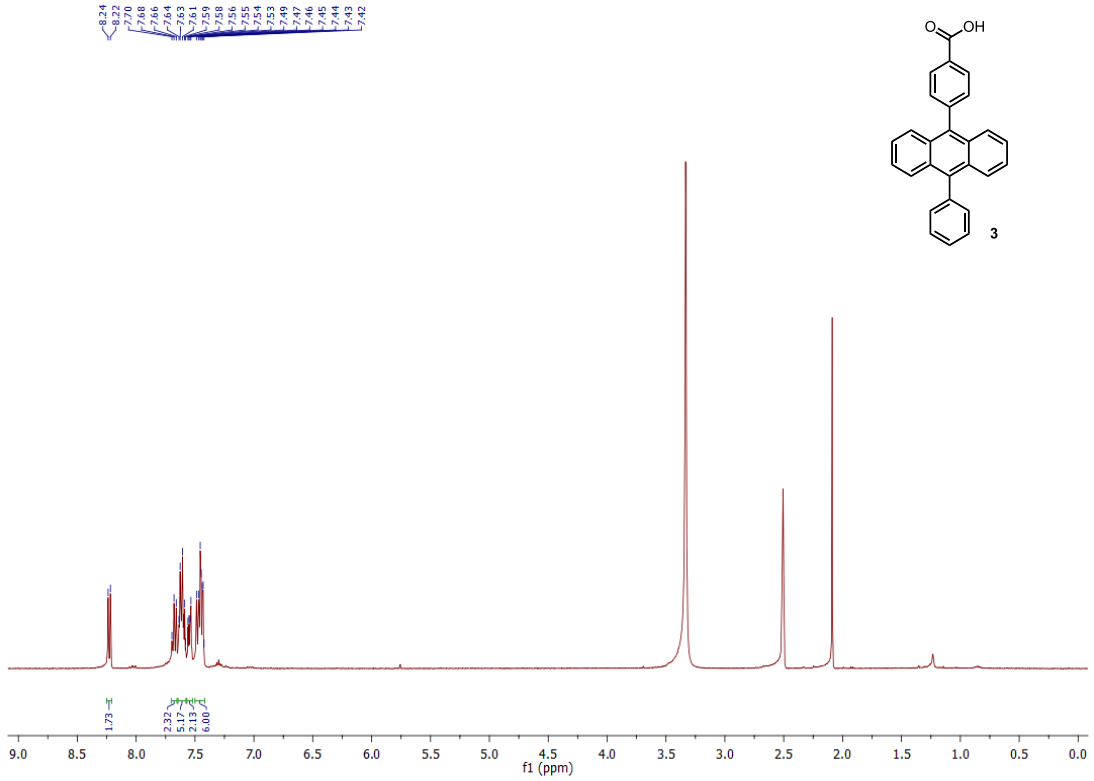
8.24
8.22
7.70
7.68
7.66
7.64
7.63
7.61
7.59
7.58
7.56
7.55
7.54
7.53
7.49
7.47
7.46
7.45
7.44
7.43
7.42
O
OH
3
1.73
2.32
5.17
2.13
6.00
9.0
8.5
8.0
7.5
7.0
6.5
6.0
5.5
5.0
4.5
4.0
3.5
3.0
2.5
2.0
1.5
1.0
0.5
0.0
f1 (ppm)

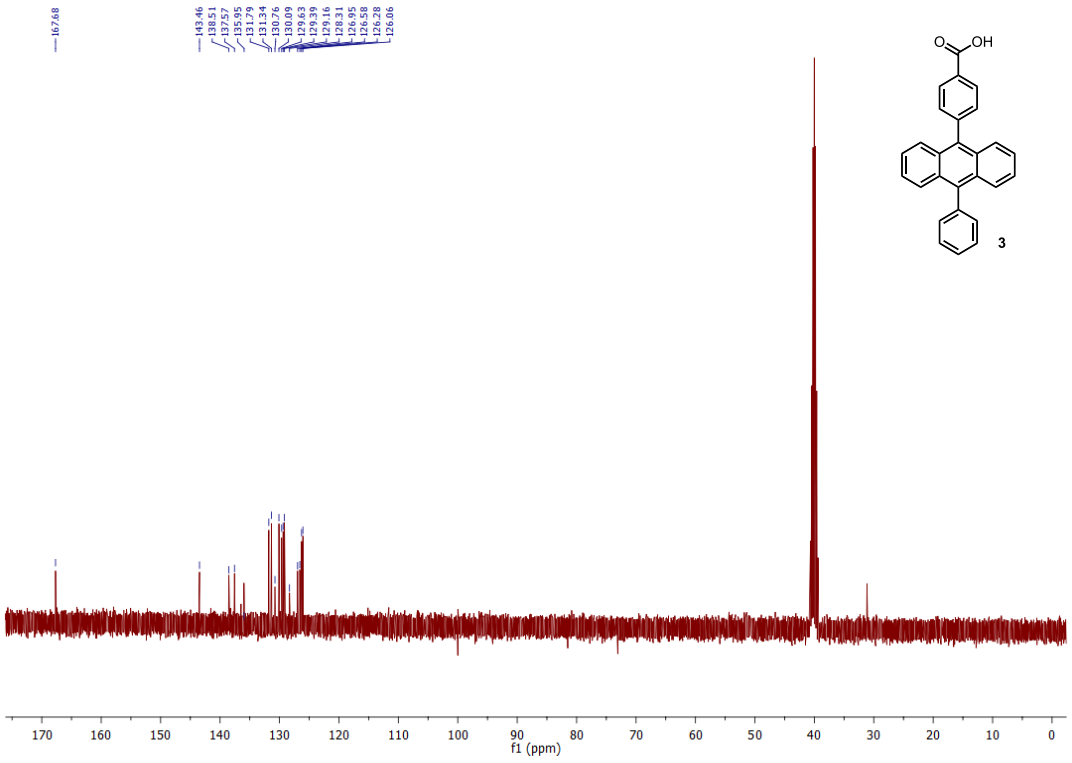
167.68
143.46
139.51
137.57
135.55
131.79
131.34
130.76
130.09
129.63
129.39
129.16
128.31
126.95
126.58
126.38
126.06
OH
3
170 160 150 140 130 120 110 100 90 80 70 60 50 40 30 20 10 0
f1 (ppm)

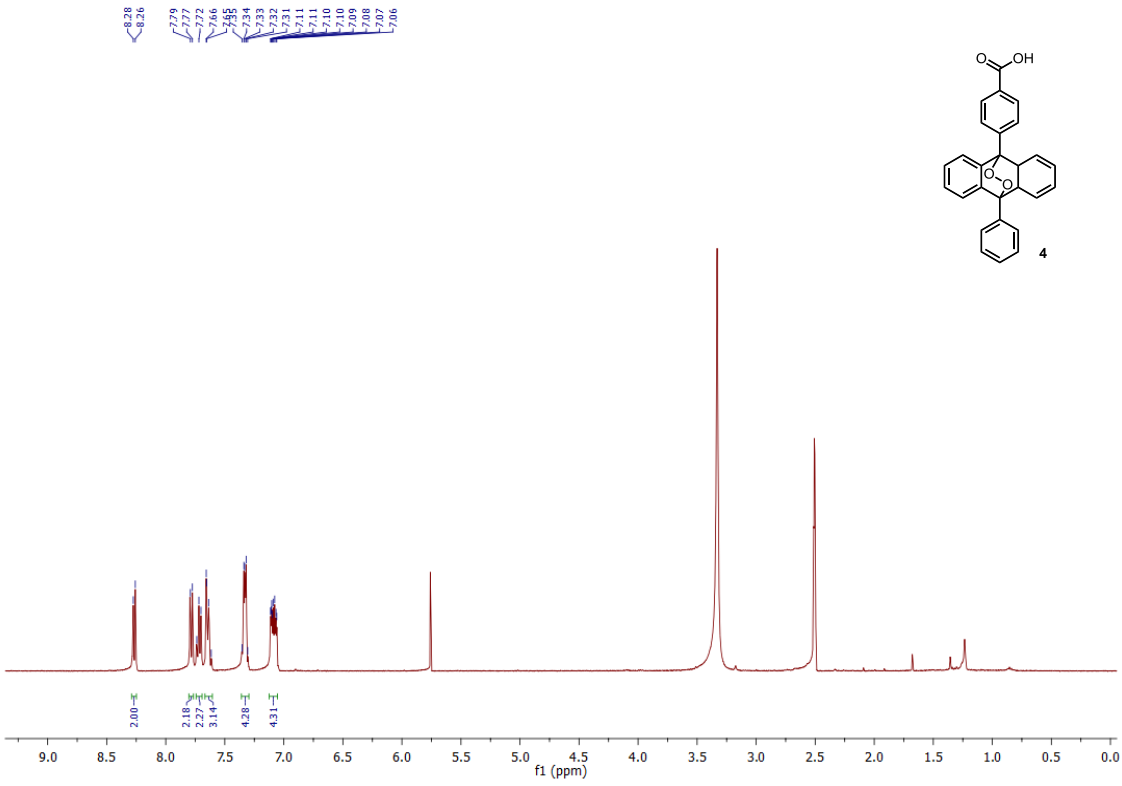
8.28
8.26
7.79
7.77
7.72
7.66
7.35
7.34
7.33
7.32
7.31
7.11
7.11
7.10
7.10
7.09
7.08
7.07
7.06
OH
O
O
4
2.00
2.18
2.27
3.14
4.28
4.31
9.0 8.5 8.0 7.5 7.0 6.5 6.0 5.5 5.0 4.5 4.0 3.5 3.0 2.5 2.0 1.5 1.0 0.5 0.0
f1 (ppm)

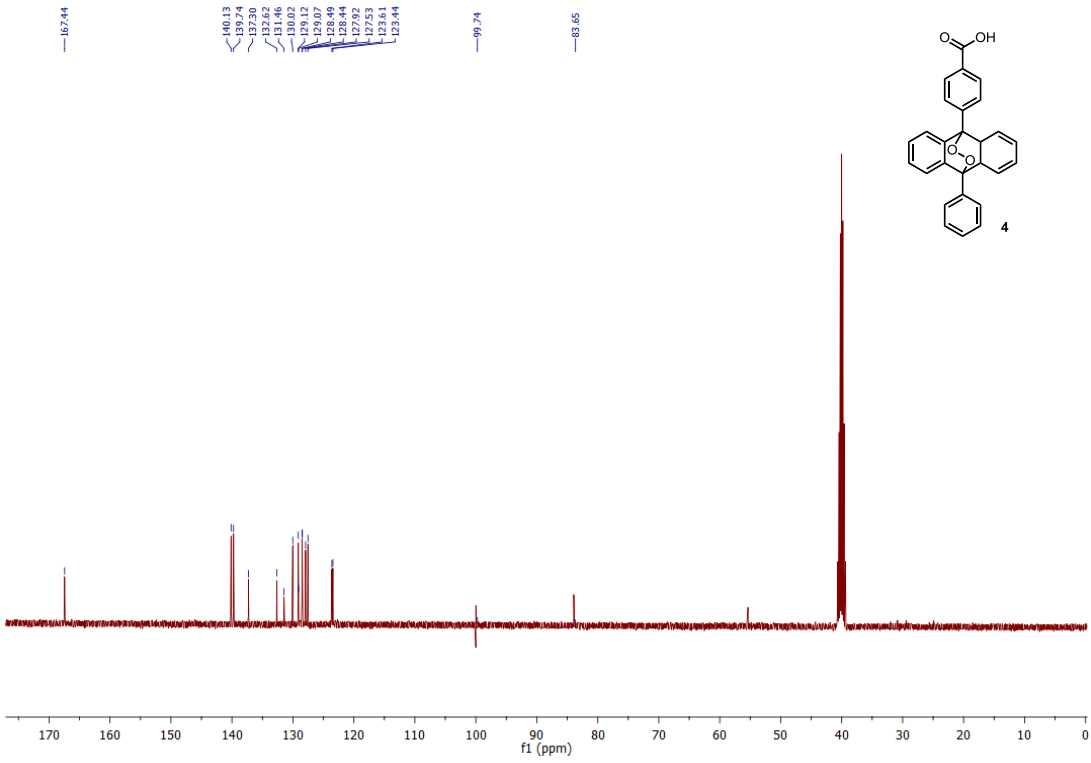
167.44
140.13
139.74
137.30
132.62
131.46
130.02
129.12
129.07
128.49
128.44
127.92
127.53
123.61
123.44
99.74
83.65
OH
O
O
O
4
170
160
150
140
130
120
110
100
90
80
70
60
50
40
30
20
10
0
f1 (ppm)

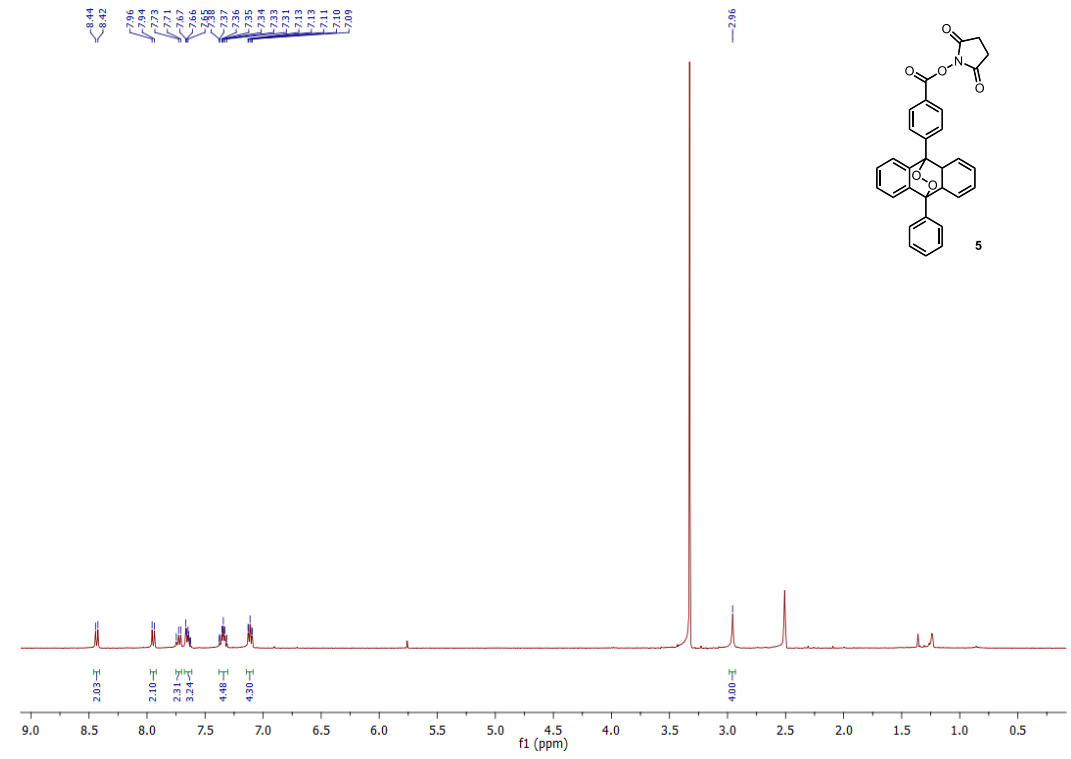
8.44
8.42
7.96
7.94
7.73
7.71
7.67
7.66
7.38
7.37
7.36
7.35
7.34
7.33
7.31
7.13
7.13
7.11
7.10
7.09
2.96
O
O
N
O
O
O
O
5
2.03
2.10
2.31
3.24
4.48
4.30
4.00
9.0
8.5
8.0
7.5
7.0
6.5
6.0
5.5
5.0
4.5
4.0
3.5
3.0
2.5
2.0
1.5
1.0
0.5
f1 (ppm)

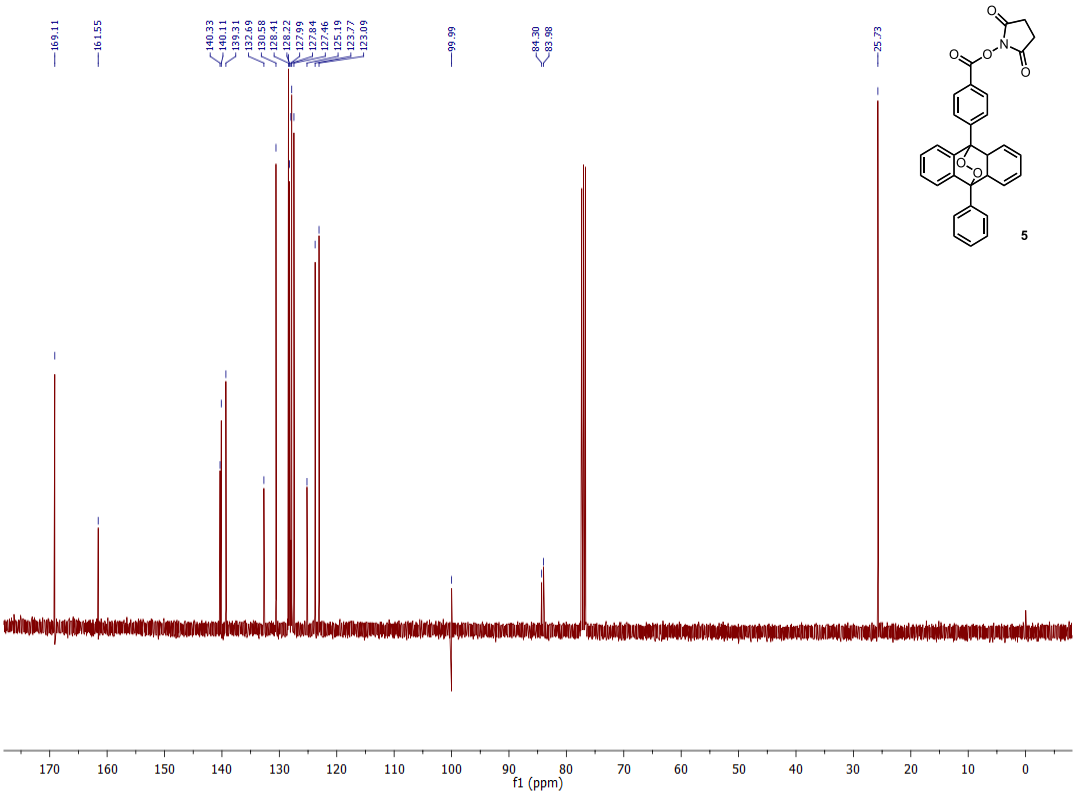
169.11
161.55
140.33
140.11
139.31
132.69
130.58
128.41
128.22
127.99
127.84
127.46
125.59
123.27
123.09
99.99
84.30
83.98
25.73
5
170 160 150 140 130 120 110 100 90 80 70 60 50 40 30 20 10 0
f1 (ppm)

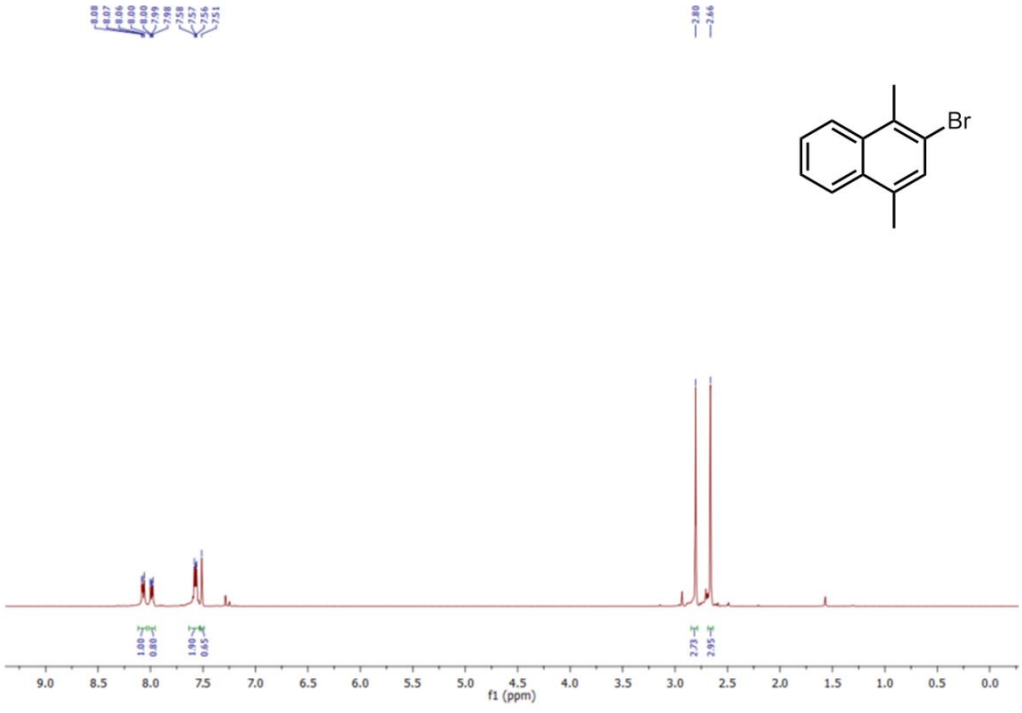
8.08
8.07
8.06
8.00
8.00
7.99
7.98
7.58
7.57
7.56
7.51
3.00
2.46
Br
1.00
0.80
1.90
0.65
2.73
2.95
9.0 8.5 8.0 7.5 7.0 6.5 6.0 5.5 5.0 4.5 4.0 3.5 3.0 2.5 2.0 1.5 1.0 0.5 0.0
f1 (ppm)

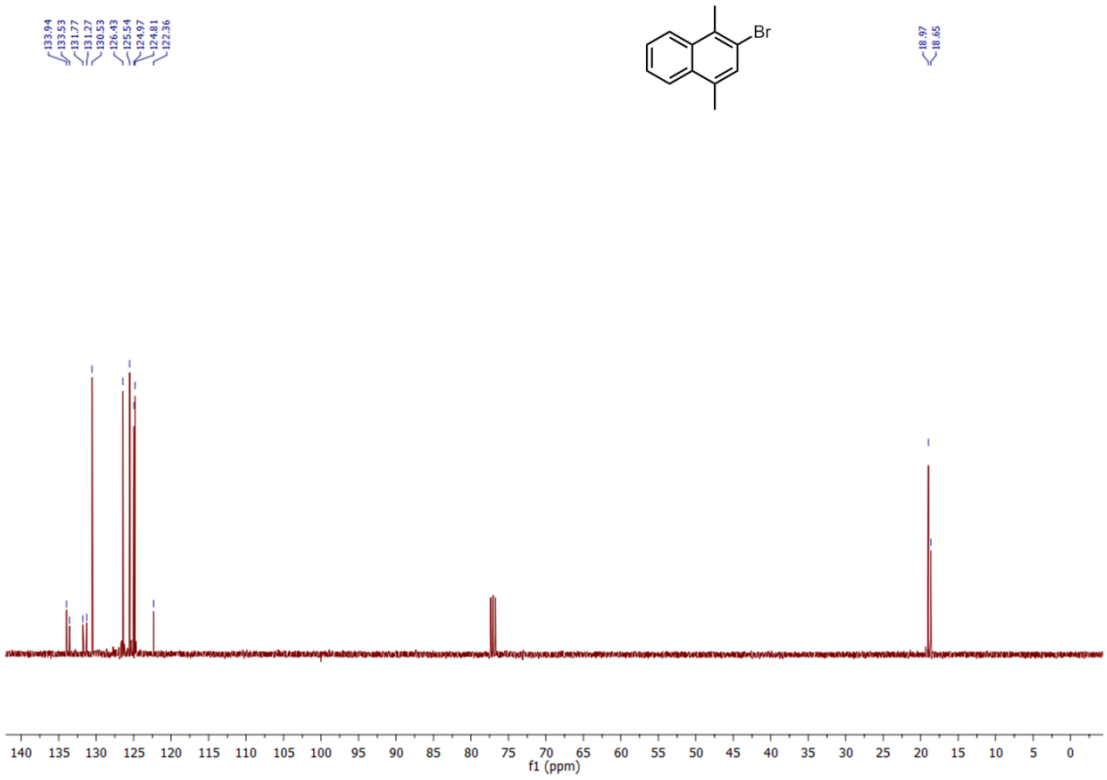
133.94
133.53
131.77
131.27
130.53
126.43
125.54
124.97
124.81
122.36
Br
18.97
18.65
140 135 130 125 120 115 110 105 100 95 90 85 80 75 70 65 60 55 50 45 40 35 30 25 20 15 10 5 0
f1 (ppm)

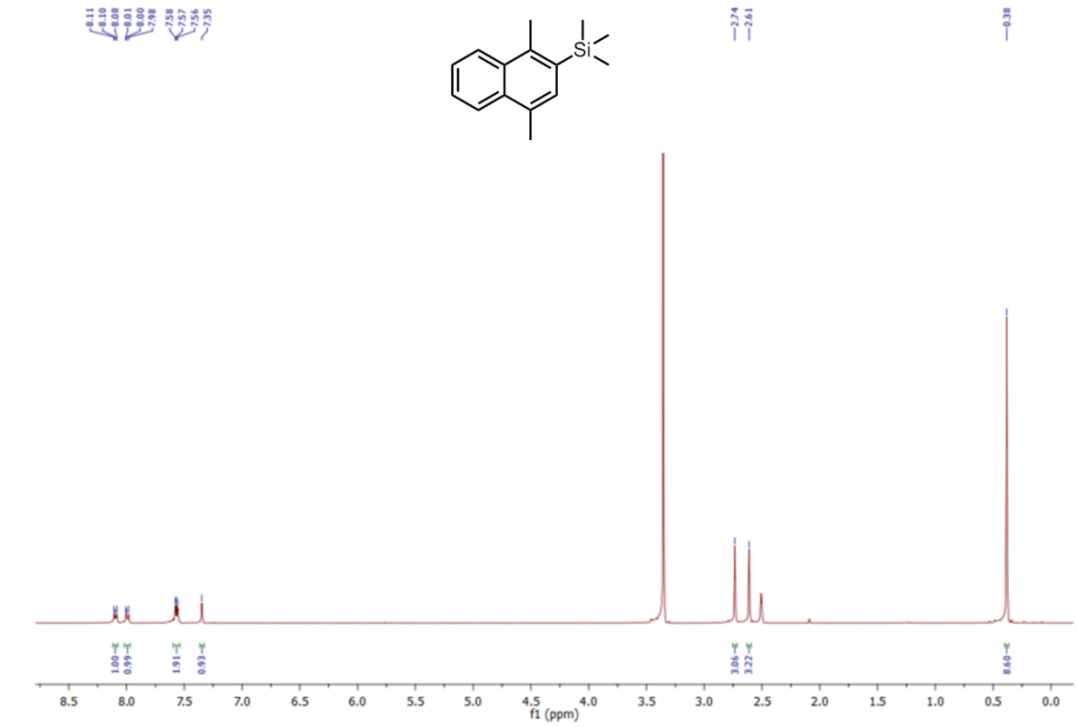
8.11
8.10
8.08
8.01
8.00
7.98
7.58
7.57
7.56
7.35
Si
2.74
2.61
0.38
1.00
0.99
1.91
0.93
3.06
3.22
8.60
8.5 8.0 7.5 7.0 6.5 6.0 5.5 5.0 4.5 4.0 3.5 3.0 2.5 2.0 1.5 1.0 0.5 0.0
f1 (ppm)

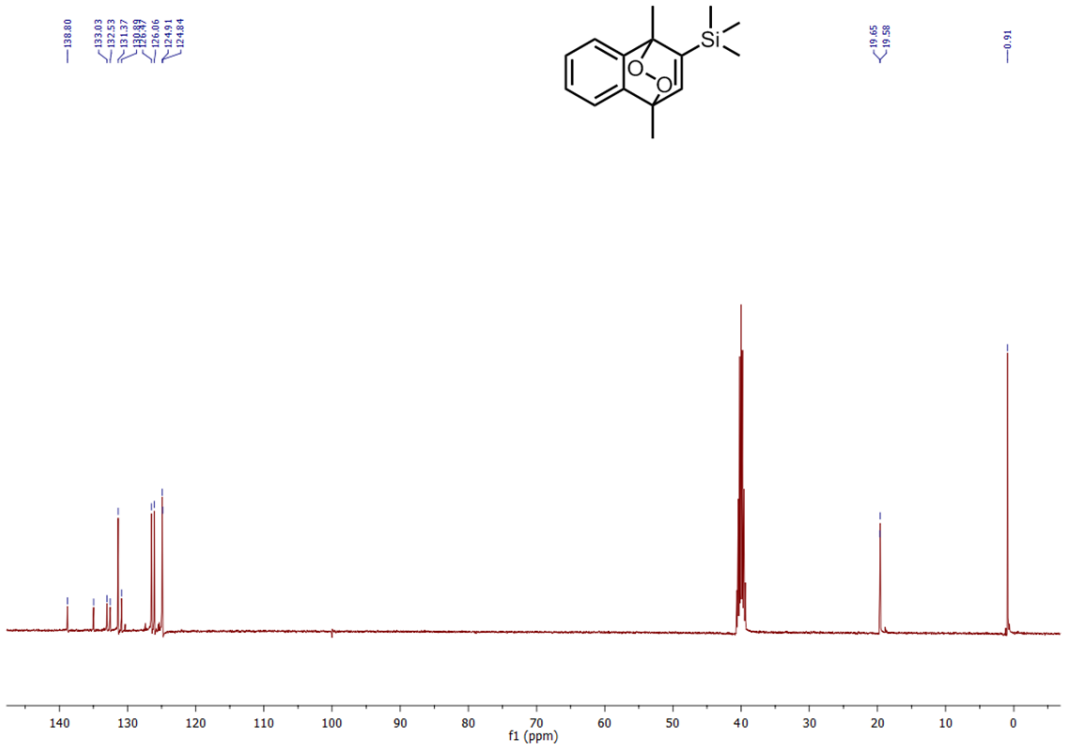
138.80
133.03
132.53
131.37
130.47
126.66
124.91
124.84
19.65
19.58
0.91
Si
O
O
140
130
120
110
100
90
80
70
60
50
40
30
20
10
0
f1 (ppm)

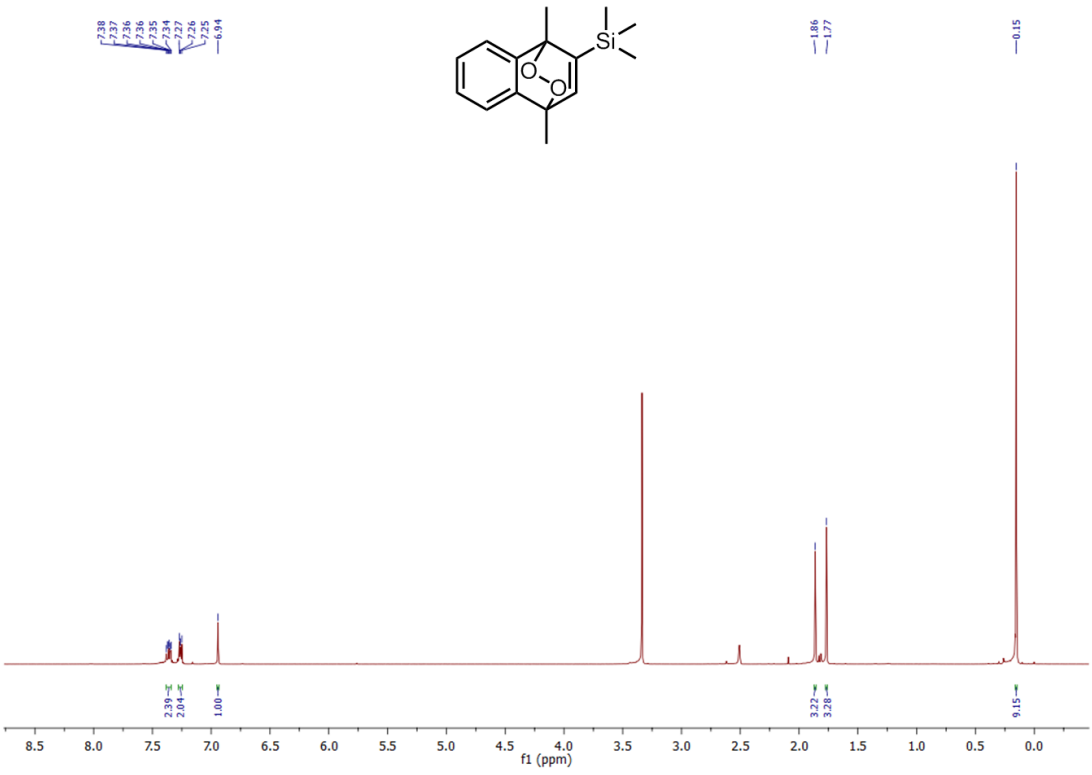
7.38
7.37
7.36
7.36
7.35
7.34
7.27
7.26
7.25
6.94
1.86
1.77
0.15
Si
O
O
2.39
2.04
1.00
3.22
3.28
9.15
8.5
8.0
7.5
7.0
6.5
6.0
5.5
5.0
4.5
4.0
3.5
3.0
2.5
2.0
1.5
1.0
0.5
0.0
f1 (ppm)

Appendix B

Mass Spectra

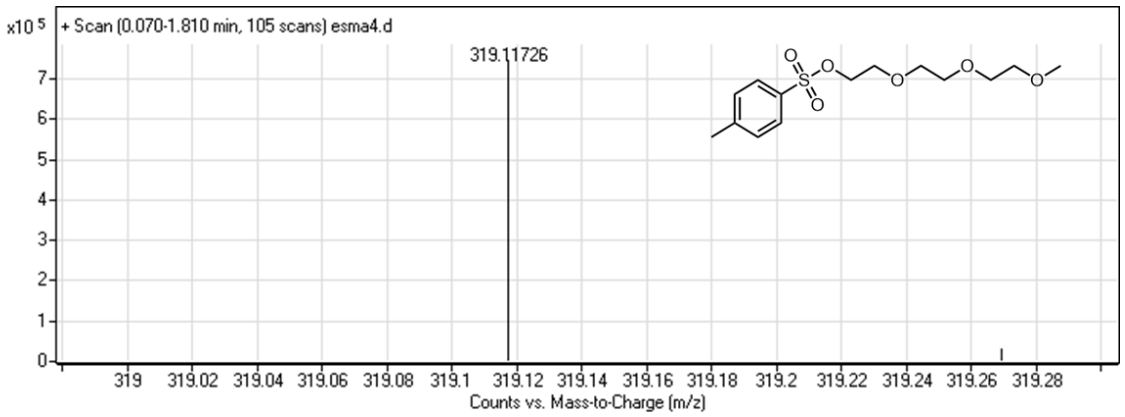

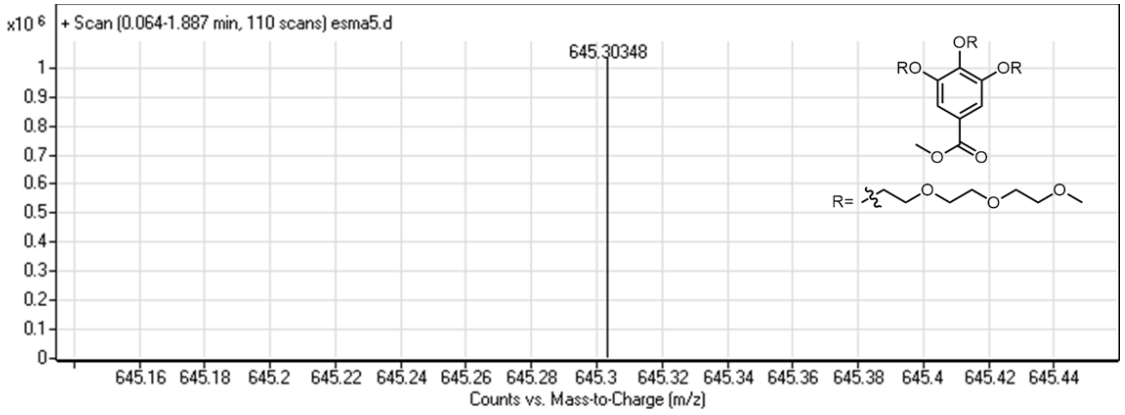

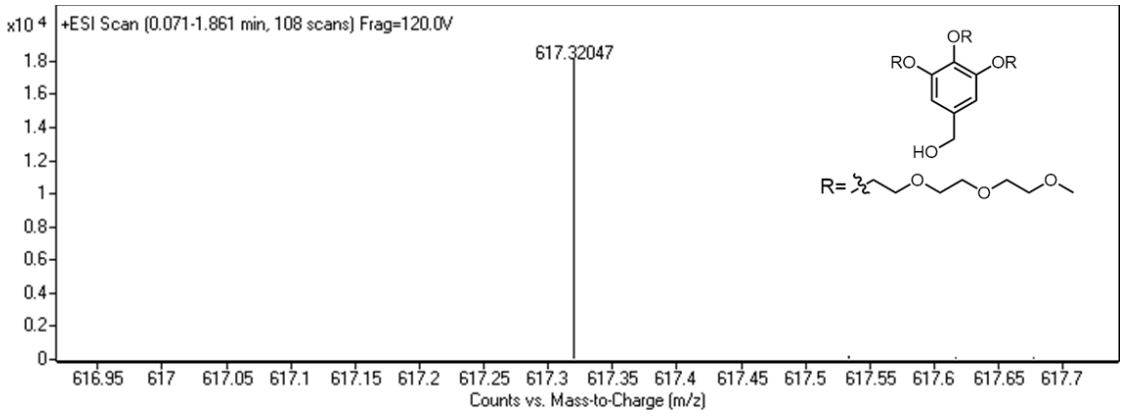

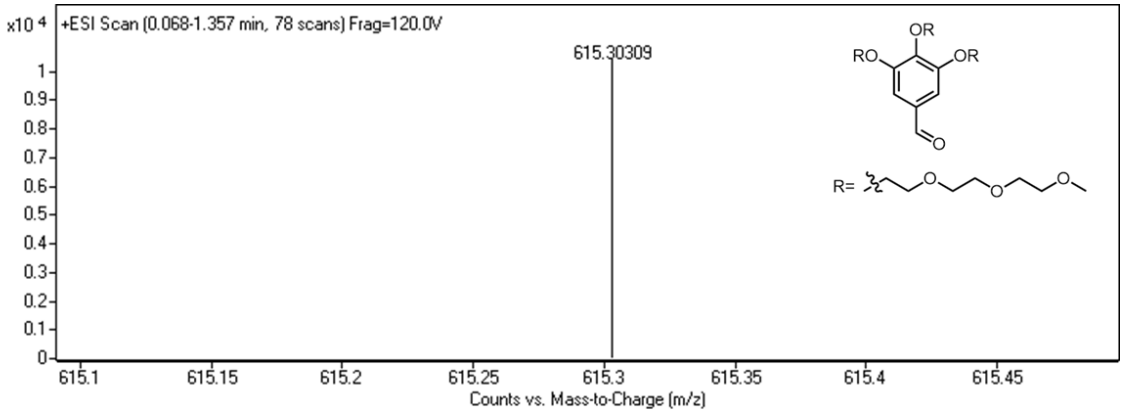
x10 4
+ESI Scan (0.068-1.357 min, 78 scans) Frag=120.0V
615.30309
OR
RO
OR
O
R=
O
O
O
1
0.9
0.8
0.7
0.6
0.5
0.4
0.3
0.2
0.1
0
615.1
615.15
615.2
615.25
615.3
615.35
615.4
615.45
Counts vs. Mass-to-Charge (m/z)

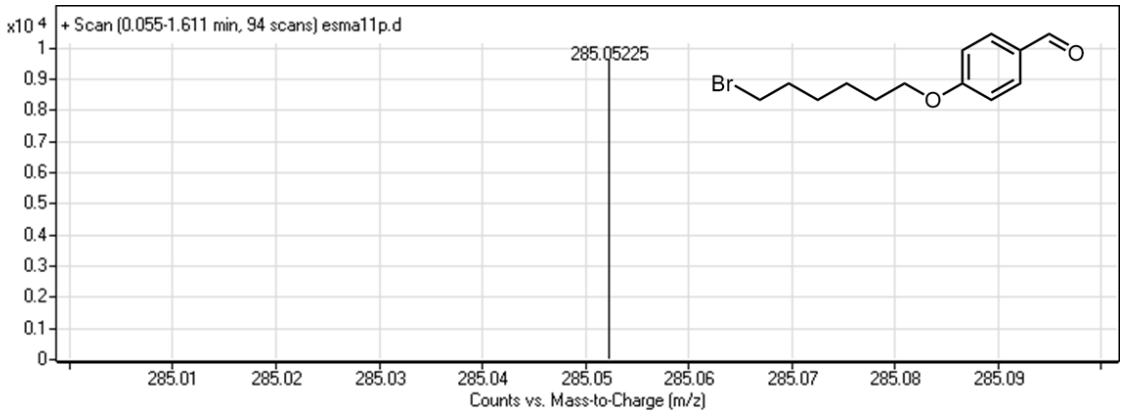
x10 4
+ Scan (0.055-1.611 min, 94 scans) esma11p.d
285.05225
Br
O
O
1
0.9
0.8
0.7
0.6
0.5
0.4
0.3
0.2
0.1
0
285.01
285.02
285.03
285.04
285.05
285.06
285.07
285.08
285.09
Counts vs. Mass-to-Charge (m/z)

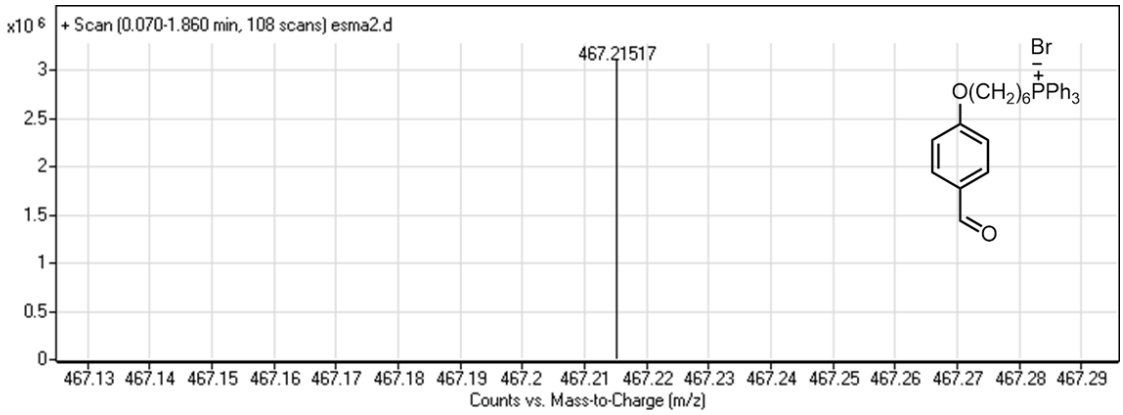
x10 6
+ Scan (0.070-1.860 min, 108 scans) esma2.d
467.21517
Br
O(CH2)6PPh3
O
3
2.5
2
1.5
1
0.5
0
467.13
467.14
467.15
467.16
467.17
467.18
467.19
467.2
467.21
467.22
467.23
467.24
467.25
467.26
467.27
467.28
467.29
Counts vs. Mass-to-Charge (m/z)

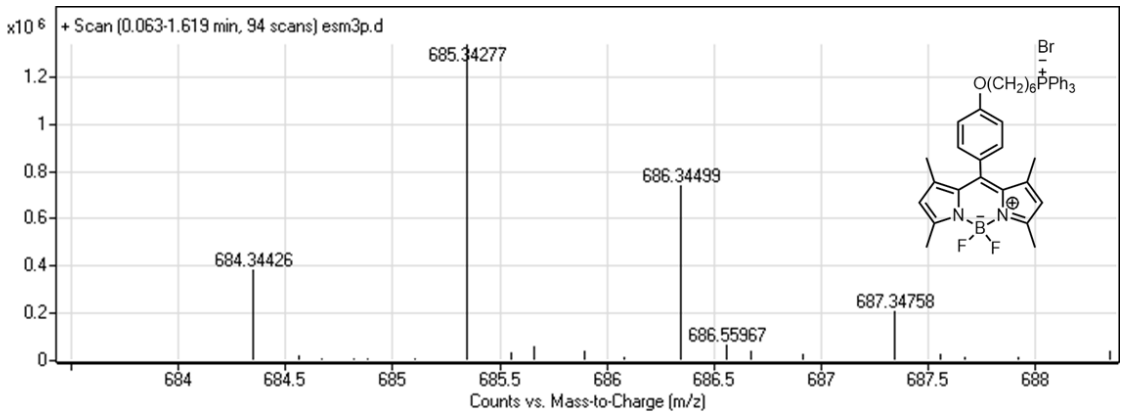
x10 6
+ Scan (0.063-1.619 min, 94 scans) esm3p.d
685.34277
686.34499
684.34426
687.34758
686.55967
Counts vs. Mass-to-Charge (m/z)

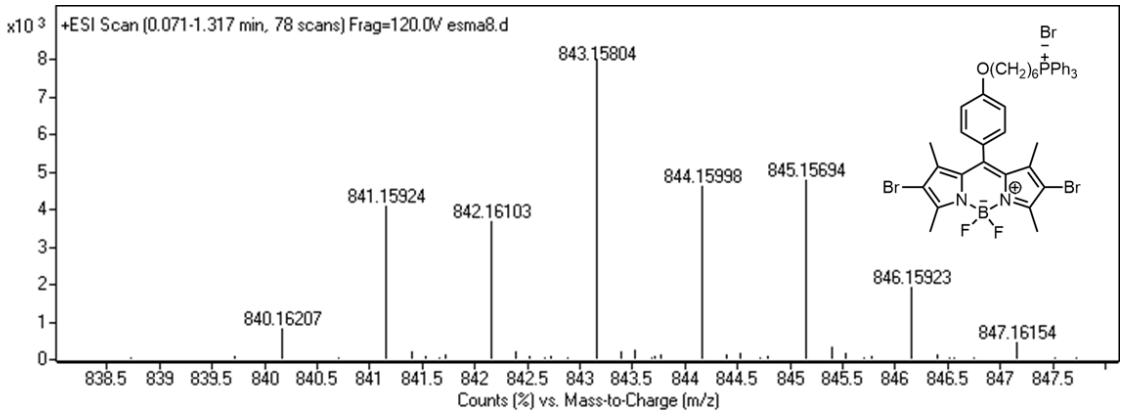
x10 3
+ESI Scan (0.071-1.317 min, 78 scans) Frag=120.0V esma8.d
843.15804
841.15924
842.16103
844.15998
845.15694
840.16207
846.15923
847.16154
Counts (%) vs. Mass-to-Charge (m/z)

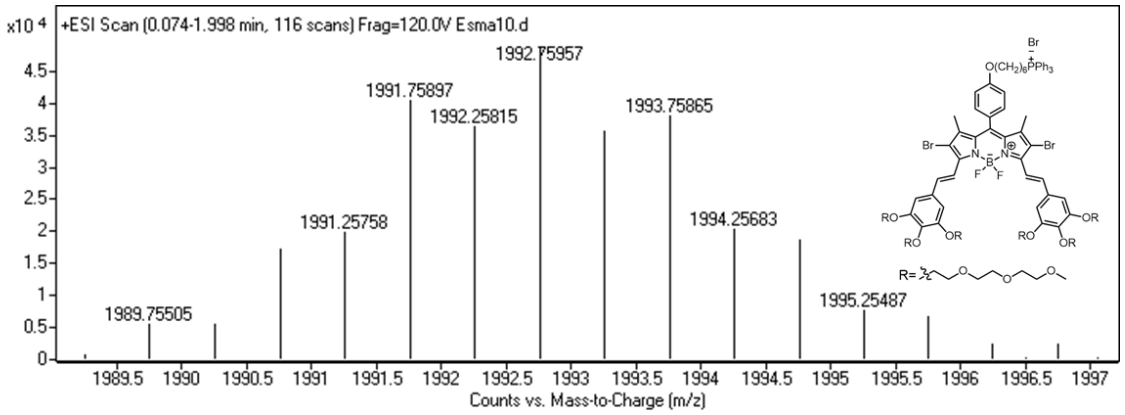
x10 4
+ESI Scan (0.074-1.998 min, 116 scans) Frag=120.0V Esma10.d
1992.75957
1991.75897
1992.25815
1993.75865
1991.25758
1994.25683
1989.75505
1995.25487
Counts vs. Mass-to-Charge (m/z)

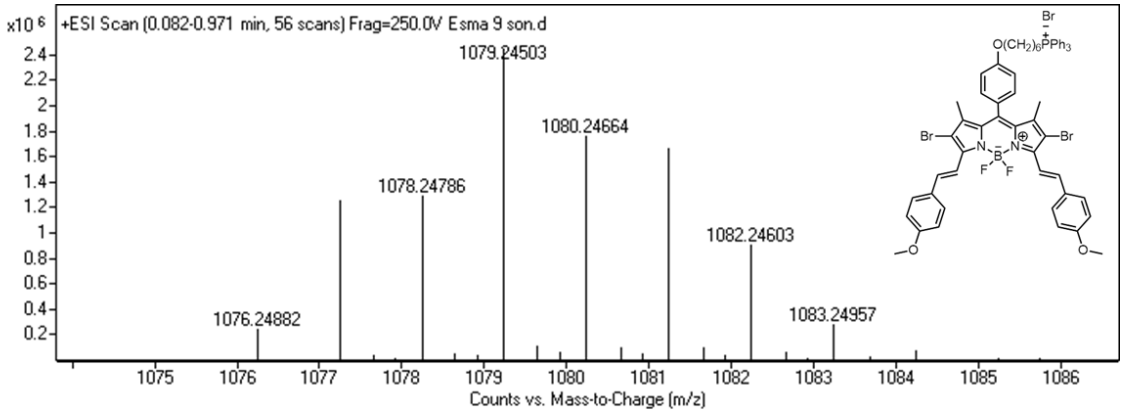
x10 6
+ESI Scan (0.082-0.971 min, 56 scans) Frag=250.0V Esma 9 son.d
1079.24503
1080.24664
1078.24786
1082.24603
1076.24882
1083.24957
Counts vs. Mass-to-Charge (m/z)

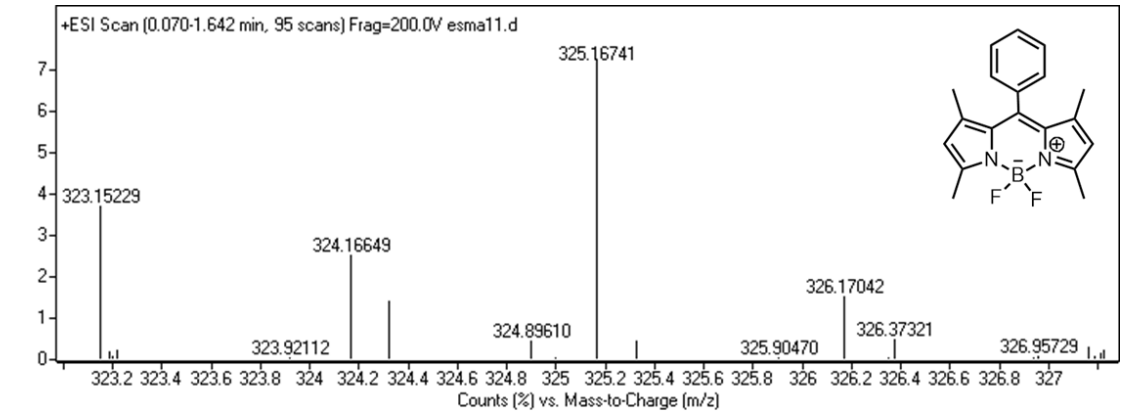
+ESI Scan (0.070-1.642 min, 95 scans) Frag=200.0V esma11.d
325.16741
323.15229
324.16649
326.17042
324.89610
326.37321
323.92112
325.90470
326.95729
Counts (%) vs. Mass-to-Charge (m/z)

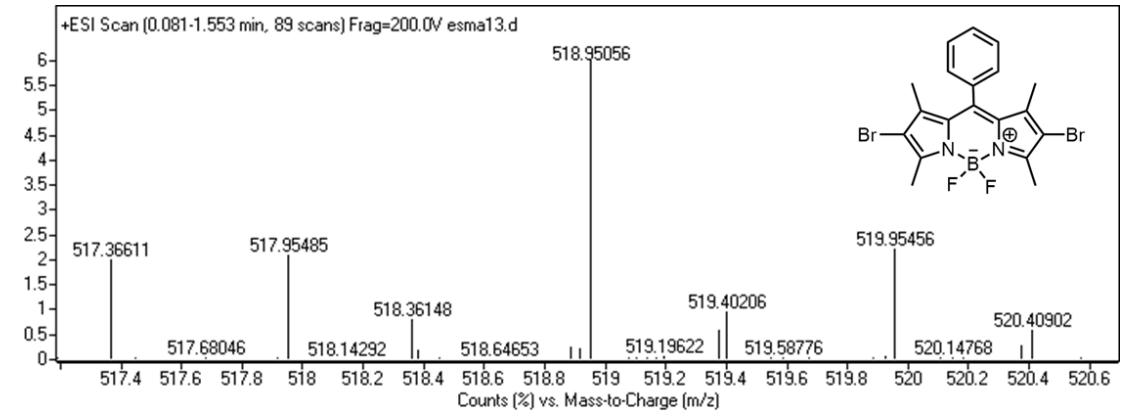
+ESI Scan (0.081-1.553 min, 89 scans) Frag=200.0V esma13.d
518.95056
517.36611
517.95485
519.95456
518.36148
519.40206
520.40902
517.68046
518.14292
518.64653
519.19622
519.58776
520.14768
Counts (%) vs. Mass-to-Charge (m/z)

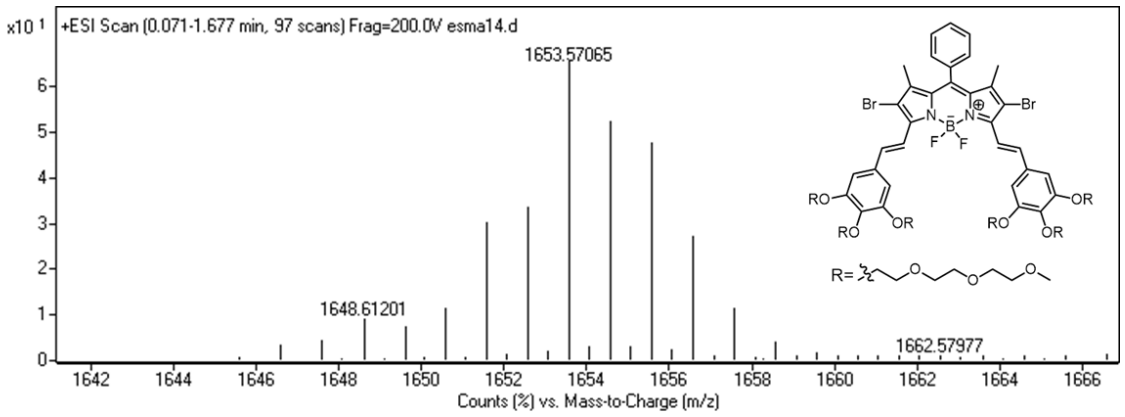
x10 1
+ESI Scan (0.071-1.677 min, 97 scans) Frag=200.0V esma14.d
1653.57065
1648.61201
1662.57977
Counts (%) vs. Mass-to-Charge (m/z)
R=

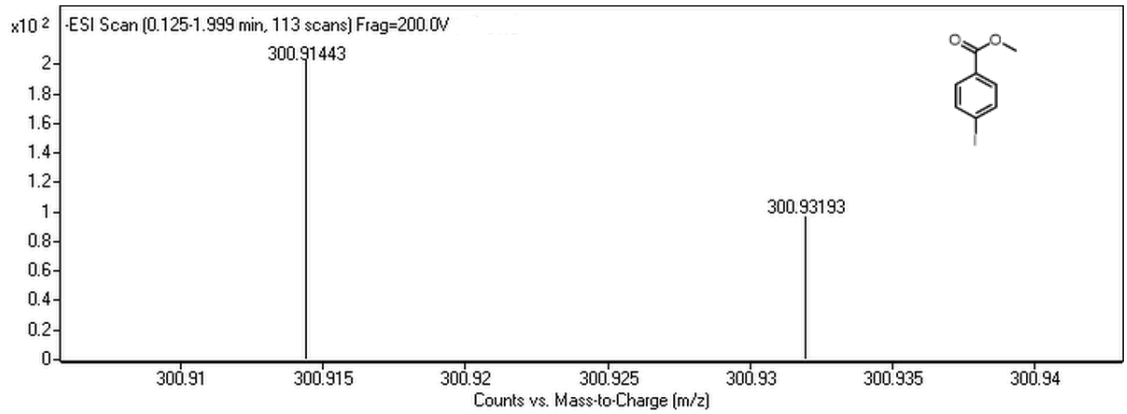
x10 2
-ESI Scan (0.125-1.999 min, 113 scans) Frag=200.0V
300.91443
300.93193
Counts vs. Mass-to-Charge (m/z)

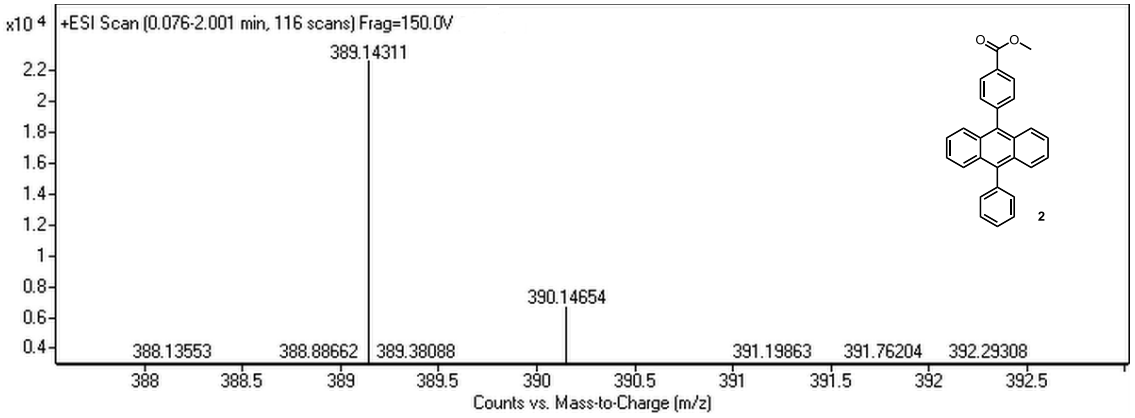
x10 4
+ESI Scan (0.076-2.001 min, 116 scans) Frag=150.0V
389.14311
390.14654
388.13553
388.88662
389.38088
391.19863
391.76204
392.29308
Counts vs. Mass-to-Charge (m/z)
2

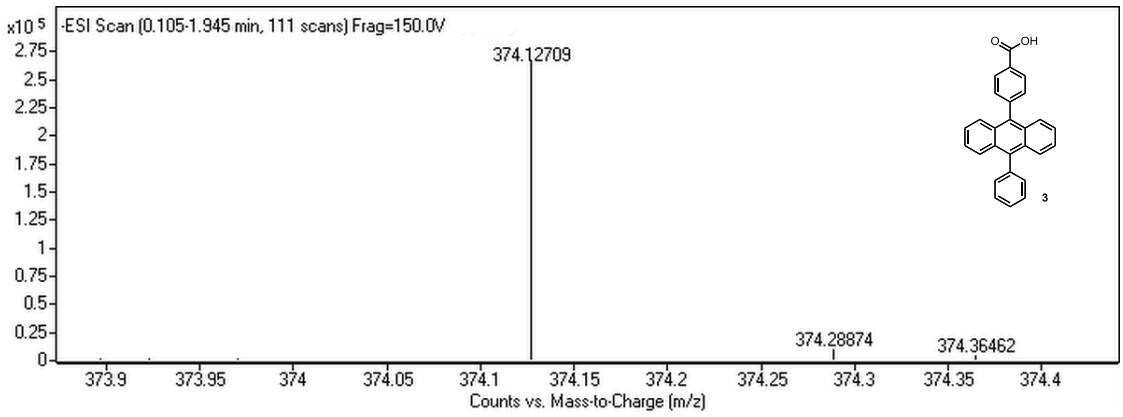
x10 5
-ESI Scan (0.105-1.945 min, 111 scans) Frag=150.0V
374.12709
374.28874
374.36462
Counts vs. Mass-to-Charge (m/z)

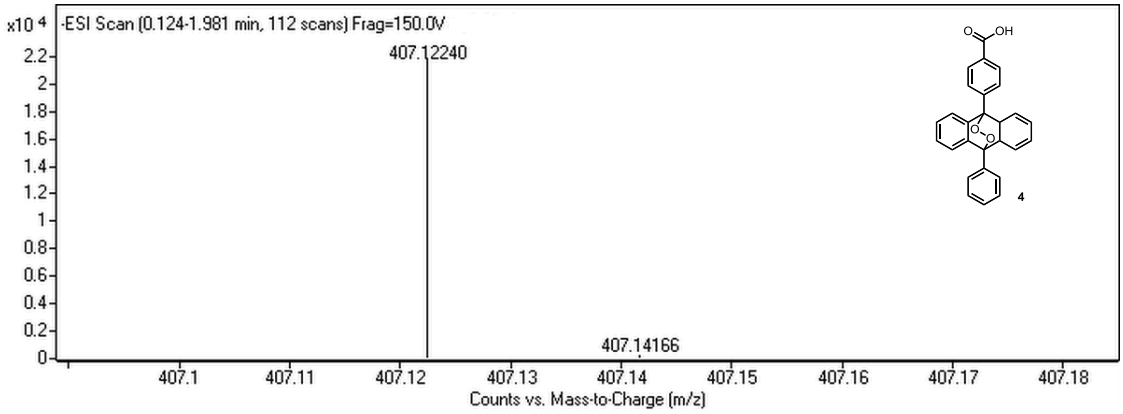
x10 4
-ESI Scan (0.124-1.981 min, 112 scans) Frag=150.0V
407.12240
407.14166
Counts vs. Mass-to-Charge (m/z)

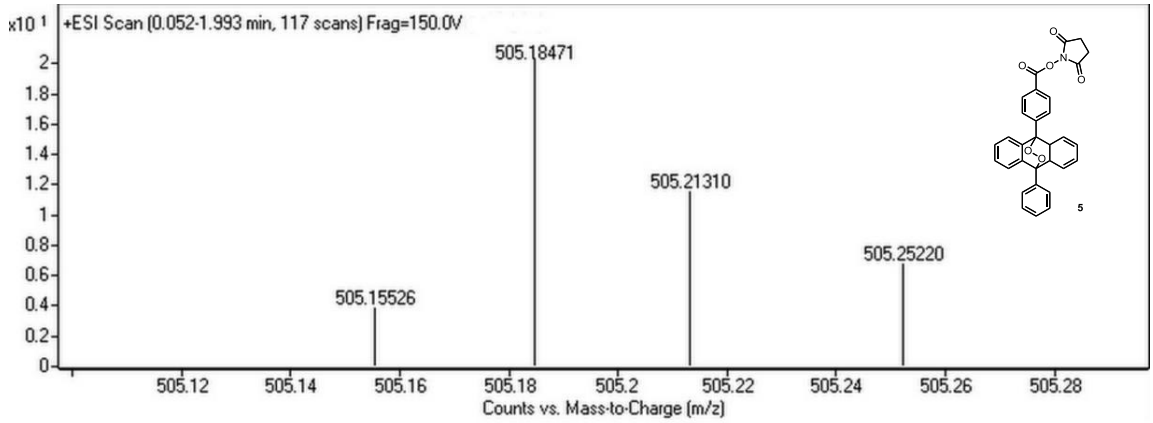
x10 1
+ESI Scan (0.052-1.993 min, 117 scans) Frag=150.0V
505.18471
505.21310
505.25220
505.15526
Counts vs. Mass-to-Charge (m/z)

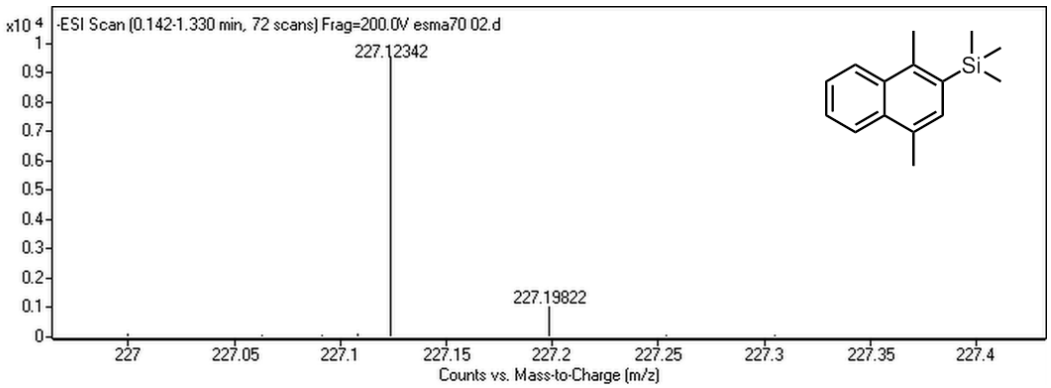
x10 4
-ESI Scan (0.142-1.330 min, 72 scans) Frag=200.0V esma70 02.d
227.12342
227.19822
Si
1
0.9
0.8
0.7
0.6
0.5
0.4
0.3
0.2
0.1
0
227
227.05
227.1
227.15
227.2
227.25
227.3
227.35
227.4
Counts vs. Mass-to-Charge (m/z)

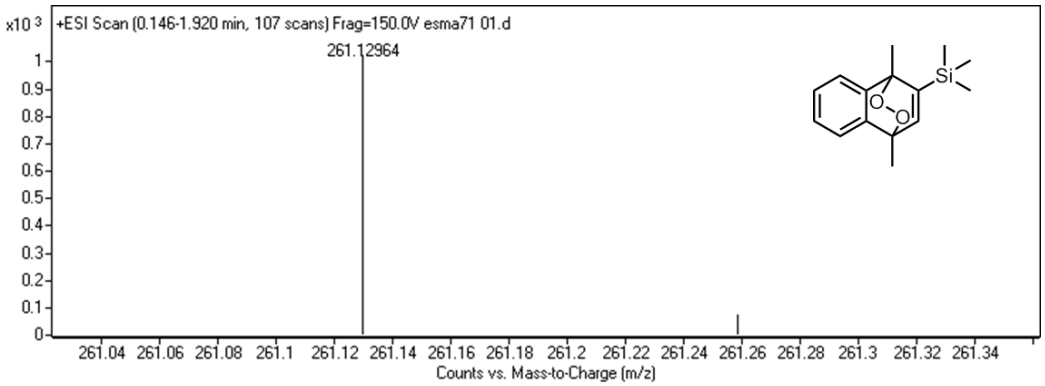
x10 3
+ESI Scan (0.146-1.920 min, 107 scans) Frag=150.0V esma71 01.d
261.12964
Si
O
O
1
0.9
0.8
0.7
0.6
0.5
0.4
0.3
0.2
0.1
0
261.04
261.06
261.08
261.1
261.12
261.14
261.16
261.18
261.2
261.22
261.24
261.26
261.28
261.3
261.32
261.34
Counts vs. Mass-to-Charge (m/z)